MULTISCALE EXPERIMENTAL APPROACHES TO LI-ION BATTERY RESEARCH: FROM PARTICLE ANALYSIS TO OPTIMIZED BATTERY DESIGN

by

Myoungdo Chung

A dissertation submitted in partial fulfillment
of the requirements for the degree of
Doctor of Philosophy
(Mechanical Engineering)
in The University of Michigan
2009

Doctoral Committee:

Professor Ann Marie Sastry, Chair
Associate Professor Christian M. Lastoskie
Associate Professor Wei Lu
Assistant Professor Anton Van der Ven

To My Parents

ACKNOWLEDGEMENTS

First and foremost, I would like to thank my advisor, Professor Ann Marie Sastry, for her inspiration, encouragement and support during the past four years. I cannot be more thankful for her insight that led me to important and challenging research problems, and for her enthusiasm that stimulated me to be a better scientist and engineer. I appreciate the opportunity that I had working with and learning from a true professional like her. She deserves, and has, my deepest appreciation.

I would like to thank Professor Christian Lastoskie, Professor Wei Lu, and Professor Van der Ven for helpful discussions and for serving as my dissertation committee. I also appreciate Dr. Stephen Feinberg of the Department of Surgery in University of Michigan Medical School for his strong support and helpful discussions during the past years.

I acknowledge Dr. Nancy Dudney, Dr. Edgar Lara-Curzio, and all the scientists and staffs at Oak Ridge National Laboratory who helped me with my research for their helpful discussions and great technical expertise. I also want to thank my collaborators at General Motors who shared the same vision of future vehicles, especially, Mr. Bob Kruse and Dr. Xingcheng Xiao for their support and helpful discussions. Also, I thank Dr. Reynaldo Rivera of the Department of Surgery for his willingness to interact with me, and connecting his medical world to my engineering research. Mr. Steve Emanuel, my former machining tutor, should be mentioned here for his technical guidance and dedicated service.

I thank all the group members that I have worked with and shared an office with: Dr. Fabio Albano, Dr. Yen-hung Chen, Mr. Sangwoo Han, Dr. Munish Inamdar, Ms. Qiuye Jin, Dr. HyonCheol Kim, Mr. KC Miller, Dr. Jonghyun Park, Dr. Myounggu Park, Mr. Conor Parks, Ms. Kelsey Powell, Ms. Tahira Reid, Dr. Jeong Hun Seo, Mr. Tim Slusser, Mr. Donghoon Song, Mr. Peter Verhees, Dr. Chia-Wei Wang, Mr. Alex Was, Ms. Maria Xiang, Dr. Xiangchun Zhang, Mr. Min Zhu, and our lab administrator, Ms. Eve Bernos. It has been a great pleasure to work with you all.

Many, many thanks should go to my family in Korea, Mom, Dad, Grandma and my brother, JR, and my sister-in-law for their endless love and trust in me. Also, I sincerely thank my new family, my mother-in-law and father-in-law, for their strong support and warm wishes. Last but not the least, I would like to thank my family in Ann Arbor, my lovely wife, Julia, for her encouragement and care for me, and my little boy, Ian, for coming to us. I love you both so much!

Support of this thesis was provided by U.S. Department of Energy through BATT program (Dr. Tien Duong, Program Manager), General Motors Corporation (Mr. Bob Kruse, GM/UM ABCD co-director), and Oral and Maxillofacial Surgery Foundation, and is gratefully acknowledged.

TABLE OF CONTENTS

LIST OF TABLES

LIST OF FIGURES

LIST OF ABBREVIATIONS

AFM	Atomic Force Microscope
BSE	Back-Scattered Electron
CV	Cyclic Voltammetry
DC	Direct Current
DEC	Diethylene Carbonate
DO	Distraction Osteogenesis
EC	Ethylene Carbonate
EIS	Electrochemical Impedance Spectroscopy
ESD	Electro-Static Deposition
EV	Electric Vehicle
HEV	Hybrid Electric Vehicle
L333	$Li[Ni_{1/3}Co_{1/3}Mn_{1/3}]O_2$
MEMS	Micro Electro-Mechanical Systems
NMP	N-Methyl-2-Pyrolidone
OCP	Open Circuit Potential
PCB	Printed Circuit Board
PHEV	Plug-in Hybrid Electric Vehicle
PITT	Potentiostatic Intermittent Titration Technique
PLD	Pulsed Laser Deposition
POWER	Power Optimization for Wireless Energy Requirement
PSCA	Potential Step Chrono-Amperometry
PVdF	Polyvinylidene Fluoride
RC	Resistance Capacitance
REV	Range-extended Electric Vehicle
RF	Radio Frequency
SEI	Solid Electrolyte Interface

SEM	Scanning Electron Microscope
SOC	State-Of-Charge
SOH	State-Of-Health
TEM	Transmission Electron Microscope
USABC	United States Automotive Battery Consortium
WIMS-EMT	Wireless Integrated Micro Systems-Environmental Monitor Testbed
XPS	X-Ray Photoelectron Spectroscopy
XRD	X-Ray Diffraction

ABSTRACT

We approach the challenges in Li-ion battery research through multiscale experiments: a small but macro scale Li-ion battery was designed for an implantable surgical device for distraction osteogenesis, while in particle- to micro-scale, the baseline cathode materials for Li-ion batteries were investigated for their structural and electrochemical characteristics. For the optimized battery design study, we first identified the power / energy requirements for a common clinical protocol using a novel distraction device developed in parallel to its battery design, and then ran an algorithm to select a commercially available battery with minimal volume that satisfied the system demands. A polymer Li-ion battery was selected due to high power and energy densities as well as its favorable geometry. A bench-top prototype device, integrating an actuator, a control circuit, and a battery, was fabricated to test its functionality and reliability, and eventually will be ready for animal implantation studies.

Particle- to micro- scale experimental studies of Li-ion insertion metal oxide cathode materials were conducted using simple forms of the baseline materials, such as thin films and dispersed single particles, aiming to understand their structural characteristics and electrochemical properties. Various characterization techniques including SEM, TEM, XRD, and AFM were used to observe external and internal

microscopic morphology of primary particles from candidate cathode materials for EV applications, such as $LiFePO_4$, $Li[Ni_{1/3}Co_{1/3}Mn_{1/3}]O_2$, and $LiMn_2O_4$. Their anisotropic and inhomogeneous nature was revealed due to the hierarchic structure consisting of crystal grains and grain boundaries. Thin film study of $LiMn_2O_4$ also showed similarly complex microstructures that were found to be determined by their fabrication conditions, including substrate material and annealing temperature.

In an experimental study with single $LiMn_2O_4$ particles, we take one step toward precise modeling and control of large format cells in EV applications by generating and incorporating accurate model parameters, including diffusion coefficients from CV and PITT methods, and realistic particle geometries from AFM scanning data. Simulation of Li-ion intercalation with the implemented experimental measurements showed that $LiMn_2O_4$ particles could be under higher intercalation-induced stress due to slower diffusion and local stress concentration at the grain boundaries.

CHAPTER I

INTRODUCTION

One of the biggest challenges to human civilization in the twenty first century is to find ways to generate, store, and use energy with minimum environmental impact. Lithium-ion (Li-ion) battery technology has been and will be a key solution to this challenge in multiple applications from consumer electronics to miniature medical devices and micro electromechanical systems (MEMS), and to electric or hybrid electric vehicles (EV / HEV). Since its commercialization by Sony in 1991, Li-ion batteries have been used in a wide range of applications for portable electronic devices, such as digital cameras, cell phones, and laptop computers. The first commercial batteries utilized a layered oxide material, such as $LiCoO_2$, for cathodes and petroleum coke for anodes, while a number of lithium intercalation compound materials have been introduced as Li-ion battery electrodes. Figure 1.1 shows a schematic diagram of a Li-ion battery [1]. Lithium metal oxides with a layered or a three-dimensional tunneled structure are typical materials for the cathode (positive electrode) (Table 1.1 [1, 2, 3, 4, 5]); graphitic carbons are commonly used for the anode (negative electrode), while a series of alloys and metal oxide compounds were also developed as anode materials for Li-ion batteries (Table 1.2 [6, 7, 8, 9, 10]).

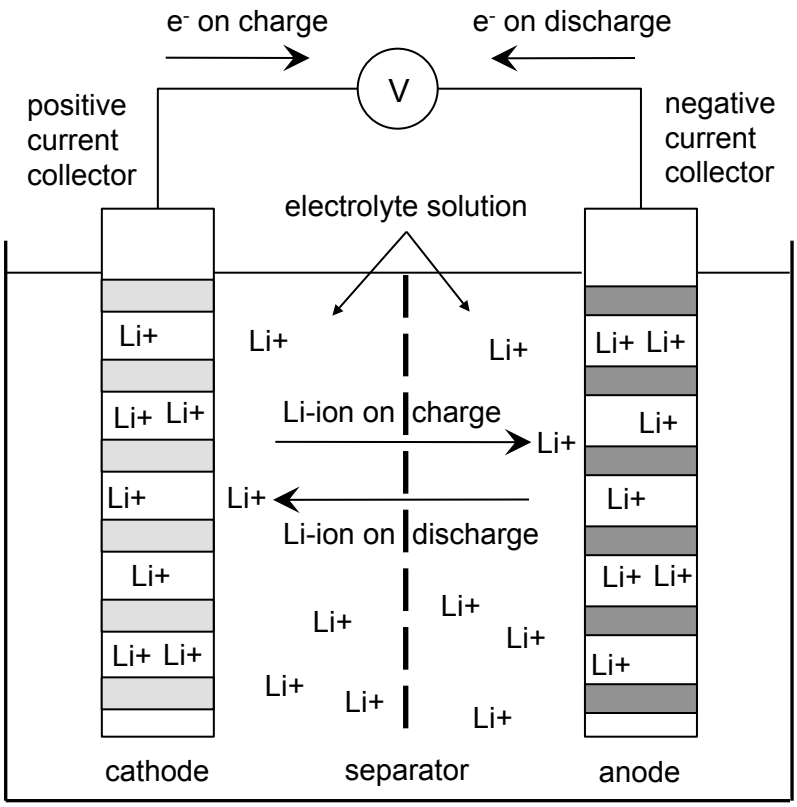

Figure 1.1: Schematic diagram of Li-ion battery

Material	Lattice Structure	Synthesis method	Specific capacity (mAh/g)	Nominal voltage vs. Li (V)
$LiCoO_2$	Layered	Electrochemical lithium extraction	155	3.88
$LiNiO_2$	Layered	Pyrolysis from LiOH and $Ni(OH)_2$	200	3.55
$LiMn_2O_4$	Tunneled, spinel	Calcination from Mn_3O_4 and Li_2CO_3	120	4.00
$Li[Ni_{1/3}Co_{1/3}Mn_{1/3}]O_2$	Layered	Carbonate coprecipitation	160	3.75
$LiFePO_4$	Tunneled, olivine	Microwave processing	110	3.50

Table 1.1: Comparison of cathode materials for Li-ion batteries [1-5]

Material	Type	Synthesis method	Specific capacity (mAh/g)	Nominal voltage vs. Li (V)
Li	Lithium metal	Lithium foils readily available	3860	0.0
$Li_{0.5}C_6$ (coke)	Disordered, non-graphitic carbon	Petrochemical side product	180	0.0-1.3
LiC_6 (graphite)	Ordered layer graphite	Natural graphite readily available	300	0.0-0.3
LiC_6 (MCMB)	Modified graphitic carbon	Graphitization from petroleum residua or coal	700	0.0-0.25
Li-Sn, Si	Alloy	Tin and silicon readily available	500	0.04-0.8
SnSb	Alloy	Tin-antimony alloying	360	0.7-0.8
$Li_4Ti_5O_{12}$	Transition metal oxide	Solid-state reaction of TiO2 and Li2CO3 or LiOH	160	1.5

Table 1.2: Comparison of anode materials for Li-ion batteries [6-10]

Implantable medical devices and MEMS are another group of Li-ion battery applications that require serious research efforts. Besides the fast-growing market, the extremely demanding system requirements for high performance and safety make medical battery development important and challenging. Battery-powered medical devices have been surgically implanted into the bodies of several million people during the past 40 years, to treat an increasingly diverse number of conditions including cardiac arrhythmias, chronic pain, epilepsy, hearing loss, obesity, vision loss, and scoliosis [11]. Battery-powered implantable medical devices for these conditions are summarized in Table 1.3 for typical electrochemistries, power and energy densities, and lifetime requirements [12, 13, 14]. Considerable research efforts have also been made in MEMS applications to make a micro system autonomous by utilizing a miniature on-board battery. Such a system has been developed for an environmental monitoring sensor [15], an entomological monitor [16], and biomedical telemetry circuit [17]. Biomedical and micro systems have been frontier applications for the development of new chemistries (e.g. lithium-based chemistry for pacemakers) and fabrication methods (e.g. thin film fabrication for micro batteries).

However, for the world's energy-and-environmental challenge, the transportation sector is where Li-ion battery technology should play the most significant role. According to the Energy Information Administration (EIA) report in 2009, the transportation sector dominates in global oil consumption and attributes approximately 1/3 of the total carbon emissions worldwide [18]. One realistic solution to this challenge is battery-based electrification of passenger vehicles and light trucks. The transition is under way; early HEV models have already demonstrated that the battery technology

Implanted device	Typical electrochemistry	Power requirement (mW)	Energy density (Wh L^{-1})	Lifetime requirement
Pacemaker	Li/I_2	0.03-0.1	700	> 10 years
Defibrillator	Li/SVO	10000	780	several years
Neurological stimulator	Li/$SOCl_2$	0.3 to several	680	> 5 years
Drug pump	Li/$SOCl_2$	0.1-2	680	> 5 years
Cochlear implant [13]	Ni-MH or Li-ion	1.6	200	> 5 years
Spinal cord stimulator [14]	polymer Li-ion	2.16	765	0.5-1 year

Table 1.3: Common applications and batteries for implantable medical devices, data taken from [12] unless specified

(mostly Ni-MH batteries) works for automotive applications with excellent market acceptance, and a plug-in HEV (PHEV) or a range-extended EV (REV) has been developed by a major automotive manufacturer (e.g. the Chevy Volt). Li-ion batteries have superior attributes including high energy density, flexible and lightweight design, and longer lifespan than other comparable battery technologies, such as lead-acid, Ni-Cd, and Ni-MH batteries, and so they will likely be used in EVs / HEVs for the next 10-20 years and beyond (Table 1.4).

CHALLENGES

A common goal in Li-ion battery research is improving the intrinsic properties of battery materials for performance and reliability. Different applications, however, either small scale devices (e.g. microchip) or large scale applications (e.g. EV) have specific challenges; increasing number of micro-systems and medical devices require high power batteries, while large format cells in EV/HEVs need to have high energy density to provide a longer driving range per charging. Also, power/energy requirements in small devices are extremely diverse so that optimizing the battery design is only feasible by accurately identifying the usage profile. For automotive applications with well-known power/energy requirements and usage profiles, the real challenge is in monitoring and controlling the batteries for a longer period time based on thorough understanding of the material and the cell behavior.

Attribute \ Battery technology	Lead Acid	Ni-Cd	Ni-MH	Li-ion
Specific energy (Wh kg^{-1})	170	220	220	410
Practical specific energy (Wh kg^{-1})	30-40	40-60	75-100	120-150
Energy density (Wh L^{-1})	50-90	40-100	240	400
Nominal voltage (V)	2.0	1.2	1.2	4.0
Cycle life (cycles)	200-1500	500-1000	300-600	> 1000
Relative toxicity	high	high	medium	medium
Safety	high	high	high	medium

Table 1.4: Comparison of battery technologies [1]

SMALL SCALE LI-ION BATTERIES FOR MEDICAL DEVICES AND MEMS

One major trend in medical / micro systems development is pursuing intensive power usage for advanced functions, such as microprocessor-based operations and improved telemetry, while keeping the total energy consumption reasonably low by reducing background drain. Early medical devices, such as pacemakers, were based on simple algorithms and circuitry and thus required relatively steady and low power, while modern pacemakers and the majority of other implanted devices incorporate sophisticated processing algorithms and circuitry using microprocessors and substantial amounts of memory, and thus have higher peak power requirements. Communication between the operator and the micro devices becomes more common and more important, which also requires high power. Additionally, the size of medical / micro devices becomes smaller, mostly due to improved micro fabrication and circuit designs, and partially due to better understanding of biological mechanisms. For lithium and Li-ion batteries that supply power and energy to those devices, the progress poses new challenges that require batteries designed for strong power performance.

Higher power demands in micro / medical devices are often met by introducing new battery chemistries with high power densities. Yet, for some applications (and functions), high energy density is the more important battery characteristic. For a successful battery design, the tradeoff between power and energy capabilities should be made based on accurate identification of system power and energy demands. An example of this can be found in Wireless Integrated Microsystems environmental monitor testbed (WIMS-EMT) developed in the University of Michigan as a case for diverse power demands in a single system (Table 1.5 [19]). Power required in this micro system ranges

Component	Power (mW)	Voltage (V)
Preconcentrator	Sustained = 650 Peak = 3700	3.0 16.64
Vacuum pump	780	6.0
Chromatographic columns	450	15.0
Thermal cooler	200	3.0
RF evaluation board	Sustained = 45 Peak = 125	3.0
Microvalves	100	1.5
MCU (40 MHz)	Sustained = 10 Peak = 22	0.9 1.8
UMSI chip	12	3.0
Sensor array	0.2	3.0
Ambient sensors	Negligible	3.0

Table 1.5: WIMS-EMT components with power and voltage requirement [19]

between 0.2 and 3700 mW, and the voltage from 0.9 to 15.0 V. Only by accurately assessing its power and energy demand can the system be utilized with an optimal power supply with prismatic polymer Li-ion batteries [19].

In addition, effective integration and packaging is another critical challenge to micro / medical batteries. As the volume fraction of these batteries in miniature applications is frequently more than 50% of the total device volume, the overall power and energy densities of the system considerably depend on how the batteries are incorporated with other components. Thermal and mechanical reliability of the battery as well as its performance should be considered when the device is designed.

LARGE FORMAT LI-ION BATTERIES FOR EV / HEV

Automotive application of Li-ion batteries brings significant challenges to the technology. Table 1.6 lists battery requirements for EVs proposed by the U.S. Automotive Battery Consortium (USABC). It is promising that Li-ion batteries' theoretical capabilities well match the requirements for EV applications (Table 1.4); compared to technologically-matured batteries, such as lead-acid or Ni-MH, Li-ion batteries have significant potentials for improvement, especially with on-going research efforts for new chemistry and cell engineering. However, current Li-ion technology does not reach the goals yet with its practically achievable values for energy density, specific power, and cycle life. Especially for transportation applications, reliable estimation of battery behavior and its health during the cycle life is critical, considering the vibrant cycling condition and lengthy life expectation. Obtaining accurate knowledge of battery

Battery attribute	Minimum goals for long term	Long term goals
Power density (W/L)	460	600
Specific power – discharge, 80% DOD/30 sec (W/kg)	300	400
Specific power – Regen, 20% DOD/10 sec (W/kg)	150	200
Energy density – C/3 discharge rate (Wh/L)	230	300
Specific energy – C/3 discharge rate (Wh/kg)	150	200
Specific power / specific energy ratio	2:1	2:1
Total pack size (kWh)	40	40
Life (years)	10	10
Cycle life – 80% DOD (cycles)	1000	1000
Power & capacity degeneration (% of rated spec)	20	20
Selling price – 25,000 units @40 kWh($/kWh)	<150	100
Operating environment (°C)	-40 to +50 20% performance loss (10% desired)	-40 to +85
Normal recharge time (hours)	6 (4 hours desired)	3 to 6
High rate charge	20-70% SOC in 30 minutes @150W/kg	40-80% SOC in 15 minutes
Continuous discharge in 1 hr – No failure (%of rated energy capacity)	75	75

Table 1.6: Goals for advanced batteries for EVs from FreedomCar/USABC

material properties including electrochemical, kinetic, and mechanical characteristics should be the first step toward that understanding.

REVIEW OF THE LITERATURE

DESIGN OF BATTERIES FOR MICRO SYSTEMS

One approach to battery design for implantable medical applications and MEMS devices with diverse power requirements is hybridizing their batteries by incorporating either multiple electrode materials or chemistries with varying power / energy characteristics. Recently efforts have been made in the field of cardiac devices and neurological stimulators to replace the Li/I_2 cells with hybrid cathode systems composed of carbon monofluoride and silver vanadium oxide (CF_x-SVO) to maintain the high energy density of existing chemistry, and to offer higher voltage and rate capability. [20, 21]. The idea of combining multiple batteries as a hybrid power supply system was originally suggested in a battery selection algorithm called POWER (Power Optimization for Wireless Energy Requirement) for MEMS devices [19, 22] and adopted in a battery design for an implantable intraocular device [23] as summarized in Table 1.7. In some applications with wide power requirement range, this approach can benefit power performance within specified energy density and cycle life.

OPTIMIZING LARGE FORMAT LI-ION BATTERIES FOR EV/HEV

At the system level, developing methods for monitoring and controlling Li-ion

Device	Function	Battery solution	Power requirement (mW)	Energy density (Wh L^{-1})
WIMS-ERC EMT	Environmental monitoring	Polymer Li-ion	0.085-1300	270
WIMS-ERC Amadeus	Cochlear implant for hearing aid	Polymer Li-ion	0.24-12.3	268
WIMS-ERC IOS	Intraocular sensor implant for ocular tissue disorder	Zn/AgO	0.0000042	525

Table 1.7: Battery selection using POWER algorithm for medical and MEMS devices [19, 22, 23]

cells and packs has been a major subject of study. Li-ion cells require careful monitoring of their charging and discharging voltages to preserve their longevity and maintain their safety. Battery control algorithms using sophisticated techniques, such as Kalman filtering, have been proposed to estimate state-of-charge (SOC), nominal capacity, and resistance under dynamic conditions in Li-ion polymer battery packs [24, 25]. Simulation results from a mathematical and empirical model using this technique showed ±3% accuracy within 100s at temperatures greater than -20°C, even with a significant initial error. Advanced cell models, however, are required to improve accurate estimating SOC and state-of-health (SOH) to account for cell aging.

Modeling and simulation of Li-ion cathode materials has also been a subject of active studies [26, 27, 28, 29]. Electrochemical reactions and kinetics of Li-ion intercalation in $LiMn_2O_4$ spinel material were modeled in two- or three-dimensional particle structures of theoretical shapes, such as spheres or ellipsoids (Fig. 1.2). The modeling works have proved their worthiness in three different ways. First, the simulation models can predict some unknown material properties. A diffusion coefficient in a $LiMn_2O_4$ single particle, for example, was estimated from a mathematical model by empirically fitting cyclic voltammetric curves to experimental measurements [26]. Second, models can be used to extract desirable geometric parameters for target battery materials. The simulation results in [28, 29] suggested large aspect ratio ellipsoidal particles with smaller sizes are desirable to reduce intercalation-induced stress during cycling of Li-ion batteries. Finally and most importantly, all the previous simulation models' basic purposes are predicting electrochemical and kinetic behaviors of Li-ion intercalation and the corresponding mechanical responses within the material structure.

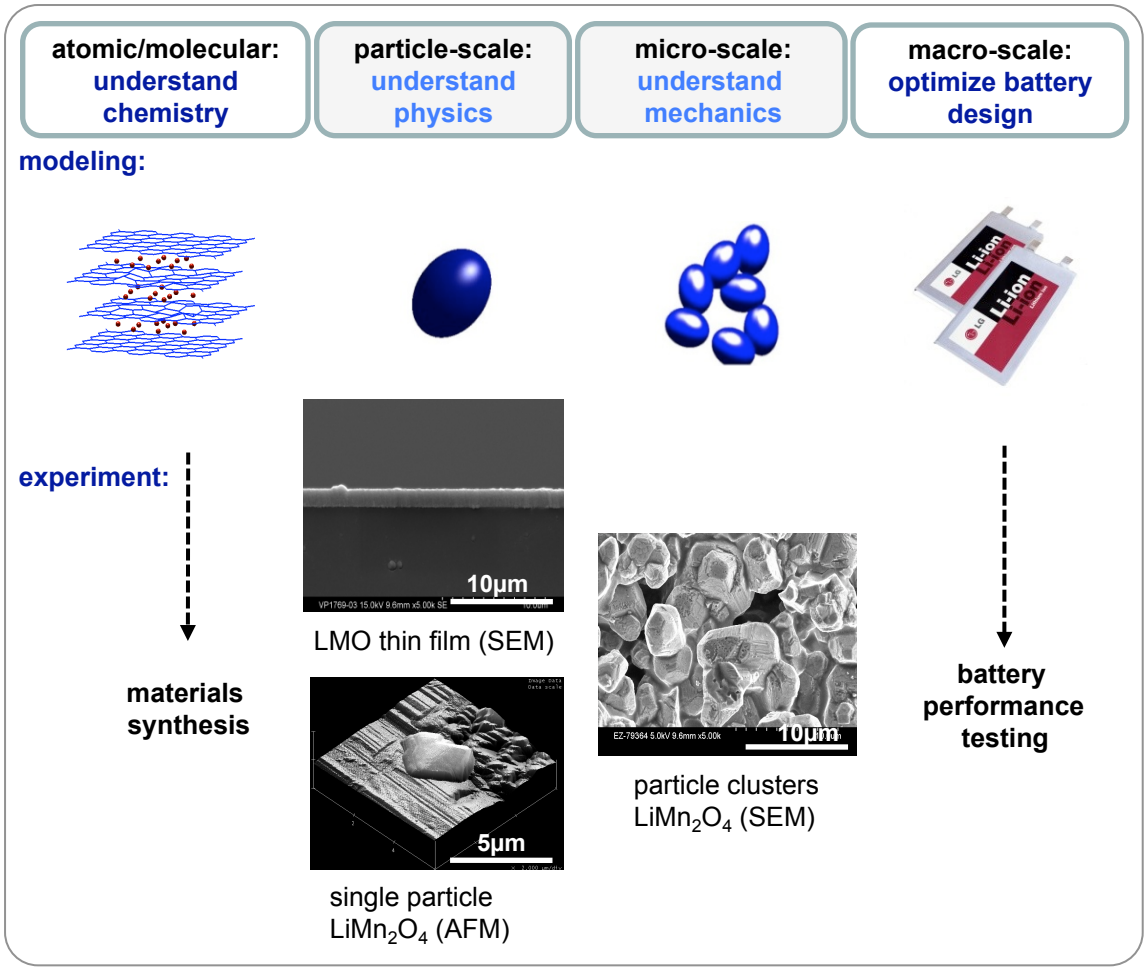

Figure 1.2: Multiscale approaches to Li-ion battery research

This role has a particular importance in controlling the Li-ion battery system, which is a considerable challenge for the automotive applications. The major obstacle to better Li-ion battery modeling is the lack of experimental data to provide accurate input parameters, such as material properties and structure, and to validate the simulation results.

Multiscale approaches in Li-ion battery research are summarized in Figure 1.3: from atomic and molecular scale to understand battery chemistry, to particle- / micro-scale to understand physics and mechanics in a single electrode or aggregates, and to macro-scale to optimize battery design. Both simulation and experimental studies are important for optimizing battery materials for large format Li-ion batteries for EV / HEV. Simulation and modeling of Li-ion batteries have been done in all these different scales, while experimental studies have mainly been done either in atomic / molecular scale of developing and modifying battery materials, or in macro-scale of testing battery performances using various electrochemical techniques to empirically optimize cell engineering procedures. Our experimental approaches aims to fill this gap between material synthesis level and battery testing level by studying particle- to micro-scale battery materials.

There have been a number of studies on micro-scale battery materials to find a link between structural characteristics and electrochemical performances. The most common experimental models are thin film electrodes. Defined by a thickness less than a few microns, thin films have some advantages for micro-scale battery materials study as they provide a uniformly dense layer of pure active material. First of all, thin films containing only the active material can provide accurate evaluation of the kinetic properties without any parasitic effect of conductive additives and organic binder

(a)

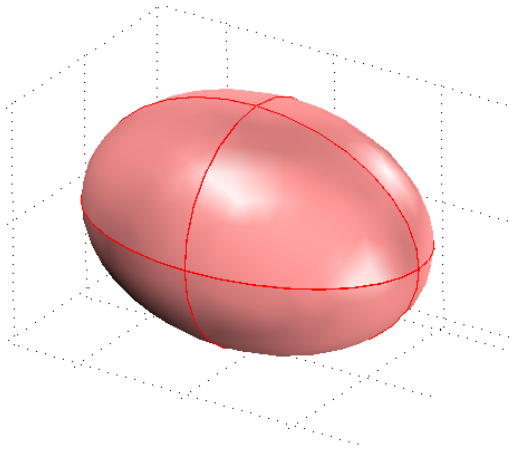

(b)

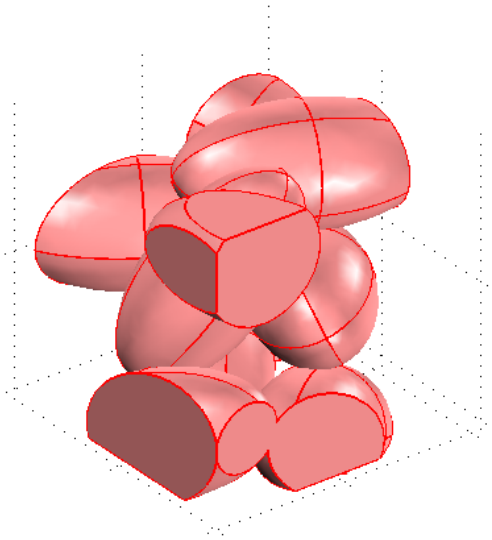

Figure 1.3: Electrode modeling with (a) a single particle, and (b) clustered particles, pictures taken from [28, 29]

materials. Also, the simple film geometry gives a good experimental comparison for a one-dimensional simulation model. In uniform and dense films, there is no complexity from the porous particle networking that often makes experimental analysis more difficult. Additionally, thin films with various micro-structures can be effectively made by changing their fabrication and heat treatment conditions. Table 1.8 summarizes $LiMn_2O_4$ cathode thin films, as an example, fabricated by several different deposition techniques, such as solution-growth [30], radio-frequency sputtering [31, 32, 33, 34], electrostatic spray [35, 36], solution-gel method [37, 38], pulsed laser deposition [39, 40], and e-beam evaporation [41, 42]. These studies help to understand how the micro-structure of cathode materials contributes different electrochemical and kinetic behaviors.

Another group of micro-scale experimental studies uses single particle electrodes (Table 1.9 [43, 44, 45, 46, 47]) as an experimental model. In these so-called micro-voltammetry experiments, a microprobe is used to maintain electric contact between the positive or negative terminal and a single electrode particle, to cycle the isolated particle against a lithium metal counter electrode. This experimental approach shares a common advantage with thin films; it contains only the active material so that the interference from additive materials can be ignored. Additionally, the single particle experiments provide information on how the Li-ion intercalation occurs in the three-dimensional particle structure containing micro-scale features of crystal grains and grain boundaries.

SCOPE AND OUTLINE OF THE DISSERTATION

This dissertation consists of 6 chapters. In the next chapter, we start our discussion from a macroscopic battery design process by a case study of an implantable

Deposition	Electrolyte / anode	Thickness (μm)	Capacity ($\mu Ah/cm^2 \mu m$)	Focus / findings
solution growth	1 M $LiPF_6$ in EC:DMC / Li	0.5	49	nano-crystalline thin films from nano-sized grains
rf-sputtering	Lipon / Li	0.3	48	serial connection of solid-state microbatteries (32V)
	Lipon / Li	0.3	32	all solid-state thin film, process conditioning
	1 M $LiClO_4$ in PC:DMC / Li	0.2	50	process conditioning including Rapid Thermal Annealing temperatures (700-800ºC)
electrostatic spray deposition (ESD)	1 M $LiClO_4$ in EC:DEC / Li	0.45	N/A	high sensitive mass measure by EQCM
	1 M $LiClO_4$ in PC / Li	0.5	64	diffusion coeff by PSCA
Sol-gel	1 M $LiClO_4$ in EC:DMC / Li	1.0	60	use of polyvinylpyrrolidone (PVP) solution
	1 M $LiClO_4$ in PC	0.2	32	deposition process conditioning
pulsed laser deposition (PLD)	1 M $LiPF_6$ in EC:DMC / Li	0.3	66	cycleability enhancement / Ni, Co-substitution
	1 M $LiClO_4$ in PC / Li	0.3	49	deposition technique / film characterization
e-beam evaporation	1 M $LiClO_4$ in PC / Li	0.5-2	N/A	cycling performance, post / in-situ annealing

Table 1.8: Experimental studies with micro-scale battery materials: $LiMn_2O_4$ thin film studies [31-42]

Material(s)	Particle size (μm)	Technique	Focus / findings
$LiCoO_2$ / $LiMn_2O_4$	10 dia.	CV	Development of the technique
$LiCoO_2$ / $LiMn_2O_4$ substitution by Cr / Ni	18 dia.	CV	Electrochemical stability at elevated temperature and effect of substitution
$LiMn_2O_4$ (single crystal)	35×20×12	CV, PITT	Lower diffusion coefficient estimated to 10^{-11} cm^2/s
$LiMn_2O_4$ (poly-crystal)	8-21 dia.	PITT, EIS	Diffusion coefficient in range of 10^{-10} to 10^{-6} cm^2/s
$Li_{4/3}Ti_{5/3}O_4$	30 dia.	CV	2-phase transition (core-shell model)

Table 1.9: Experimental studies with micro-scale battery materials: single particle electrode studies [43-47]

medical device for distraction osteogenesis. From chapter 3 to 5, we redirect our attention to the microscopic scale for the fundamental study of Li-ion battery cathode materials, especially lithium manganese oxide spinel. In chapter 3, experimentally measured diffusion properties and a microscopic geometry from a lithium manganese oxide particle are implemented into battery simulation for comparing experimental and computational results. In chapter 4, we investigate anisotropic and inhomogeneous aspects of typical cathode materials using a series of materials characterization techniques. In chapter 5, experimental approaches are described for thin film cathode material study, from its fabrication to electrochemical and structural characterization. In the last chapter, we summarize our studies and suggest future work.

BIBLIOGRAPHY

1. D. Linden and T.B. Reddy, Handbook of batteries, 3rd Ed., McGraw-Hill (2002)

2. K. Mizushima, P.C. Jones, P.J. Wiseman, and J.B. Goodenough, Li_xCoO_2 ($0<x<1$): A new cathode material for batteries of high energy density, Materials Research Bulletin 15, 783-789 (1980)

3. W. Ebner, D. Fouchard, and L. Xie, The $LiNiO_2$/carbon lithium-ion battery, Solid State Ionics 69, 248-256 (1994)

4. M.-H. Lee, Y.-J. Kang, S.-T. Myung, and Y.-K. Sun, Synthetic optimization of $Li[Ni_{1/3}Co_{1/3}Mn_{1/3}]O_2$ via co-precipitation, Electrochimica Acta 50, 939-948 (2004)

5. A.K. Padhi, K.S. Nanjundaswamy, and J.B. Goodenough, Phospho-olivines as positive-electrode materials for rechargeable lithium batteries, Journal of The Electrochemical Society 144 (4), 1188-1194 (1997)

6. J.L. Tirado, Inorganic materials for the negative electrode of lithium-ion batteries: state-of-the-art and future prospects, Materials Science and Engineering R 40, 103-136 (2003)

7. M. Noel and V. Suryanarayanan, Role of carbon host lattices in Li-ion intercalation/de-intercalation processes, Journal of Power Sources 111, 193-209 (2002)

8. W.J. Weydanz, M. Wohlfaht-Mehrens, and R.A. Huggins, A room temperature study of the binary lithium-silicon and the ternary lithium-chromium-silicon system for use in rechargeable lithium batteries, Journal of Power Sources 81-82, 237-242 (1999)

9. J. Yang, M. Wachtler, M. Winter, and J.O. Besenhard, Sub-microcrystalline Sn and Sn-SnSb powders as lithium storage materials for lithium-ion batteries, Electrochemical and Solid-State Letters 2 (4), 161-163 (1999)

10. T. Ohzuku, A. Ueda, and N. Yamamoto, Zero-strain insertion material of $Li[Li_{1/3}Ti_{5/3}]O4$ for rechargeable lithium cells, Journal of The Electrochemical Society 142 (5), 1431-1435 (1995)

11. C.F. Holmes and B.B. Owens, Batteries for implantable biomedical applications, Wiley Encyclopedia of Biomedical Engineering, John Wiley & Sons (2006)

12. C.L. Schmidt, P.M. Skarstad, The future of lithium and lithium-ion batteries in implantable medical devices, Journal of Power Sources 97-98, 742-746 (2001)

13. J.W. Baumann and H. Leysieffer, Basics of energy supply to completely implantable hearing aids for sensorineural hearing loss, HNO 46 (2), 121-128 (1998)

14. S. Shapiro, R. Borgens, et al., Oscillating field stimulation for complete spinal cord injury in humans: a Phase 1 trial, Journal of Neurosurgery Spine 2, 3-10 (2005)

15. D.R. Lemmerhirt and K.D. Wise, Chip-scale integration of data-gathering microsystems, Proceedings of the IEEE 94 (6) (2006)

16. D.R. Lemmerhirt, E.M. Staudacher, and K.D. Wise, A multitransducer microsystem for insect monitoring and control, IEEE Transactions on Biomedical Engineering 53 (10), 2084-2091 (2006)

17. P. Mohseni, K. Najafi, S.J. Eliades, and X. Wang, Wireless multichannel biopotential recording using an integrated FM telemetry circuit, IEEE Transactions on neural systems and rehabilitation engineering 13 (3) (2005)

18. Energy Information Administration, U.S. Department of Energy, International Energy Outlook 2009 (IEO2009)

19. K.A. Cook and A.M. Sastry, An algorithm for selection and design of hybrid power supplies for MEMS with a case study of a micro-gas chromatograph system, Journal of Power Sources 140, 181-202 (2005)

20. C.L. Schmidt and P.M. Skarstad, The future of lithium and lithium-ion batteries in implantable medical devices, Journal of Power Sources 97-98, 742-746 (2001)

21. K. Chen, D.R. Merritt, W.G. Howard, et al., Hybrid cathode lithium batteries for implantable medical applications, Journal of Power Sources 162, 837-840 (2006)

22. K.A. Cook, F. Albano, P.E. Nevius, and A.M. Sastry, POWER (power optimization for wireless energy requirements): A MATLAB based algorithm for design of hybrid energy systems, Journal of Power Sources 159, 758-780 (2006)

23. F. Albano, M.D. Chung, D. Blaauw, et al., Design of an implantable power supply for an intraocular sensor, using POWER (power optimization for wireless energy requirements), Journal of Power Sources 170, 216-224 (2007)

24. G.L. Plett, Extended Kalman filtering for battery management systems of LiPB-based HEV battery packs, Journal of Power Sources 134, 252-292 (2004)

25. G.L. Plett, Sigma-point Kalman filtering for battery management systems of LiPB-based HEV battery packs, Journal of Power Sources 161, 1356-1384 (2006)

26. D. Zhang, B.N. Popov, and R.E. White, Modeling lithium intercalation of a single spinel particle under potentiodynamic control, Journal of The Electrochemical Society 147 (3), 831-838 (2000)

27. J. Christensen and J. Newman, A mathematical model of stress generation and fracture in lithium manganese oxide, Journal of the Electrochemical Society 153 (6), A1019-A1030 (2006)

28. X.C. Zhang, W. Shyy, and A.M. Sastry, Numerical simulation of intercalation-induced stress in Li-ion battery electrode particles, Journal of the Electrochemical Society 154 (10), A910-A916 (2007)

29. X.C. Zhang, A.M. Sastry, W. Shyy, Intercalation-induced stress and heat generation within single lithium-ion battery cathode, Journal of the Electrochemical Society 155 (7), A542-A552 (2008)

30. S.R. Das, S.B. Majumder, R.S. Katiyar, Kinetic analysis of the Li+ ion intercalation behavior of solution derived nano-crystalline lithium manganate thin films, Journal of Power Sources 139, 261-268 (2005)

31. Y.S. Park, S.H. Lee, B.I. Lee, and S.K. Joo, All-solid-state lithium thin-film rechargeable battery with lithium manganese oxide, Electrochemical and Solid-State Letters 2 (2), 58-59 (1999)

32. J.B. Bates, N.J. Dudney, D.C. Lubben, et al., Thin-film rechargeable lithium batteries, Journal of Power Sources 54, 58-62 (1995)

33. J.B. Bates, N.J. Dudney, B. Neudecker, et al., Thin-film lithium and lithium-ion batteries, Solid State Ionics 135, 33-45 (2000)

34. K.H. Hwang, S.H. Lee, and S.K. Joo, Characterization of sputter-deposited LiMn2O4 thin films for rechargeable microbatteries, Journal of The Electrochemical Society 141 (12) (1994)

35. D. Shu, K.Y. Chung, W.I. Cho, K.B. Kim, Electrochemical investigations on electrostatic spray deposited LiMn2O4 films, Journal of Power Sources 114, 253-263 (2003)

36. M. Nishizawa, T. Uchiyama, K. Dokko, et al., Electrochemical studies of spinel $LiMn_2O_4$ films prepared by electrostatic spray deposition, Bulletin Chemical Society of Japan 71, 2011-2015 (1998)

37. Y.H. Rho, K. Kanamura, T. Umegaki, $LiCoO_2$ and $LiMn_2O_4$ thin-film electrodes for rechargeable lithium batteries, Journal of The Electrochemical Society 150 (1), A107-A111 (2003)

38. Y.J. Park, J.G. Kim, M.K. Kim, et al., Fabrication of $LiMn_2O_4$ thin films by sol-gel method for cathode materials of microbattery, Journal of Power Sources 76, 41-47 (1998)

39. K.A. Striebel, A. Rougier, C.R. Horne, R.P. Reade, and E.J. Cairns, Electrochemical studies of substituted spinel thin films, Journal of The Electrochemical Society 146 (12), 4339-4347 (1999)

40. A. Rougier, K.A. Striebel, S.J. Wen, T.J. Richardson, R.P. Reade, and E.J. Cairns, Characterization of pulsed laser-deposited $LiMn_2O_4$ thin films for rechargeable lithium batteries, Applied Surface Science 134, 107-115 (1998)

41. F.K. Shokoohi, J.M. Tarascon, and B.J. Wilkens, Fabrication of thin-film $LiMn_2O_4$ cathodes for rechargeable microbatteries, Applied Physics Letter 59 (10), 2 (1991)

42. F.K. Shokoohi, J.M. Tarascon, and B.J. Wilkens, et al., Low temperature $LiMn_2O_4$ spinel films for secondary lithium batteries, Journal of The Electrochemical Society 139 (7), 1845-1849 (1992)

43. I. Uchida, H. Fujiyoshi, S. Waki, Microvoltammetric studies on single particle of battery active materials, Journal of Power Sources 68, 139-144 (1997)

44. K. Dokko, S. Horikoshi, T. Itoh, et al., Microvoltammetry for cathode materials at elevated temperatures: electrochemical stability of single particles, Journal of Power Sources 90, 109-115 (2000)

45. K. Dokko, M. Nishizawa, M. Mohamed, et al., Electrochemical studies of Li-ion extraction and insertion of $LiMn_2O_4$ single crystal, Electrochemical and Solid-State Letters 4 (9), A151-A153 (2001)

46. K. Dokko, M. Mohamed, M. Umeda, and I. Uchida, Kinetic study of Li-ion extraction and insertion at $LiMn_2O_4$ single particle electrodes using potential step and impedance methods, Journal of The Electrochemical Society 150 (4), A425-429 (2003)

47. N. Takami, H. Inagaki, T. Kishi, et al., Electrochemical kinetics and safety of 2-Volt class Li-ion battery system using lithium titanium oxide anode, Journal of The Electrochemical Society 156 (2), A128-A132 (2009)

CHAPTER II

APPLICATION OF LI-ION BATTERIES: AN IMPLANTABLE DEVICE FOR CONTINUOUS AUTOMATIC DISTRACTION OSTEOGENESIS[1]

INTRODUCTION

Lithium primary and lithium-ion (Li-ion) secondary batteries have been widely used in implantable biomedical devices due to their superior performances. The reliability and longevity of implanted devices are largely determined by the battery selection and design. The major challenge for medical battery designer comes from the uniqueness of the application; wide range of current rate, power, and environmental constraints from various implantable devices requires careful consideration to find an optimal battery for an application. Thus, to successfully select and design a medical battery, one should first identify the power/energy requirement and other design parameters for its specific application, and then thoroughly assess the reliability and the safety of the device and its battery. In this chapter, we will discuss a typical medical battery design process by a specific case of an implantable distraction device for osteogenesis.

Recent fast-developing Li-ion micro-battery technology has the potential to supply power for implantable medical devices by providing high power/energy density with flexible shapes, while also satisfying environmental requirements. As summarized in

[1] Material in this chapter is an unpublished paper in progress: M.D. Chung, S.E. Feinberg and A.M. Sastry, An Implantable Battery System for a Continuous Automatic Distraction Device for Mandibular Distraction Osteogenesis, *ASME Journal of Medical Devices* (2009).

Table 2.1, implantable batteries in medical applications and their design strategies have been studied including cardiac pacemaker, defibrillator, neurological stimulator, and drug pump [1, 2, 3, 4, 5], providing general considerations in selecting a battery for medical applications. Compared to the other medical devices, the present application for distraction osteogenesis requires a significantly higher power density during a relatively short lifetime, allowing real-time performance testing. In this paper, we present the interdisciplinary design processes for a continuous automatic distractor and the preliminary results including structural design and controls architecture, focusing on strategies for choosing power supplies to the implantable medical system via a MATLAB based battery selection algorithm [6, 7].

Distraction Osteogenesis (DO) is a surgical method of stimulating new bone formation in a controlled fashion by applying gradual tensile stress across a bisected bone gap. Since the clinical technique was first applied to craniofacial implications in 1992 by McCarthy et al. [8], most subsequent research has focused on developing more effective distraction via empirical examination with a variety of clinical parameters such as latency period, distraction rate, and distraction frequency [9, 10, 11]. The main problems of external devices include the unsightly scar formation and infection due to the transcutaneous pins, and lack of acceptance by patients. To overcome these limitations, internal or intra-oral distraction devices have been developed to become the most common clinical apparatuses in craniofacial DO [9]. In both external and internal devices, however, actuating the distraction process relies upon manual length adjustment under patients' compliance, introducing inconvenience and potential error in the procedure. More importantly, the continuous distraction process applying low strain magnitude with

multiple steps, and leading to the greatest osteogenic activity [11, 12], is restricted by the manual operation protocol which limits distraction frequency to 2-4 times per day. These limitations of current techniques motivated development of the next generation of DO devices, to realize the continuous automatic distraction for minimizing scar formation and infection, providing more acceptable protocols to patients, and accelerating bone regeneration.

In the past few years, various actuation mechanisms have been proposed to achieve automated distraction including electric motor, shape memory alloy, and hydraulic pump [13, 14, 15, 16, 17]. Comparison of these mechanisms shows electric motor offers suitable controllability, specific actuation power/energy, and biocompatibility as given in Table 2.2. For the same reasons, electric motors were used in the earliest studies to develop automatic distraction devices, including Schmelzeisen et al. [13] and Ploder et al. [14], who examined the feasibility of motor-driven distraction mechanism in animal experiments. In both studies, an electric motor-gearing actuator was used in accordance with a separately implanted power unit consisting of commercial lithium batteries and control modules. Although these previous studies showed promising results with considerable distraction lengths, they were limited to the experimental level by failing to proceed to human clinical application, mainly due to the excessive size of the device and its power supply. It is important to note that the power supplies from both studies occupied at least 50 % of the total device size. Thus, minimizing the total size of the implantable devices inevitably requires optimizing battery design and/or selection, which is the main focus of this paper.

Implanted device	Typical electrochemistry	Power requirements (mW)	Energy density* (Wh L^{-1})	Lifetime requirements
Pacemaker	Li/I_2	0.030-0.1	700	> 10 years
Defibrillator	Li/SVO	10000	780	several years
Neurological stimulator	$Li/SOCl_2$	0.3 to several	680	> 5 years
Drug pump	$Li/SOCl_2$	0.1-2	680	> 5 years
Present application	-	50-500	222	15-20 days

Table 2.1: Common applications and batteries for implanted medical deices [1,5]

	Functional / environmental requirements					
Mechanism	Force output	Accuracy	Resolution	Actuation energy density	Size	Biocompatibility
EAP	< 15 N	high (<1E6m)	medium	3.4 J/cm^3	6×6×65 for 8mm	low (high voltage ~100V/μm)
Shape memory alloy	10-40 N	medium (<1E3m)	low	3.12 J/cm^3	1.2×40×40 for 10mm	low (high temp 47~80 ºC)
Hydraulic pump	< 45 N	medium (<1E3m)	medium	external syringe driver	10×10×55 for 25mm	medium
Electric motor	0.25~3.0 mNm (transmissible)	medium (<1E3 rad)	high	11.8-118 J/cm^3	6×6×10~ 10×10×25	medium

Table 2.2: Comparison of actuation mechanisms in distraction devices [13-17]

METHODS

STRUCTURAL DESIGN AND CONTROL SCHEME

Based on the literature and current battery technology, functional requirements and environmental constraints of the implantable distraction device are chosen as follows:

(1) Minimum output distraction force (F) = 36 N [18]

(2) Distraction rate, or linear actuator speed (S) = 1 mm/day [9]

(3) Maximum distraction length (L) = 15 mm [9, 19]

(4) Thickness < 10 mm; minimum total size is desirable, current reference size is 15×15×60 mm [20]

(5) Operating temperature = 37°C (under critical temperature of 37.8°C [21])

(6) Nominal voltage 1.2~3.7V; low power consumption is desirable [22]

(7) All materials must be biocompatible, or sealed

A commercial miniature DC motor with a planetary gearhead has been selected for an actuation system for the device along with a rotary-to-linear mechanism, by using a lead screw and a miniature thrust bearing (Fig. 2.1), resulting in an average linear distraction force of 57 N, and a maximum distraction length of 15 mm. The planetary gearhead mechanism can provide 4,096:1 speed reduction to 6 mm/min, which eventually can be reduced to 1 mm/day distraction rate by additional circuit design.

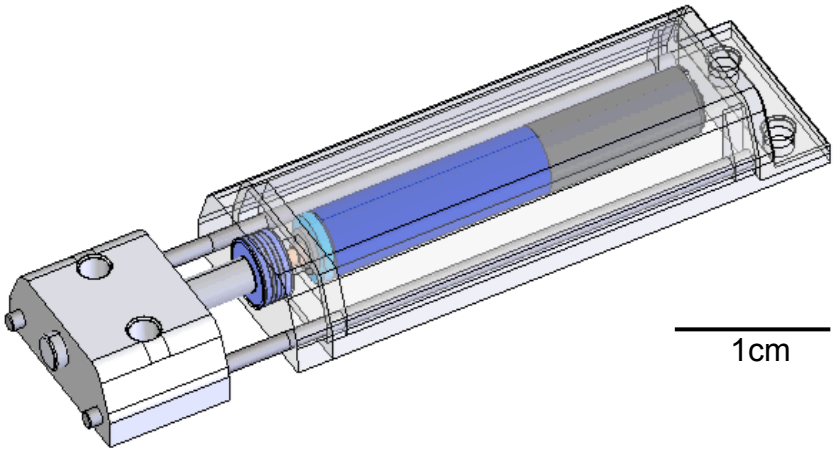

Figure 2.1: Structural design of distraction device, computer-aided design using SolidWorks®2006

Clinically, distraction protocols are divided into the latency period (time period between osteotomy and initiation of distraction), the rate and rhythm of distraction (amount and frequency of operational movement), and the maturation period (period of time the patient is maintained in rigid fixation). In this study, we focused on several aspects of the DO protocols pertaining to the rate and rhythm studied for our preliminary design of a continuous automated device. The DC motor speed and the corresponding distraction rate can be controlled intermittently by pulsed power input from the control circuit including a clock-counter and a logic gate. A schematic diagram for the control circuit is shown in Fig. 2.2. The width of a pulse, T_1, is determined by the RC oscillator that drives the clock input with frequency f by the following relationship.

$$f = \frac{1}{2.2 \times R_1 \times C_1} = \frac{4}{T_1} \tag{1}$$

The interval of the pulses, T_2, is dependent upon the pin-connections of the clock-counter into the logic gate. Thus, by simply changing the composition of the passive components and their connectivity, the power pulse can be modulated to generate different distraction parameters, such as distraction rate and frequency. For example, the most successful distraction protocol from the previous clinical and experimental studies, a distraction rate of 1 mm/day with multiple steps, can be achieved. Signal measurement using an oscilloscope can verify the power pulse modulation for a certain protocol before the custom printed circuit board (PCB) circuit fabrication.

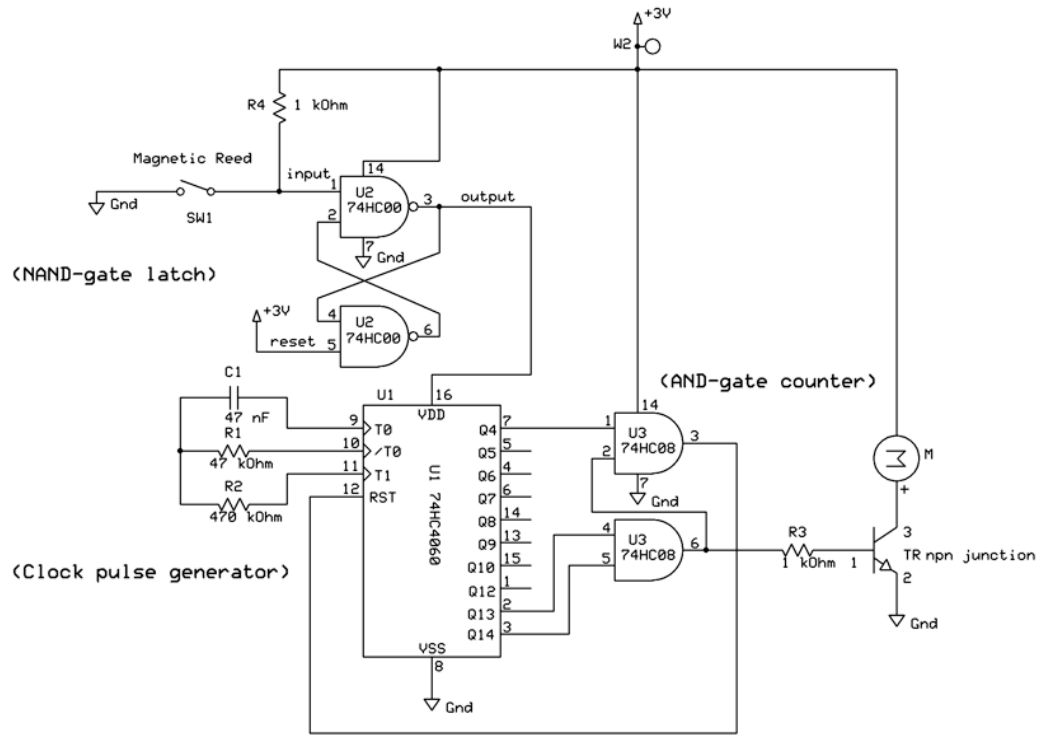

Figure 2.2: Schematic diagram of control circuit

POWER / ENERGY REQUIREMENTS AND BATTERY SELECTION

Selection of an optimal battery for the automatic distractor required accurate measurement of the power and energy consumption during a realistic operation protocol. Programmable charging procedures by a battery tester (Solartron Analytical, Hampshire, UK) were used to measure the current drains under constant voltage of 3.7 V to the actuator connected to a control circuit, and we obtained the battery requirements profile including electrochemistry, geometry, and environmental constraints as shown in Table 2.3. The electrochemistry includes cell potential, discharge profile, capacity, and lifetime of the battery. The nominal voltage required for the motor operation led to the cell potential of around 3.7 V, and the current discharge range of 0.15~60 mA with the lifetime of 15 days resulted in the capacity requirement of 70 mAh. Geometric constraints, such as volume and surface area, were decided based on the structural design (Fig. 2.1). For example, the volume for the power supply was calculated by subtracting the motor-gearhead volume from the total device volume, resulting in 1120 mm^3. The temperature and the battery operation are mutually dependent: heat dissipation from the battery may increase the temperature, and the high-operating temperature can result in self-discharge of the battery. For the motor selection, we obtained the maximum temperature of 42.2 °C from the heat dissipation of the motor operation, based on the product specification. However, the actual maximum temperature and its effect on battery performance must be examined.

The POWER (Power Optimization for Wireless Energy Requirements) is a MATLAB based battery selection algorithm for wireless MEMS applications developed by previous researchers in our lab [6, 7]. We used POWER algorithm to select candidate

batteries for the distraction device from a commercial batteries database including most lithium-based electrochemical systems with various shapes, such as cylindrical and prismatic cells. All the input parameters including energy/power requirements and geometrical constraints were entered based on the actual measurement and structural design (Table 2.4). Then, the algorithm could recommend the optimal system from the database.

BATTERY TESTING

Following battery selection, the candidate battery system was tested for the equivalent discharging profile by a complete clinical protocol of distraction osteogenesis. As described in the design criteria, distraction rate of 1mm per day was applied for the total distraction length of 15 mm, and the equivalent current discharge for this protocol was applied to the candidate battery to verify its operation under 37°C, the body temperature. All load-cycle testing was conducted with a battery tester (Maccor, Tulsa, OK) to record current and voltage of the system, and the body temperature experiments were realized by using a laboratory oven at 37°C. Batteries were fully charged until 4.2 V between each discharging cycle by a constant current mode of C/2 rate.

To simulate an averaged, typical pulse-load profile, as would be required by clinical DO protocols, a load cycle consisting of a sleep mode current of 150 μA for 150 sec followed by a pulse load of 60 mA for 100 ms (time-average current of 190 μA) was applied for 15 days. This testing protocol demonstrated the battery performed even with prolonged periods of inactivity and demanding high pulse currents during the distraction period of DO.

Electrochemistry	*Device specifications*
Cell potential	nominal voltage = 3.7 V
Discharge profile	current drains = 0.15~60 mA (sleep~pulse)
Capacity	> 70 mAh
Lifetime	~ 15 days
Geometry	
Volume	1120 mm^3
Surface area	240 mm^2
Mass	< 20 g
Shape	cylindrical, or prismatic
Environment	
Temperature	T ≈ 42.2 °C, to be measured
Biocompatibility	need to be sealed

Table 2.3: Power/energy requirements for typical distraction osteogenesis

Input parameters	Symbol	Input value
Number of devices	N	1
Current (A) vs. time	c(t)	0.1~0.15 for 20 sec
Voltage (V) vs. time	v(t)	3.0 for 20 sec
Ambient temperature (K)	T	310
Battery type (P/S)	<p> or <s>	<p>
Volume or mass optimization	<v> or <m>	<v>
Desired mass (g)	m	20
Desired volume (cm^3)	v	1.12
Max. surface area (cm^2)	a	2.4
Number of operation cycles	n_cyc	2160
Max. number of power bundle	n_loc	2

Table 2.4: Input parameters for POWER battery selection algorithm

RESULTS

BATTERY SELECTION

Energy and power data for a full DO process of 15 mm's distraction was summed per time segment to generate aggregate system parameters for battery selection. These values for capacity, energy, specific energy, energy density, specific power, and power density are listed in Table 2.5. As the device requires relatively high current up to 70 mA, high power electrochemical systems were expected as possible candidates, including those with lithium-based chemistry in various form factors. The battery selection algorithm (Table 7) recommended a polymer lithium-ion (Li-ion) rechargeable battery (UBC322030, Ultralife Batteries, Newark, NY) to satisfy the required high current discharge within minimum size.

BATTERY PERFORMANCE: PULSE DISCHARGE CHARACTERISTIC

Performance tests followed to confirm the theoretical battery selection. The pulsed-load profile simulating the actual distraction protocol was used to verify that the polymer Li-ion battery sustained the pulsed current drain for more than 15 days, and the drain was equivalent to 15 mm's distraction; during the test the current drain was regulated by control scheme, and the environmental temperature was maintained at 37°C. The voltage drop after 15 days pulsed discharge test was 0.46 V under pulsed load, resulting in 65 % capacity use out of the rated 120mAh capacity (Fig. 2.3).

Mode	Power (mW)	Voltage (V)	Current (mA)	Capacity (mAh)	Energy (Wh)	Specific energy (Wh/kg)	Energy density (Wh/L)	Specific power (W/kg)	Power density (W/L)
sleep	0.58	3.7	0.158	56.88	0.209	41.8	104.5	0.0116	0.029
active	235.69	3.7	63.70	15.29	0.057	11.4	28.5	47.14	117.85
total	236.27	3.7	n/a	72.17	0.266	53.2	133	47.15	117.88

Table 2.5: Power and energy requirements for distraction of 15 mm (active mode for 100 ms during actuation; mass (kg) = 0.005; volume (L) = 0.002)

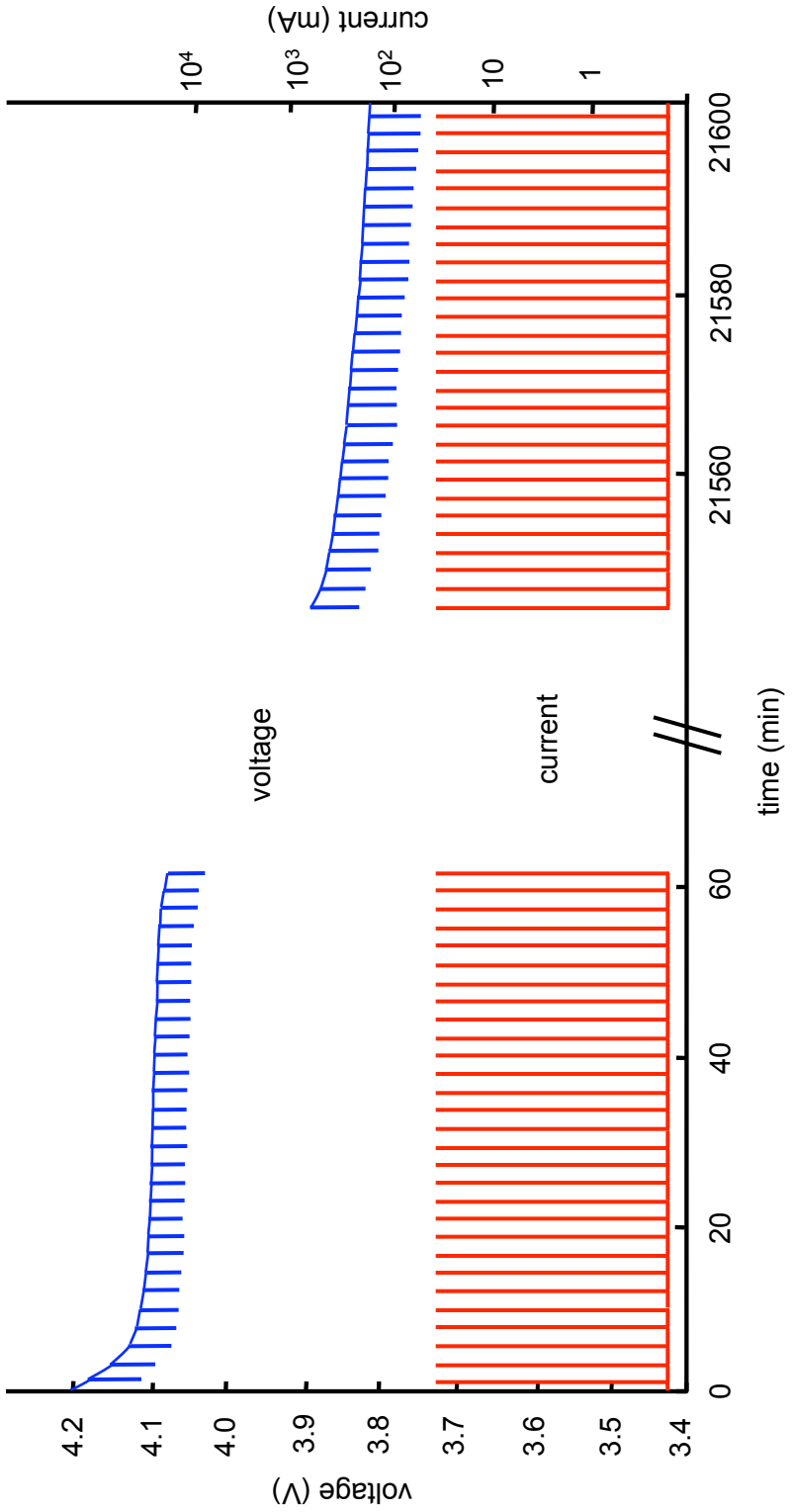

Figure 2.3: Pulsed current discharge of a single polymer Li-ion cell for over 15 days under 60 mA for 100 ms every 2.5 min with a base current drain of 150 µA

DEVICE PROTOTYPE

Based on the mechanical element design, control circuit design, and the battery selection described in the previous sections, a benchtop prototype was built to satisfy the functional requirements and biological/geometric constraints (Fig. 2.4).

DISCUSSION

The design criteria for functional requirements and environmental constraints are based on previous experimental and clinical studies which involved both discontinuous and manual distraction protocols. Some factors, such as distraction force and distraction rate, might differ for continuous automatic distraction. Indeed, Kessler et al. [12] measured lower distraction force from continuous distraction protocols by using a hydraulic pump based device on a miniature pig model (28.3 N with continuous; 76.3 N with intermittent distraction). Thus, our design goal for distraction force is conservative and sufficient to cover the variation from the model (animal/human) and the patient (age/gender/health). Also, our device can reach the distraction length of 15 mm, which covers a large portion of the patients in mandibular DO. The largest group of DO patients consists of approximately 100,000 teenagers per year suffering from severe overbite. These patients typically require 7-12 mm of distraction along one linear axis [19]. It was reported that in 305 patients (96.0%) from a total of 318 congenital micrognathia cases during 1992~2001, the distraction distance of more than 10 mm was obtained [9].

(a)

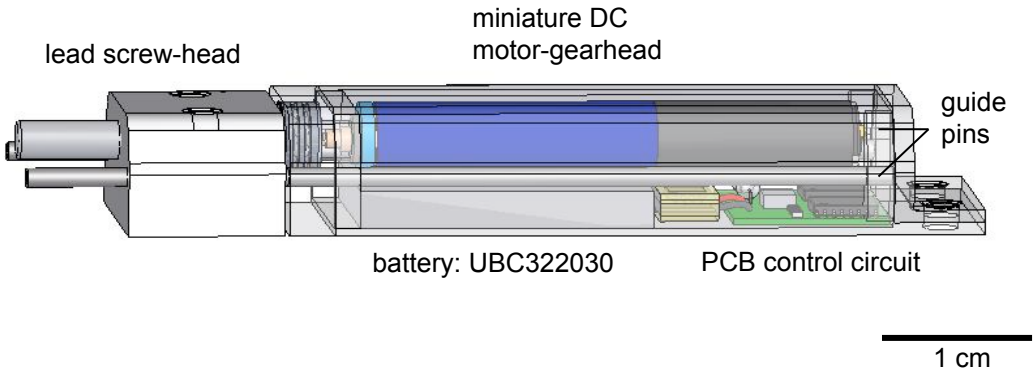

(b)

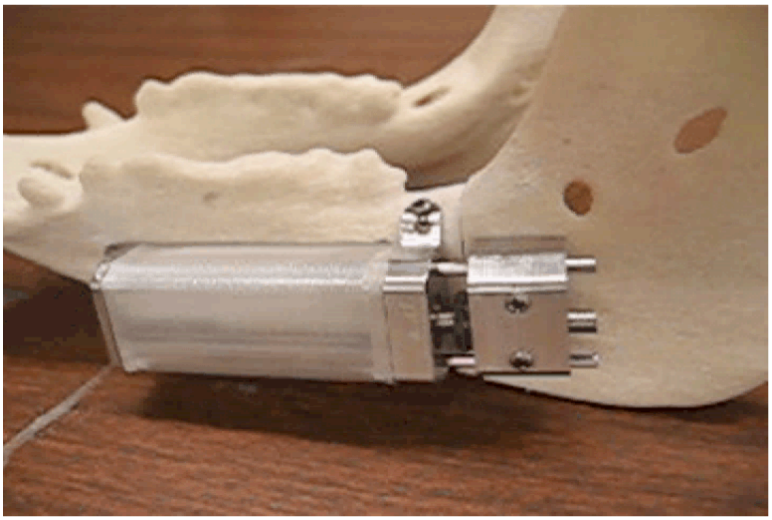

Figure 2.4: Prototype device design and fabrication: (a) computer-aided design, (b) prototype device on a mandible model

Battery type	Part number	Mass (kg)	Volume (L)	Height (mm)	Length (mm)	Width (mm)	Area (cm^2)
Polymer Li-ion	UBC322030	0.003	0.00267	3.7	31.0	21.0	16.87

Capacity (mAh)	Max. discharge current (mA)	Min/max voltage(V)	Min/max temp. (C)	Specific energy (Wh/kg)	Energy density (Wh/L)	Specific power (W/kg)	Power density (W/L)
120	240	3/4.2	-20/60	146.0	230.0	240.0	269.7

Table 2.6: Selected polymer Li-ion battery specifications

Minimizing the device size was one of the most critical parameters in this design, to allow the device to be implanted in the small space between the mandible and the skin. Especially minimizing total thickness was one of the most important design factors for human clinical application. Our current prototype based on a commercial motor and a battery system has the size of 10×20×66 mm, which is considerably smaller than previous models with the same or different actuation mechanisms. Previous models using motor-driven actuators [13, 14] had approximate size envelopes of 20×30×110 mm and 15×20×80 mm respectively only for the actuator, and they required additional and separate power supplies which considerably increased the total implantation size. This was also the case with the continuous distraction protocol of Kessler et al. [12] using a hydraulic pump that had an extra-corporeal motor and electric equipment housed in a metal box of 140×80×50 mm that had to be placed subcutaneously into the animal's back. Due to the transcutaneous syringe connection, their distraction concept was not free of scar formations and infection. As our approach chose all-in-one casing design, and required no external power supply or control module, it could accomplish one critical design goal, fully implantable distraction.

The battery selection from the commercially available battery database resulted in a polymer Li-ion battery (Table 2.6) with high specific energy and high energy density, within a thin, high aspect-ratio form factor. The main advantages of the battery are minimal thickness and favorable geometry for high power generation. As the polymer Li-ion cell employs a gel type electrolyte absorbed into a thin polymeric binder along with the active materials as $C/LiMn_2O_4$, it does not require rigid packaging for liquid

electrolytes, and thus it can provide higher energy and power density within smaller thickness, compared to the performance of typical Li-ion cells in metallic cases. Also, its high surface-volume ratio is favorable to providing improved pulse discharge characteristics, required for actuating the distraction device.

Additional safety issues with implantable medical devices should be addressed in two parts: temperature and biocompatibility. Temperature needs to be considered as a critical design parameter in two aspects; one is the allowable operating temperature of the micromotor and gearhead. Our preliminary calculation showed the maximum operating temperature remained under 42.2°C from the heat dissipation from the motor operation, satisfying the temperature limit between –30~85°C from the manufacturing specification. The second consideration is tissue damage from excessive temperature during the implantation period. Any possible high temperature due to the total heat dissipation from the motor and battery operation must be measured to verify that the maximum surface temperature of the device will remain under the critical temperature of 37.8°C, as even a very small temperature increase (less than 1°C) may affect the osteogenic activity and cause tissue damage [21]. Thus, heat-sealing with non-conductive materials, such as biocompatible polymers, should be applied to the actuator and the battery to provide thermal isolation from the surrounding osteogenic site.

All materials contacting the body must be biocompatible, or need to be sealed. Current device design involves various materials covering different components including motor-gearhead, bearing, lead screw, and battery. Especially the DC motor-gearhead must be built in a biocompatible case, due to any possible steel/bronze loss. The battery and the control circuitry also should be contained in the same casing to be

protected from the body's humid environment.

CONCLUSIONS AND FUTURE WORK

We designed a continuous automatic distraction device for mandibular DO, using a battery powered micro-motor actuator with a control circuit. A polymer Li-ion battery, UBC322030 has been selected from the commercially available batteries through a MATLAB algorithm, and tested under a pulsed discharge profile, representing the equivalent clinical distraction protocol. The test results verified the pulse capacity and performance characteristics of the polymer Li-ion battery were satisfactory to operate our device, and the POWER algorithm was confirmed as an effective tool for selecting a battery for an implantable medical device. The bench top prototype of the device is under fabrication for animal studies using miniature pig models, and eventually will be implanted for human clinical application. Custom component design and fabrication including a micro-motor and batteries can realize further minimization of the device, which might be required for younger patients (< 2 yr) or infants.

BIBLIOGRAPHY

1. J. Drews, G. Fehrmann, R. Staub, and R. Wolf, Primary batteries for implantable pacemakers and defibrillators, Journal of Power Sources 97-98, 747-749 (2001)

2. C.L. Schmidt and P.M. Skarstad, The future of lithium and lithium-ion batteries in implantable medical devices, Journal of Power Sources 97-98, 742-746 (2001)

3. B.B. Owens, Batteries for implantable biomedical devices, Plenum Press (1986)

4. M. Visbisky, R.C. Stinebring, and C.F. Holmes, An approach to the reliability of implantable lithium batteries, Journal of Power Sources 26, 185-194 (1989)

5. G.K. MacLean, P.A. Aiken, W.A. Adams, and T. Mussivand, Preliminary evaluation of rechargeable lithium-ion cells for an implantable battery pack, Journal of Power Sources 56, 69-74 (1995)

6. K.A. Cook and A.M. Sastry, An algorithm for selection and design of hybrid power supplies for MEMS with a case study of a micro-gas chromatograph system, Journal of Power Sources 140, 181-202 (2005)

7. K.A. Cook, F. Albano, P.E. Nevius, and A.M. Sastry, "POWER (Power Optimization for Wireless Energy Requirements): A Matlab based algorithm for design of hybrid energy systems", Journal of Power Sources 159, 758-780 (2006)

8. J.G. McCarthy, J. Schreiber, N. Karp et al., Lengthening the human mandible by gradual distraction, Plastic Reconstruction Surgery 89 (1-8) (1992)

9. G. Swennen, H. Schliephake, R. Dempf, H. Schierle, and C. Malevez, Craniofacial distraction osteogenesis: a review of the literature. Part I: clinical studies, International Journal of Oral and Maxillofacial Surgery 30, 89-103 (2001)

10. G. Swennen, R. Dempf, and H. Schliephake, Cranio-facial distraction osteogenesis: a review of the literature. Part II: experimental studies, International Journal of Oral and Maxillofacial Surgery 31, 123-135 (2002)

11. U. Meyer, T. Meyer, H.P. Wiesmann et al., The effect of magnitude and frequency of interfragmentary strain on the tissue response to distraction osteogenesis, Journal of Oral and Maxillofacial Surgery 57, 1331-1339 (1999)

12. P. Kessler, F.W. Neukam, and J. Wiltfang, Effects of distraction forces and frequency of distraction on bony regeneration, British Journal of Oral and Maxillofacial Surgery 43, 392-398 (2005)

13. R. Schmelzeisen, G. Neumann, and R. von der Fecht, Distraction osteogenesis in the mandible with a motor-driven plate: a preliminary animal study, British Journal of Oral and Maxillofacial Surgery 34, 375-378 (1996)

14. O. Ploder, W. Mayr, G. Schnetz, E. Unger, R. Ewers, and H. Plenk Jr, Mandibular lengthening with an implanted motor-driven device: preliminary study in sheep, British Journal of Oral and Maxillofacial Surgery 37, 273-276 (1999)

15. S. Idelsohn, J. Pena, D. Lacroix, J.A. Planell, and F.J. Gil, Continuous mandibular distraction osteogenesis using superelastic shape memory alloy (SMA), Journal of Materials Science: Materials in Medicine 15, 541-546 (2004)

16. Z. Lekston, J. Drugacz, and H. Morawiec, Application of superelastic NiTi wires for mandibular distraction, Materials Science and Engineering A 378, 537-541 (2004)

17. J. Wiltfang and P. Kebler, Continuous bone distraction using a microhydraulic cylinder: an experimental study in minipigs, British Journal of Oral and Maxillofacial Surgery 39, 2-7 (2000)

18. R.C. Robinson, P.J. O'Neal, and G.H. Robinson, Mandibular distraction force: laboratory data and clinical correlation, Journal of Oral and Maxillofacial Surgery 59, 539-544 (2001)

19. N. Crane et al., Design and feasibility testing of a novel device for automatic distraction osteogenesis of the mandible, Proceedings of the ASME Design Engineering Technical Conference 2A, 611 (2004)

20. C. Guerrero et al., Intra-oral bone distraction device, USPTO #5885290

21. T. Suzuki, T. Hirayama, K. Aihara, and Y. Hirohata, Experimental studies of moderate temperature burns, Burns 17 (6) 443-451 (1991)

22. D. Linden, and T.B. Reddy, Handbook of batteries, 3rd Ed., McGraw-Hill (2002)

CHAPTER III

IMPLEMENTATION OF EXPERIMENTAL FINDINGS TO SIMULATION[1]

INTRODUCTION

Recent efforts in large-scale vehicle electrification have intensified interest in selecting, characterizing, and validating of the performance of cathode materials. Among present candidates, the $Li_xMn_2O_4$ spinel ($0 < x < 1$) system is of high interest because of its high voltage, low cost, and low toxicity, and thus has been widely studied experimentally and by electrode modeling and simulations [1, 2, 3]. Key results from these studies, including simulations of reaction fluxes and intercalation-induced stresses, were found to be highly dependent upon material properties, especially Li ionic diffusivity. Though constant diffusion coefficients were presumably used in the previous simulation studies, the dependence of Li-ion diffusivity on its concentration or state-of-charge (SOC) has been investigated within $Li_xMn_2O_4$ by several studies, which found the diffusion coefficient values vary up to two order of magnitude between $x = 0$ to 1. Assumptions of spherical or ellipsoidal electrodes in previous battery modeling are subject to careful investigation by studying how the irregular but realistic electrode shapes of different active materials affect the electrochemistry. To improve electrode

[1] Material in this chapter is an unpublished paper in progress: M.D. Chung, X. Zhang, J.H. Seo and A.M. Sastry, Implementing Realistic Geometry and Measured Diffusion Coefficients into Single Particle Electrode Modeling Based on Experiments with Single Particle LiMn2O4 Spinel, *Journal of The Electrochemical Society* (2009).

modeling, and eventually to predict battery cell performance and failure with higher fidelity, it is essential to accurately characterize these parameters.

The diffusion coefficient of $Li_xMn_2O_4$ spinel ($0 < x < 1$) has been measured as a function of Li-ion concentration in a number of studies. Bulk, composite cells (Table 3.1 [4, 5, 6, 7, 8, 9]) and thin films (Table 3.2 [10, 11, 12, 13, 14]) were mostly used to measure the diffusion coefficients by cyclic voltammetry (CV), electrochemical impedance spectroscopy (EIS), and potential step chronoamperometry (PSCA) or potentiostatic intermittent titration technique (PITT). As shown in Table 3.1 and 3.2, there are substantial disagreements in the values, with discrepancies of up to three orders of magnitude. While disagreement of up to two orders of magnitude between composite electrodes and thin films may be attributed to the additives in composite electrodes such as binders and conducting agents, diverse electrode structures, from crystalline microstructure to cluster macrostructure, also play an important role. Dokko *et al.* [15, 16], for example, have shown that crystalline grain and particle size have significant effects on diffusion coefficients measured from microprobe-cycled single crystal and single particle electrodes. Thus, $Li_xMn_2O_4$ cathode materials of any type have different micro- to macro- structures, and so have different diffusion properties depending on their manufacturing and fabrication process and conditioning. So, accuracy of homogeneous electrode simulation can be limited because of these different diffusion properties. More realistic simulation requires a new experimental approach to measure diffusion coefficients from *known* electrodes as a form of isolated particles, involving only the active cathode materials in the electrochemical process, and also to identify realistic electrode geometry.

D (cm^2/s)	x	Technique	Ref.
0.5 to 1.5 $\times 10^{-9}$	0 and 0.5 ≤ x ≤ 1.0	PITT	[4]
0.66 to 1.4 $\times 10^{-10}$	0.1 ≤ x ≤ 0.8	PSCA	[5]
4.89 $\times 10^{-9}$	0.2 ≤ x ≤ 0.8	CV	[6]
0.19 to 3.1 $\times 10^{-11}$	0.1 ≤ x ≤ 0.8	EIS	[7]
5 $\times 10^{-10}$	0 ≤ x ≤ 1.0	CV	[8]
2.2 $\times 10^{-9}$	0.17 ≤ x ≤ 1.0	CV	[9]

Table 3.1: Review of diffusion coefficients of Li-ion in bulk, composite electrodes $Li_xMn_2O_4$

D **(cm^2/s)**	**x / potential**	**Technique**	**Deposition**	**Ref.**
3.5×10^{-11}	-	CV	PLD	[10]
6.1×10^{-12}	4.0 V	PSCA	ESD	[11]
0.3 to 5.5×10^{-11}	3.9 ~ 4.3 V	PSCA	ESD	[12]
0.47 to 5.96×10^{-12}	1.4	CV, PSCA	sol-gel	[13]
0.463 to 1.04×10^{-11}	0.5	CV	PLD	[14]
10^{-12} to 10^{-10}	3.85 ~ 4.3 V	EIS		
1.9×10^{-12} to 8×10^{-11}	3.85 ~ 4.5 V	PITT		

Table 3.2: Review of diffusion coefficients of Li-ion in thin film $Li_xMn_2O_4$

Our research aims to bridge experiments to modeling by implementing realistic parameters from experimental samples in order to simulate the electrochemical reaction within a single particle cathode model. It also uses the same experimental samples to validate the simulation models through measuring electrochemical and/or mechanical responses, such as strains. The present work is mainly focusing on implementing experimental results through simulation. The overall research sequence including present and ongoing work is shown in Fig. 3.1. In this study, we have the following specific objectives:

1. To develop an experimental model using dispersed particle electrodes.
2. To perform electrochemical tests including CV and PITT to measure their diffusion coefficients using the dispersed particle model.
3. To generate 3D particle model geometry by processing the surface scan image obtained from atomic force microscopy (AFM).
4. To implement the new parameters of actual particle geometry and diffusion coefficients into the previously developed single particle cathode model, and evaluate their influences on the simulation of reaction fluxes and intercalation-induced stresses.

METHODS

EXPERIMENTAL METHODS

The dispersed particle based electrodes of $Li_xMn_2O_4$ were prepared on gold foil current-collecting substrates. We adopted and modified a method similar to that developed by Totir et al. [8] and Clemencon et al. [17] to fabricate pure cathode particle

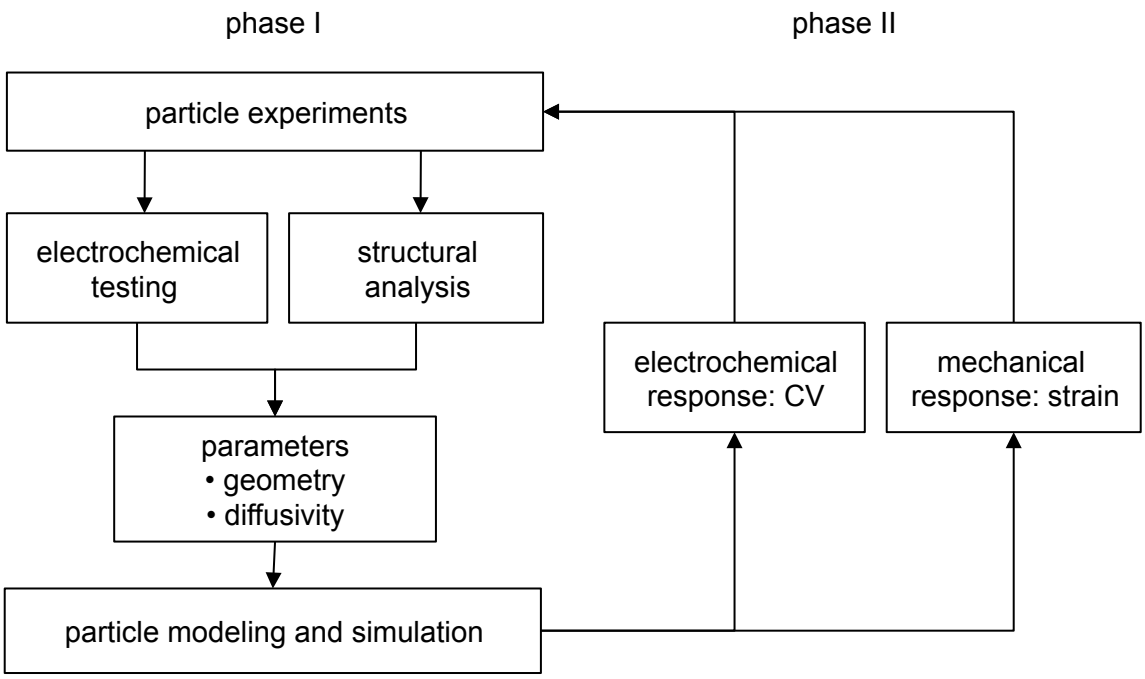

Figure 3.1: A schematic diagram of research sequence to bridge experiments to modeling (phase I – present work), and to validate the model (phase II)

electrodes in the absence of any additives. Electrodes prepared by Totir et al. [8] were lithium transition metal oxide particles closely packed on Au foils, while the electrode samples prepared by Clemencon et al. [17] were dispersed $LiCoO_2$ particles made for AFM measurement. In this study, similar efforts were made to isolate the $LiMn_2O_4$ particles, but with a higher degree of dispersion by using ultrasonication. We prepared the electrode samples with the following steps: (1) mixing raw $LiMn_2O_4$ powder (99.5%, Alfa Aesar) into acetone suspension with a ratio of 1% wt., (2) dispersing the $LiMn_2O_4$ powder in acetone suspension by an ultrasonic wave for 60 min., (3) depositing the $LiMn_2O_4$ particles onto a gold foil (99.99%, Aldrich) from a drop of suspension, and (4) gradually pressing the particles against a counter gold foil up to 20 kpsi using a preprogrammed material compression tester (Instron). Once the counter gold piece was carefully removed, the particle-topped electrodes were examined by scanning electron microscopy (SEM) for larger scale observation, and AFM for micro scale characterization. AFM (MultiMode coupled with a NanoScope controller, Veeco) on single particle electrodes was used to reconstruct the 3D particle geometry with Matlab and Hypermesh for image processing and meshing.

For the electrochemical measurements, the particle cathode substrates were assembled in a Swagelok cell containing electrolyte of 1 M $LiPF_6$ in ethylene carbonate (EC) and diethyl carbonate (DEC) (1:1 in volume, Merck) with lithium foil counter electrodes, all inside Ar-filled glove box (< 1 ppm O_2 and H_2O). The assembled cells were rested for about an hour, and then measured for open circuit potential (OCP) before galvanostatic cycling at a rate of C/50 between the OCP to 4.5 V using a VMP3 potentiostat/galvanostat (Bio-Logic). Cyclic voltammograms were collected between 3.5

and 4.5 V at a sweep rate varied from 0.05 to 1.0 mV/s. For the measurement of PITT, a potential step of 10mV was applied between 3.85 and 4.30V while the current transition was measured until the absolute current value reached below 10nA at the equilibrium state. All electrochemical tests were conducted at room temperature (298K).

ANALYTICAL METHODS

The peak currents measured from CV versus the scan rates were used to calculate the diffusion coefficients. The relationship was derived from a diffusion equation describing spherical electrodes [18] as

$$\frac{\partial C_O(r,t)}{\partial t} = D_O\left[\frac{\partial^2 C_O(r,t)}{\partial r^2} + \frac{2}{r}\frac{\partial C_O(r,t)}{\partial r}\right] \tag{1}$$

where C_o is the concentration of the diffusion component (lithium ions), D_o is the diffusion coefficient of Li-ion, r is the distance from the center of the electrode, and t is the time. This equation can be solved by an initial condition such that the concentration of lithium ion is uniformly given by the bulk concentration at the beginning of the electrochemical reaction, and two boundary conditions. One boundary condition can be obtained from Nernst equation with potential sweep given as

$$\frac{C_O}{C_R} = \frac{f_R}{f_O}\exp\left[\frac{nF}{RT}\left(E_i - E^0\right)\right]\exp\left[\frac{nF}{RT}\nu t\right] \tag{2}$$

where f_R and f_o are activity coefficients of reduction and oxidation substances (i.e. Li-ion), n is the charge number, E_i and E^0 are the initial and the standard potentials, ν is the potential scan rate, F is Faraday's constant, R is the gas constant, and T is absolute temperature. Another boundary condition is the equilibrium condition at the electrode surface as

$$D_O \frac{\partial C_O(r_o,t)}{\partial r} + D_R \frac{\partial C_R(r_o,t)}{\partial r} = 0 \tag{3}$$

This diffusion equation at the spherical electrode was numerically solved by Frankenthal and Shain [19] for the peak current at room temperature (25 °C) as

$$i_p = (8.81 \times 10^5) n^{3/2} A D_O^{1/2} C_O^{\,0} v^{1/2} \partial C_O(r_o,t)/C_O^{\,0} \tag{4}$$

where i_p is the peak current in A (amperes), A is the electrode surface area in cm^2, D_o is the diffusion coefficient, in cm^2/s, $C_o^{\,0}$ is the bulk concentration in $mole/cm^3$, and ν is in V/s. The extrapolated value of the term $\partial C_O(r_o,t)/C_O^{\,0}$ was obtained from the experimental data in [19]. The peak current in spherical electrodes for Li-ion diffusion can be estimated as

$$i_p = (2.74 \times 10^5) n^{3/2} A D_O^{1/2} C_O^{\,0} v^{1/2} \tag{5}$$

According to the diffusion theory of a single spherical electrode [20, 21], the current response to a step potential can be expressed by a Cottrell equation for a short time region as

$$i(t) = nFA(C_S - C_O^{\,0})(D_{app}/\pi t)^{1/2} \tag{6}$$

and by the finite diffusion approximation for a longer time region as

$$i(t) = \frac{2nFA(C_S - C_O^{\,0})D_{app}}{r} \exp\left(-\frac{\pi^2 D_{app} t}{r^2}\right) \tag{7}$$

Where r is the radius of a spherical particle, C_s the concentration of Li-ion at the surface, $C_o^{\,0}$ the bulk Li-ion concentration inside a particle, and D_{app} the apparent diffusion coefficient. In the long time approximation in Eq. (7), the chemical diffusion coefficient

can be evaluated from the slope of a linear plot of ln *i(t)* vs. *t* without information about concentration when the radius of the particle is known.

RESULTS AND DISCUSSION

ELECTRODE CHARACTERIZATION

The dispersed $LiMn_2O_4$ particles embedded on a gold foil were observed in a series of SEM images as in Fig. 3.2. The average size of cathode particles was 2~4 μm; higher magnification images revealed the particle is flat crystal surface as shown in Fig. 3.2(b). Surface area of the dispersed particle electrode was estimated from a number of SEM photographs to be 0.0237 cm^2 for 3 mm × 3 mm sample substrate. 3D images from AFM showed individual particle geometry on a flat gold foil (Fig. 3.3(a)). The sectional analysis of the particle surface profile confirmed the particles were securely connected to the current collecting gold substrate as shown in Fig. 3.3; this was also indicated by good galvanostatic and cyclic voltammetry behavior of the electrode.

ELECTROCHEMICAL BEHAVIORS

$LiMn_2O_4$ particle electrodes were cycled at constant current rate of C/50 (~10 $\mu A/cm^2$) between OCP to 4.5 V against lithium foil counter electrodes for the initial formation cycle. The galvanostatic voltage profile showed well-defined potential plateaus at 3.94 and 4.13 V indicating that the removal of a Li-ion takes place in two steps due to Li-ion ordering around 4 V versus lithium, which is in good agreement with previous galvanostatic measurements of $Li_xMn_2O_4$ ($0 < x < 1$) composite [4, 6] and thin film

(a)

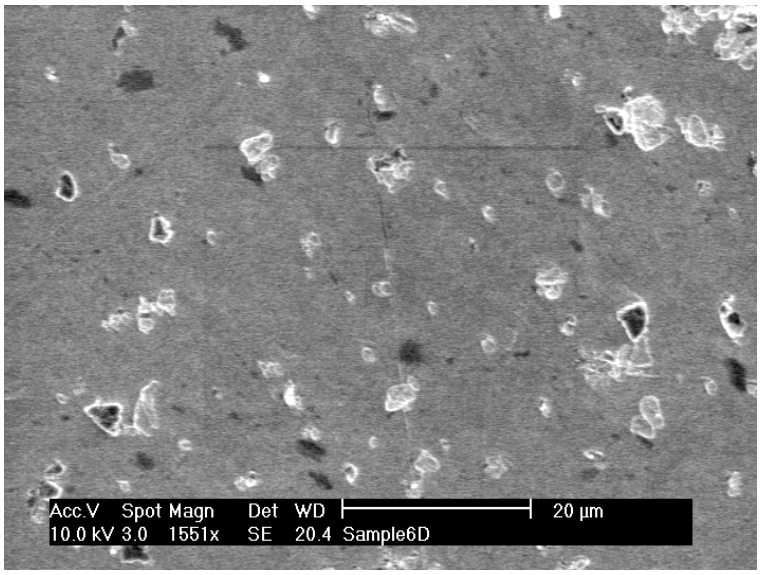

(b)

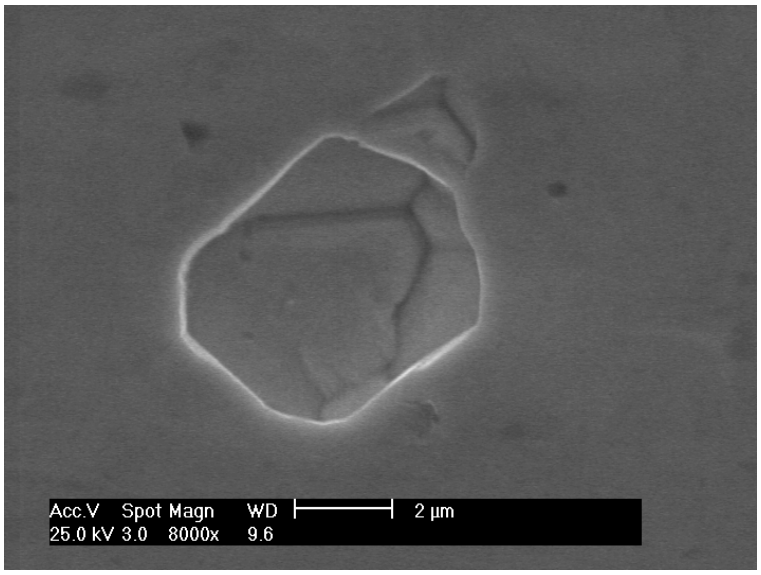

Figure 3.2: SEM images of (a) $Li_xMn_2O_4$ dispersed particle electrode and (b) single particle with a crystal surface parallel to a gold substrate

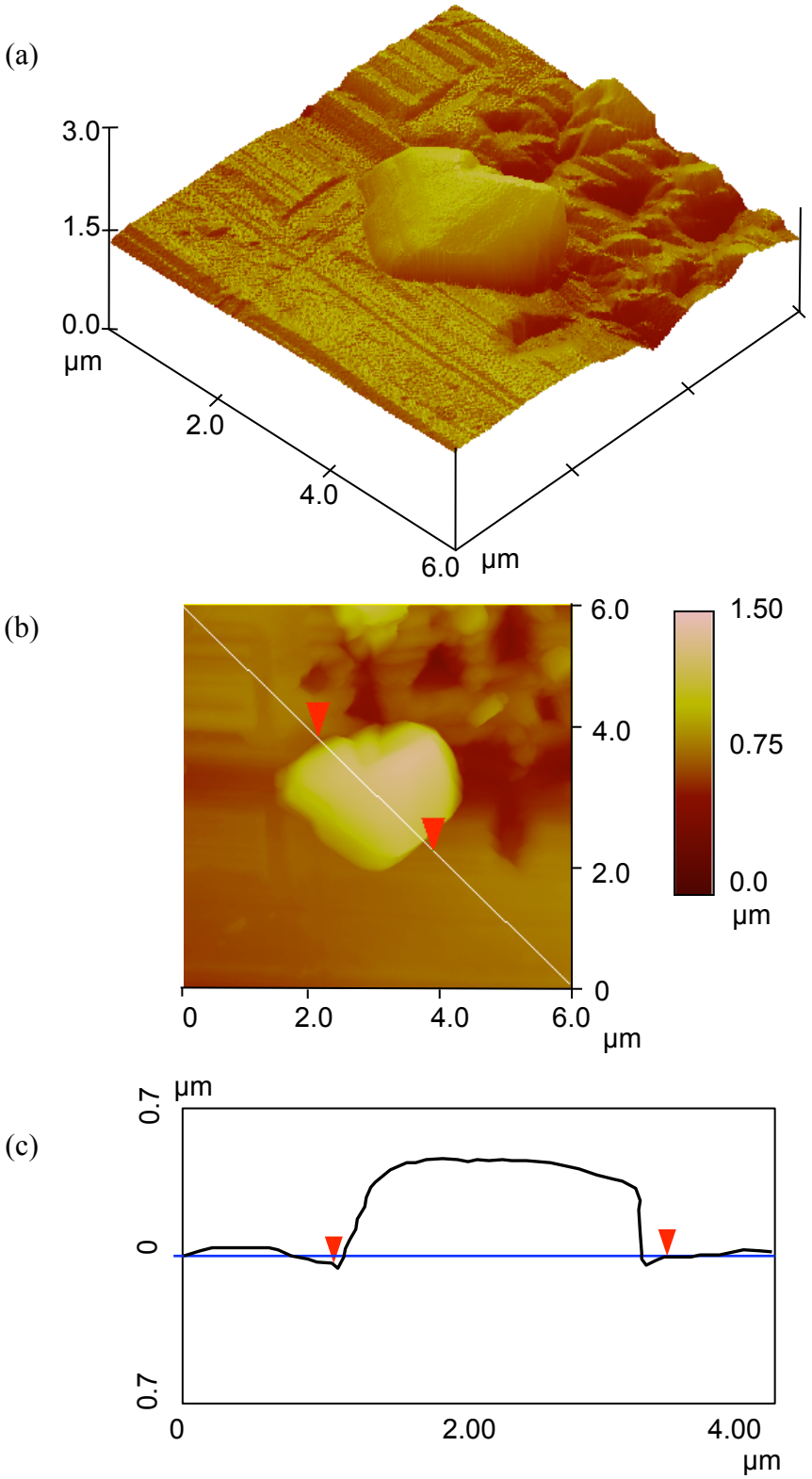

Figure 3.3: AFM images of single particles by tapping mode on a scan size of 6 × 6 µm: (a) 3D image, (b) 2D profile of surface height, and (c) section analysis on a cross section line indicated by red arrows. The tuning frequency of the tapping probe was 277.15 kHz and the scan rate was 0.5 Hz

electrodes [14]. The two-phase (de)insertion process of Li-ion at the tetrahedral sites in the spinel structure was also confirmed by the two well-defined peaks from cyclic voltammograms at lower scan rates (Fig. 3.4). The first anodic peak potential was 4.01 V and the second anodic peak potential was 4.14 V, and for the cathodic peaks, potentials were 3.99 V and 4.11 V versus lithium counter electrode, which were determined in Fig. 3.4(b). The relative heights of the two peaks in Fig. 3.5 are consistent with those reported for CV measurements of composite cells [5, 22] and microvoltammetry of single particle electrodes [16, 23], while the reverse trend has been reported in the case of $LiMn_2O_4$ thin film fabricated with pulsed laser deposition [10]. Because the electrodes used in this study were pure $LiMn_2O_4$ spinel particles without carbon and binder (as in the case of single particle studies in [16, 23]), our CV results can provide a good comparison and answer a question raised in the thin film study [10]; the reverse trend of relative peak heights from the thin film electrodes might originate from characteristics of the thin film micro structures and its fabrication condition.

DIFFUSIVITY MEASUREMENTS

Both CV and potentiostatic intermittent titration technique (PITT) were used for estimating chemical diffusion coefficients for Li-ion intercalation within the particle $Li_xMn_2O_4$ electrodes. The trends of peak current versus potential scan rate from the cyclic voltammograms are shown in Fig. 3.5. The peak current values of both Li-ion (de)insertion processes are linearly dependent on the square root of the scan rate ($v^{1/2}$) as derived in Eq. (5) for diffusion-controlled reactions. With a given charge number, the bulk concentration of Li-ion in $LiMn_2O_4$ (given as $C_o^0 = 0.02378$ mol/cm^3 from the

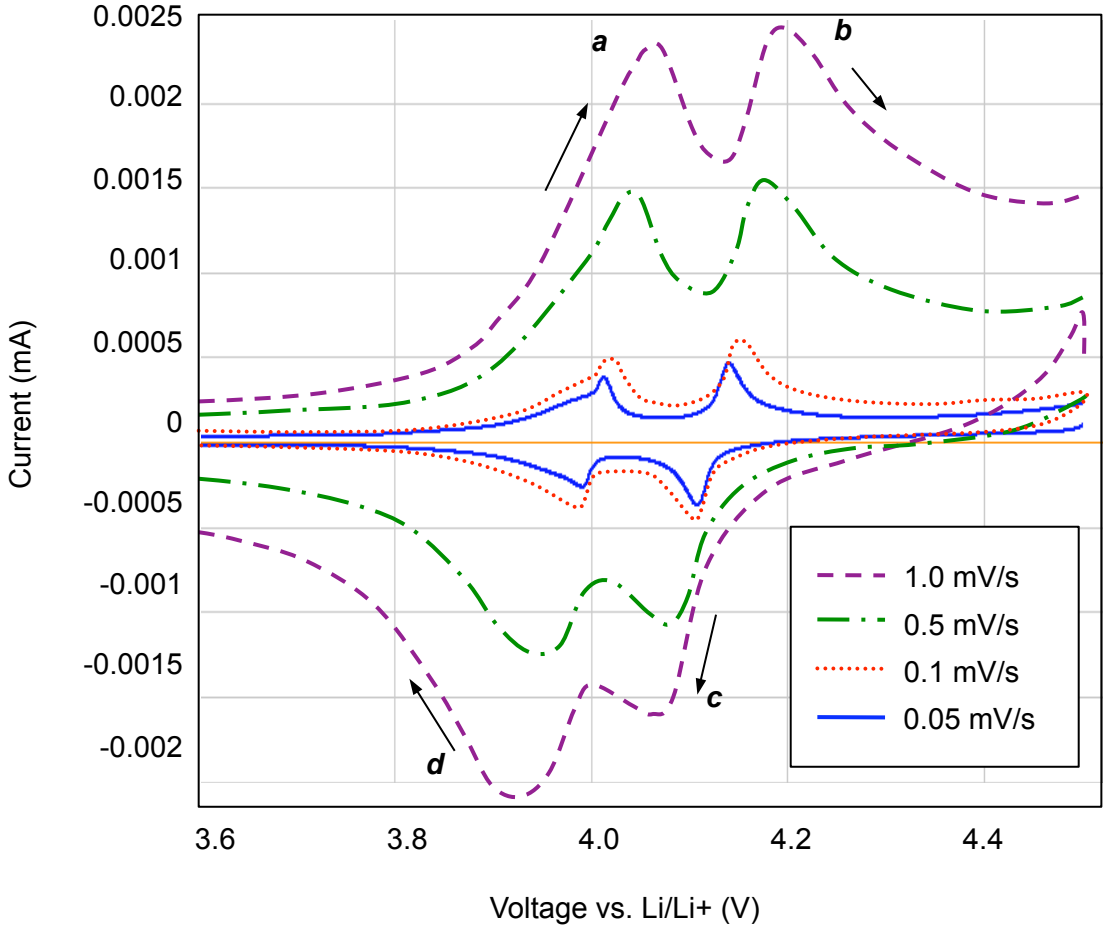

Figure 3.4: Cyclic voltammetry of a $Li_xMn_2O_4$ dispersed particle electrode at scan rates from 0.01 to 1.0 mV/s. The current peaks are labeled by a, b for oxidation (charging) and c, d for reduction (discharging) peaks respectively

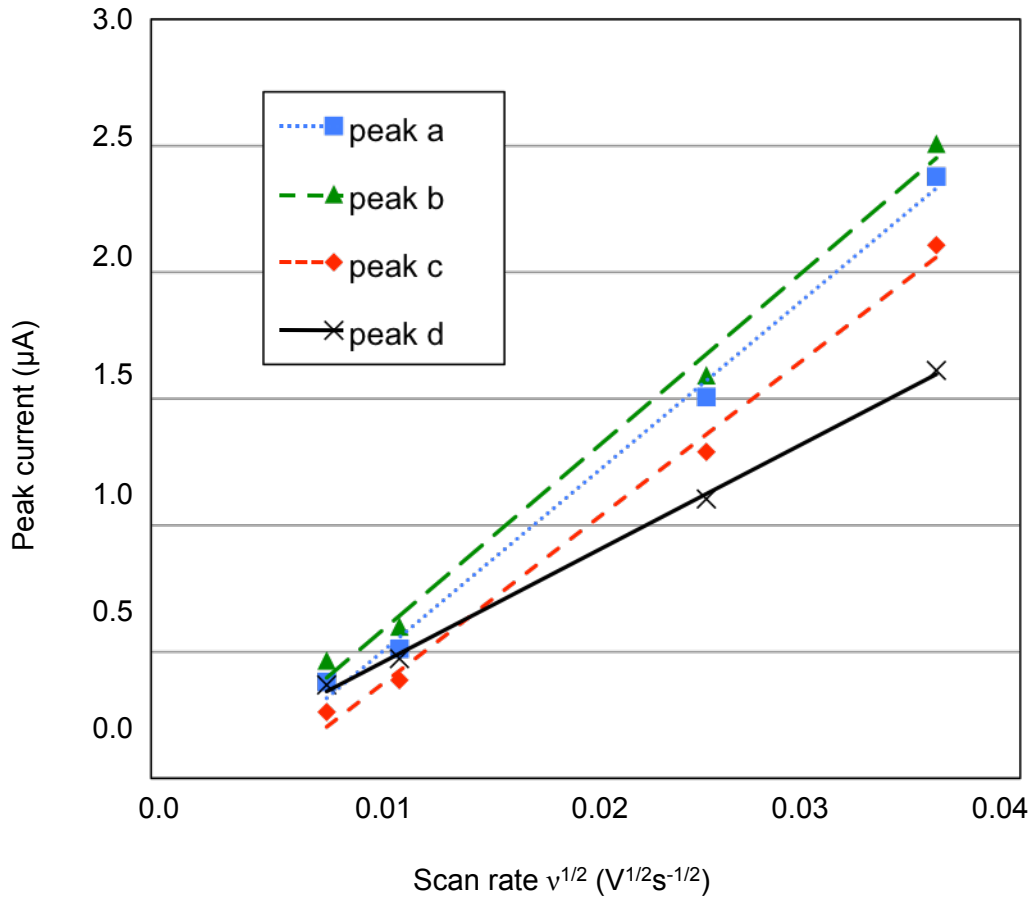

Figure 3.5: Peak current vs. square root of scan rate ($\nu^{1/2}$) with peaks a, b, c, and d as labeled in cyclic voltammograms in Fig. 3.4

theoretical density of spinel), and the estimated electrode surface area from SEM/AFM images, we can calculate the Li-ion diffusion coefficients from the slope of peak current versus the square root of the scan rate ($v^{1/2}$) in Fig. 3.5. The results are listed in Table 3.3. The diffusion coefficients for four different peaks are very similar, ranging between 1.70×10^{-11} and 2.94×10^{-11} cm^2/s; the oxidation process shows slightly higher diffusion coefficients than reduction, which is in good agreement with previous measurements of Li-ion diffusivity using CV [6, 14].

The PITT method [24] was also used to determine the chemical diffusion coefficients of Li-ions in the $Li_xMn_2O_4$ spinel particles. As discussed in a previous diffusion study [25], the use of Eq. (7) can provide more reliable diffusion coefficients than Eq. (6), because the long time approximation of Eq. (7) is not easily affected by the surface roughness of the particle. The Cottrell equation usually depends on the surface condition, as this semi-infinite diffusion model is applicable only for a short time range when the thickness of the diffusion layer is generated at the interface. Additionally, the current response from the short time region often shows nonlinear behavior. For most of the potential steps between 3.85 and 4.30 V, nonlinear current responses were observed from the short time range while consistent linear behaviors of the current were shown at the long time regions from the Cottrell plots. Thus, in this study we used Eq. (7), the long time approximation of the potential stepped current response for the measurement of Li-ion diffusion coefficients.

The resulting diffusion coefficients determined for the $Li_xMn_2O_4$ ($0 < x < 0.85$) when the electrode potential was between 3.85 and 4.30 V (vs. Li/Li+) are shown in Fig. 3.6 for both the Li-ion insertion and extraction processes. The trends of the diffusion

Oxidation (anodic reaction)	**D_o (cm^2/s)**
$LiMn_2O_4 \rightarrow Li_{0.5}Mn_2O_4$ (peak **a**)	2.94×10^{-11}
$Li_{0.5}Mn_2O_4 \rightarrow \lambda\text{-}MnO_2$ (peak ***b***)	2.83×10^{-11}
Reduction (cathodic reaction)	
$\lambda\text{-}MnO_2 \rightarrow Li_{0.5}Mn_2O_4$ (peak ***c***)	1.70×10^{-11}
$Li_{0.5}Mn_2O_4 \rightarrow LiMn_2O_4$ (peak ***d***)	2.40×10^{-11}

Table 3.3: Diffusion coefficients of Li-ion in dispersed particle $Li_xMn_2O_4$ electrode calculated from CV

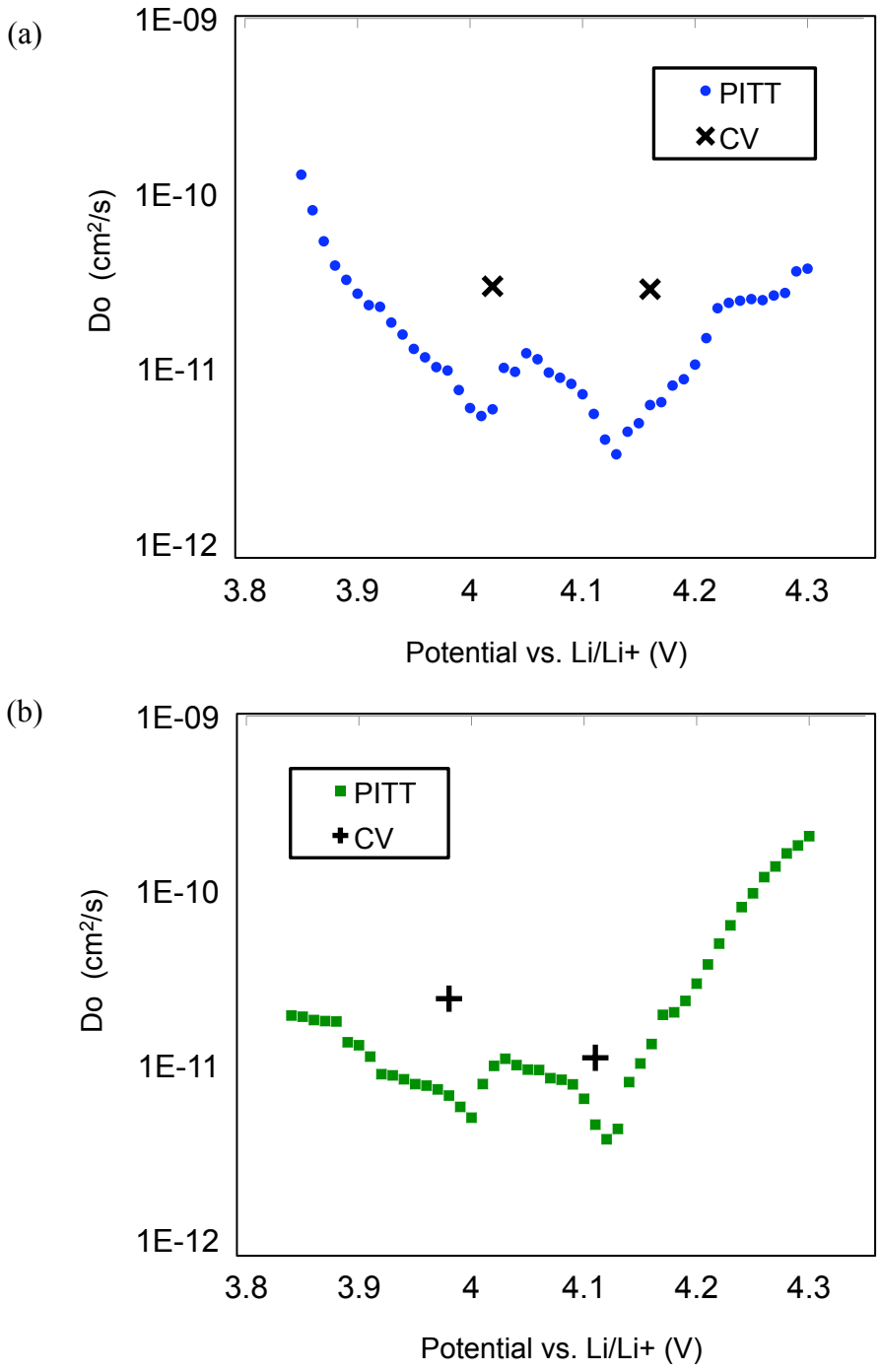

Figure 3.6: Diffusion coefficients of Li-ion as a function of electrode potentials vs. Li/Li+ obtained from PITT for (a) oxidation (anodic), and (b) reduction (cathodic) compared to the values obtained from CV as labeled

coefficients are similar to those reported by other researchers who studied either powder-based composite cells or thin film electrodes [7, 12, 13, 14, 16], but the values ranging between 3.22×10^{-12} and 1.22×10^{-11} cm^2/s (3.95 to 4.15 V) are closer to the case of thin film measurements (shown in Table 3.2) than the results from the composite cells ranging 10^{-11} to 10^{-9} cm^2/s (Table 3.1). Fig. 3.6 also shows the diffusion coefficients from CV at the peak current potentials of 4.01 and 4.14 V for the anodic reaction (charging), and of 3.99 and 4.11 V for the cathodic reaction (discharging). The values from CV and PITT deviate within one order of magnitude for each peak; the CV results show slightly higher diffusion coefficients. For both (de)insertion processes, the diffusion coefficients from PITT show strong dependency on the Li-ion concentration within the potential range (3.85~4.30 V).

SINGLE PARTICLE SIMULATION

A single particle $LiMn_2O_4$ electrode model was used to simulate the Li-ion diffusion and the intercalation-induced stress, following prior work [1, 2], but including new parameters of realistic particle geometry and diffusion coefficients. In our previous modeling, the Li-ion diffusion, expressed as the diffusion flux, was given by [1]

$$J = -D\left(\nabla c - \frac{\Omega c}{RT}\nabla \sigma_h\right) \tag{8}$$

where c is the Li-ion concentration, σ_h is the hydrostatic stress, D is the diffusion coefficient, R is the general gas constant, and T is temperature. From this equation, the Li-ion species mass conservation equation was obtained as

$$\frac{\partial c}{\partial t} + \nabla \cdot \left[-D\left(\nabla c - \frac{\Omega c}{RT} \nabla \sigma_h \right) \right] = 0 \tag{9}$$

At the particle boundary, the diffusion flux can be expressed by the current density i_n as

$$J = -D\left(\nabla c - \frac{\Omega c}{RT} \nabla \sigma_h \right) = \frac{i_n}{F} \tag{10}$$

where F is Faraday's constant.

The Li-ion diffusion kinetics are derived by Butler-Volmer equation as

$$J = \frac{i_n}{F} = \frac{i_0}{F}\left(\exp\left[\frac{(1-\beta)F}{RT}\eta \right] - \exp\left[-\frac{\beta F}{RT}\eta \right] \right) \tag{11}$$

where i_0 is exchange current density, η is surface overpotential, and β is symmetry factor. The exchange current density is given by

$$i_0 = Fk(c_l)^{1-\beta}(c_\theta)^{1-\beta}(c_s)^{\beta} \tag{12}$$

where c_l is the Li-ion concentration in the electrolyte, c_s is the Li-ion concentration on the surface of the solid electrode, c_θ is the concentration of available vacant sites on the surface ready for lithium intercalation (c_{max} - c_s), and k is a reaction rate constant [2]. Input parameters for these diffusion equations are given in Table 3.4. The intercalation-induced stress model was derived by thermal stress analogy to the constitutive equation between stress and strain as

$$\varepsilon_{ij} = \frac{1}{E}\left[(1+\nu)\sigma_{ij} - \nu\sigma_{kk}\delta_{ij} \right] + \frac{\tilde{c}\Omega}{3}\delta_{ij} \tag{13}$$

where ε_{ij} are strain components, σ_{ij} are stress components, E is Young's modulus, ν is Poisson's ratio, $\tilde{c} = c - c_0$ is the Li-ion concentration change, and Ω is the partial molar

Parameter (symbol)	**Value**
Li-ion concentration in the electrolyte (c_l)	1000 mol/m^3 [a]
maximum Li-ion concentration (c_{max})	2.37×10^4 mol/m^3 [a]
reaction constant (k)	1.9×10^{-9} m$^{5/2}$s^{-1}mol$^{-1/2}$ [a]
potential cycling rate (v)	0.5 mV/s
diffusion coefficient (*D as function of c*)	0.03~1.28 × 10^{-10} cm^2/s [b]

[a] Ref. 2
[b] Experimental results (Fig. 3.6)

Table 3.4: Parameters for the single particle electrode simulation

volume of lithium [1]. A Young's modulus E = 10 GPa and a partial molar volume Ω = 3.497×10^{-6} m^3/mol were assumed. Eq. (9) and Eq. (13) are coupled through the Li-ion concentration and the stress components.

In the former studies [1, 2], the particle geometry was assumed as either spheres or ellipsoids, and the stress localization due to sub-particle structures such as crystalline grains and grain boundaries were not considered in the stress calculation. Irregular particle geometry as shown in SEM (Fig. 3.2) and AFM (Fig. 3.3) images can result in localized stress distribution and concentration, which may cause local particle fracture and eventual electrode failure. As shown in Fig. 3.7(a), a 3D particle model was reconstructed based on AFM scan data from a dispersed $LiMn_2O_4$ particle sample, and then imported into the simulation tool COMSOL Multiphysics. The initial condition for electrode concentration was applied based on the initial OCP. The boundary conditions were applied either for Li-ion flux determined by Eq. (11) and free traction force on the top surface between a particle electrode and electrolyte, or for zero Li-ion flux and point-fixed displacement on the bottom surface between a particle electrode and gold substrate (Fig. 3.7(b) and 3.7(c)).

The simulation results of reaction flux and stress at a surface point on the grain boundary are shown in Fig. 3.8. The time history of reaction flux shown in Fig. 3.8(a) follows a pattern similar to those experimentally measured from CV (Fig. 3.4). The trend of von Mises stress generation in Fig. 3.8(b) at the same surface point also follows this pattern. However, the maximum von Mises stress of 78.6 MPa measured at the second peak is significantly higher than the maximum von Mises stress of 43.2 MPa measured from spherical/ellipsoidal particle simulation in a previous study [1] for the following

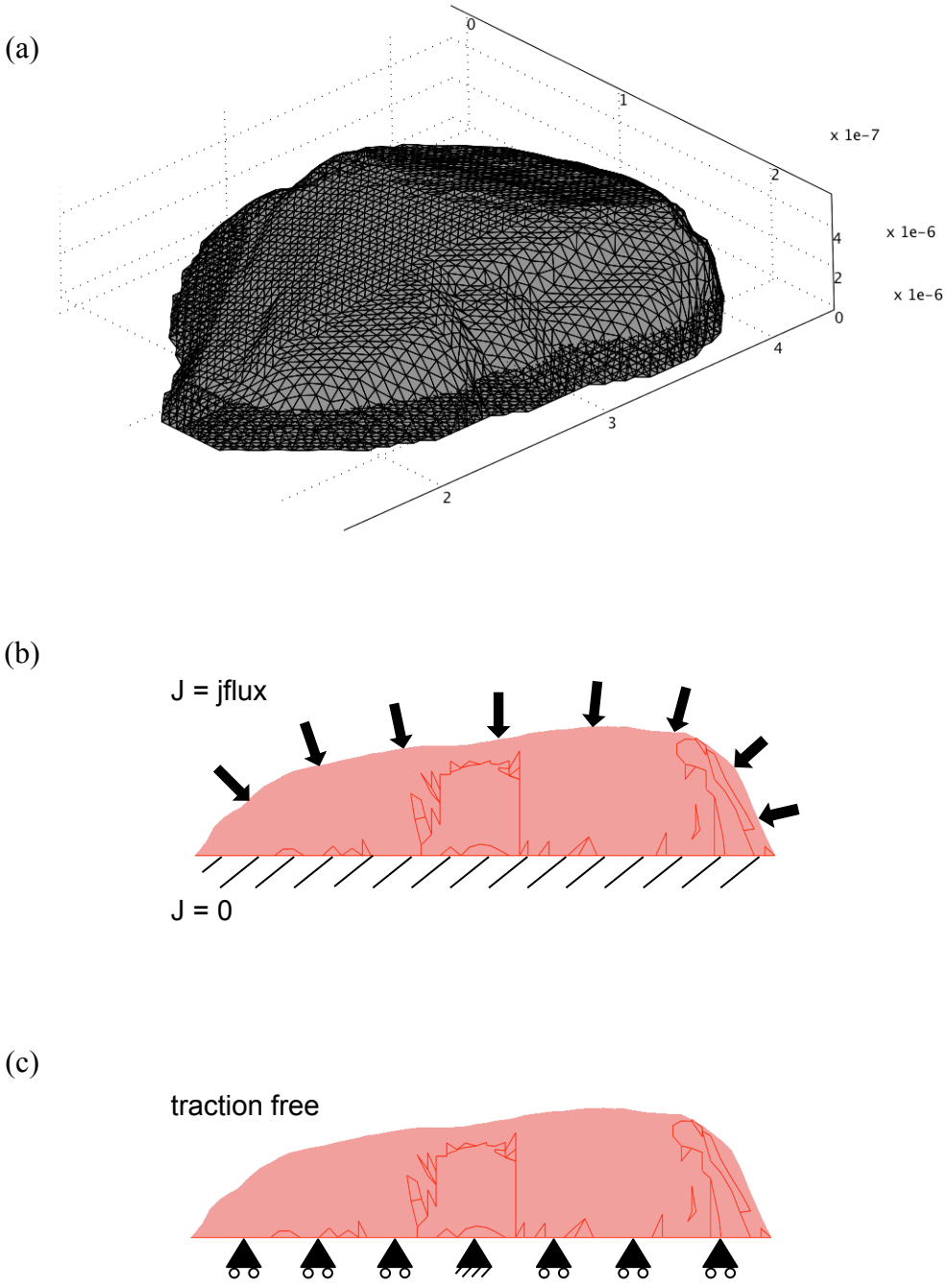

Figure 3.7: 3D particle model reconstructed from AFM data: (a) imported mesh structure, (b) boundary conditions for diffusion, (c) boundary conditions for stress-strain

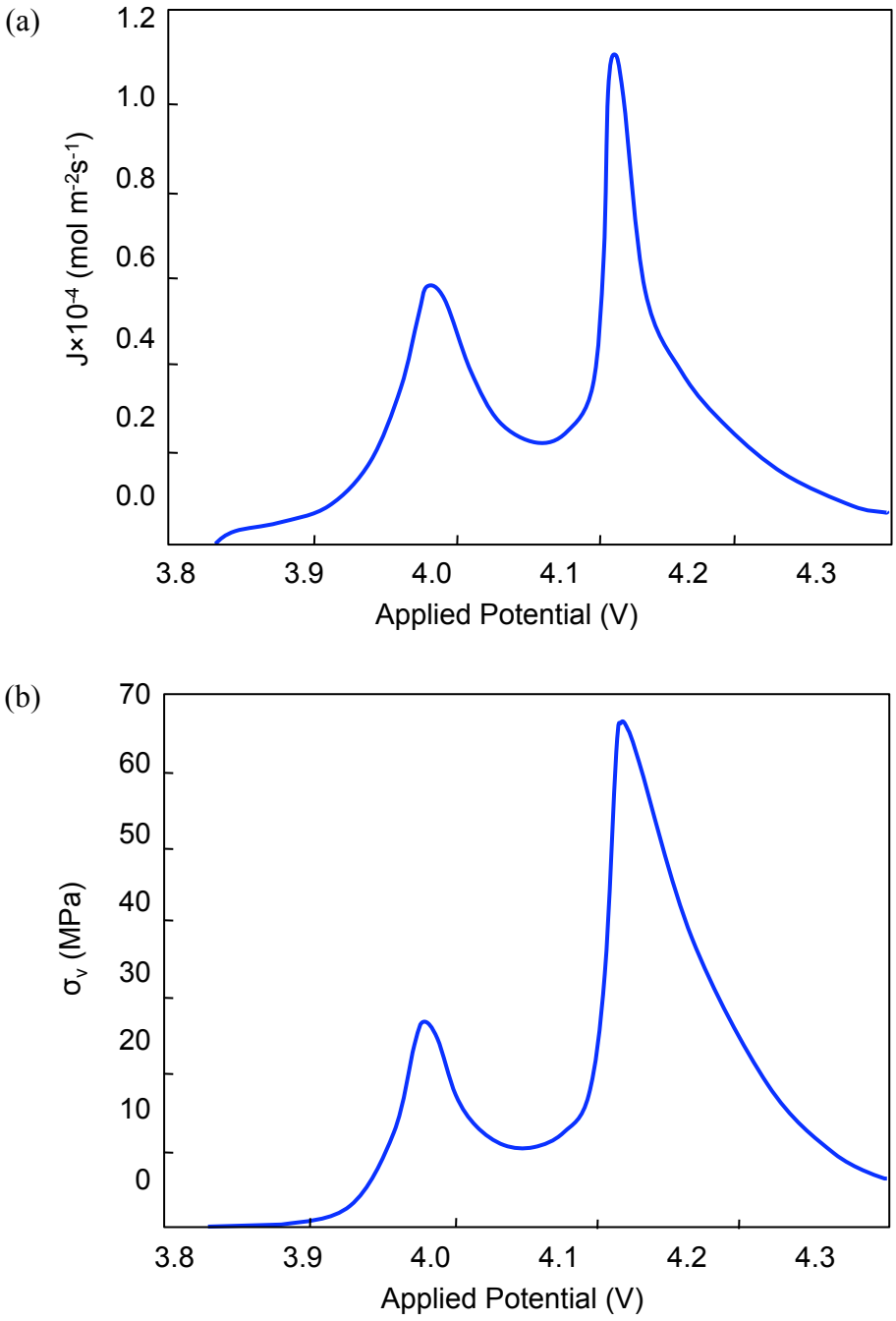

Figure 3.8: Simulation with a realistic particle geometry and concentration dependent diffusion coefficients with scan rate ν = 0.5mV/s: (a) reaction flux at the grain boundary on the particle surface, (b) von Mises stress at the grain boundary on the particle surface

(c)

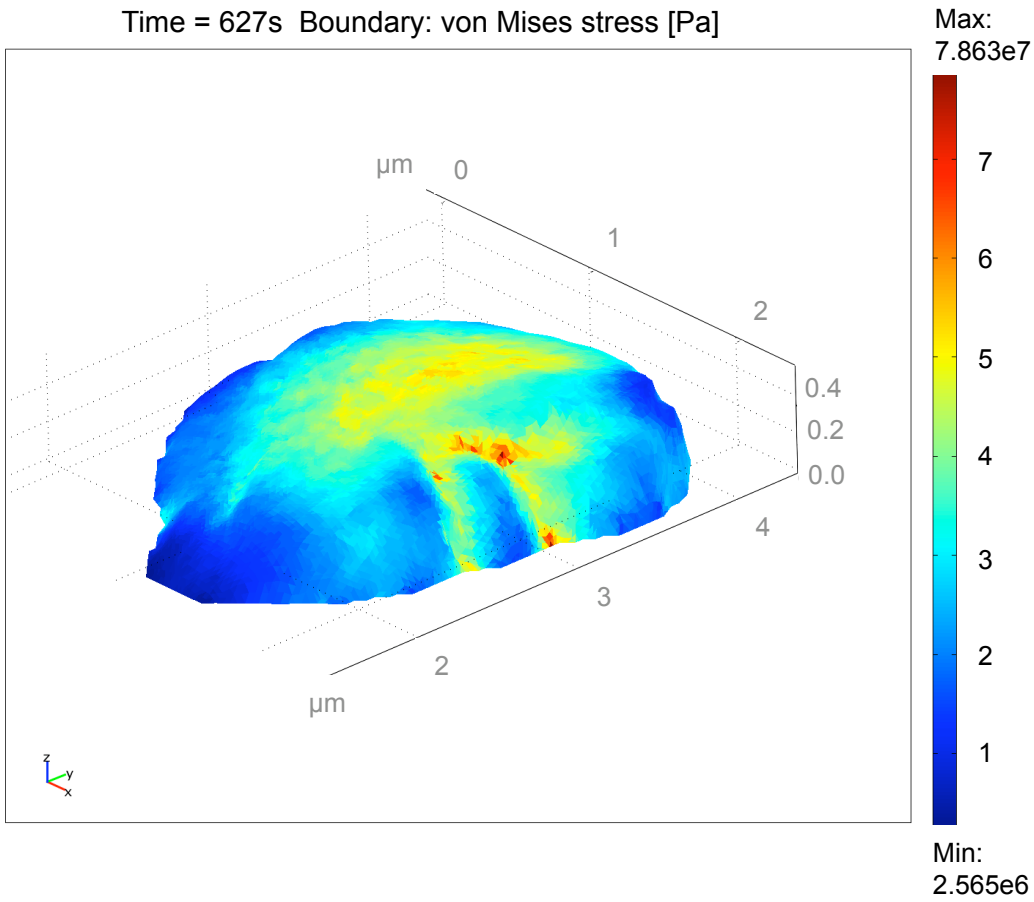

Figure 3.8: Simulation with a realistic particle geometry and concentration dependent diffusion coefficients with scan rate ν = 0.5mV/s: (c) von Mises stress distribution on the particle surface

reasons. First, the diffusion coefficients measured in this study were lower than the constant value used in the former study, especially at the potential regions associated with peak currents, so they can be attributed to higher concentration gradients and thus higher stress generation. Second, intercalation-induced stress was concentrated at the grain boundaries on the particle surface geometry, as shown in Fig. 3.8(c). Stress distribution on the particle surface shows that (i) larger stress occurs around the center of the flat particle surface where the diffusion path is shorter and the concentration change is larger, and (ii) the irregular particle geometry leads to local stress concentration, especially through the grain boundaries. Although stress distribution can be predicted, the quantitative estimation of stress generation from this simulation is limited as it is based on a homogeneous particle assumption. To improve the fidelity of the single particle modeling, inhomogeneous and anisotropic Li-ion diffusion within a particle consisting of multiple crystalline grains and complex grain boundaries should be considered.

CONCLUSIONS AND FUTURE WORK

Irregular but realistic particle surface geometry and diffusion coefficients were measured from dispersed single particles of $LiMn_2O_4$ cathode material. Dispersed cathode particle samples were suitable for investigating morphology of the particles using AFM. 3D particle models including local structures of crystal grains and their boundaries were reconstructed from AFM scanning data. The single particle samples also showed good cyclic behavior and the diffusion coefficients were measured using both CV and PITT. Concentration dependent diffusion coefficients ranging between 3.22×10^{-12} and

1.22×10^{-11} cm^2/s were implemented into single particle simulation with realistic particle geometry. The simulation results with concentration dependent diffusion coefficients showed that the $LiMn_2O_4$ particle could be under higher intercalation-induced stress due to slower diffusion around 4.01 and 4.13 V. Also, simulation with irregular particle shape showed that higher stress concentration could occur at the grain boundaries on the particle surface.

BIBLIOGRAPHY

1. X.C. Zhang, W. Shyy, and A.M. Sastry, Numerical simulation of intercalation-induced stress in Li-ion battery electrode particles, Journal of The Electrochemical Society 154 (10), A910-A916 (2007)

2. X.C. Zhang, A.M. Sastry, and W. Shyy, Intercalation-induced stress and heat generation within single lithium-ion battery cathode, Journal of The Electrochemical Society 155 (7), A542-A552 (2008)

3. J. Christensen and J. Newman, A mathematical model of stress generation and fracture in lithium manganese oxide, Journal of The Electrochemical Society 153 (6), A1019-A1030 (2006)

4. D. Guyomard and J.M. Tarascon, Li metal-free rechargeable $LiMn_2O_4$/carbon cells: their understanding and optimization, Journal of The Electrochemical Society 139 (4), 937-948 (1992)

5. H. Kanoh, Q. Feng, Y. Miyai, and K. Ooi, Kinetic properties of a Pt/lambda-MnO_2 electrode for the electroinsertion of lithium ions in an aqueous phase, Journal of The Electrochemical Society 142 (3), 702-707 (1995)

6. Y. Xia, H. Takeshige, H. Noguchi, and M. Yoshio, Studies on a Li-Mn-O spinel system (obtained by melt-impregnation) and a cathode for 4V lithium batteries Part 1. Synthesis and electrochemical behavior of $Li_xMn_2O_4$, Journal of Power Sources 56, 61-67 (1995)

7. H. Kanoh, Q. Feng, T. Hirotsu, and K. Ooi, AC impedance analysis for Li+ insertion of a Pt/lambda-MnO_2 electrode in an aqueous phase, Journal of The Electrochemical Society 143 (8), 2610-2615 (1996)

8. D.A. Totir, B.D. Cahan, and D.A. Scherson, Electrochemical characterization of lithiated transition metal oxide cathode particles in the absence of carbon, binders and other additives, Electrochimica Acta 45, 161-166 (1999)

9. D. Zhang, B.N. Popov, and R.E. White, Modeling lithium intercalation of a single spinel particle under potentiodynamic control, Journal of The Electrochemical Society 147 (3), 831-838 (2000)

10. K.A. Striebel, C.Z. Deng, S.J. Wen, and E.J. Cairns, Electrochemical behavior of $LiMn_2O_4$ and $LiCoO_2$ thin films produced with pulsed laser deposition, Journal of The Electrochemical Society 143 (6), 1821-1827 (1996)

11. M. Nishizawa, T. Uchiyama, K. Dokko, K. Yamada, T. Matsue, and I. Uchida, Electrochemical studies of spinel $LiMn_2O_4$ films prepared by electrostatic spray deposition, Bulletin Chemical Society Japan 71, 2011-2015 (1998)

12. D. Shu, K.Y. Chung, W.I. Cho, and K.-B. Kim, Electrochemical investigations on electrostatic spray deposited $LiMn_2O_4$ films, Journal of Power Sources 114, 253-263 (2003)

13. S.R. Das, S.B. Majumder, and R.S. Katiyar, Kinetic analysis of the Li+ ion intercalation behavior of solution derived nano-crystalline lithium manganate thin films, Journal of Power Sources 139, 261-268 (2005)

14. S.B. Tang, M.O. Lai, and L. Lu, Study on Li+-ion diffusion in nano-crystalline $LiMn_2O_4$ thin film cathode grown by pulsed laser deposition using CV, EIS and PITT techniques, Materials Chemistry and Physics 111, 149-153 (2008)

15. K. Dokko, M. Nishizawa, M. Mohamedi, et al., Electrochemical studies of Li-ion extraction and insertion of $LiMn_2O_4$ single crystal, Electrochemical and Solid-State Letters 4 (9), A151-A153 (2001)

16. K. Dokko, M. Mohamed, M. Umeda, and I. Uchida, Kinetic study of Li-ion extraction and insertion at $LiMn_2O_4$ single particle electrodes using potential step and impedance methods, Journal of The Electrochemical Society 150 (4), A425-429 (2003)

17. A. Clemencon, A.T. Appapillai, S. Kumar, and Y. Shao-Horn, Atomic force microscopy studies of surface and dimensional changes in Li_xCoO_2 crystals during lithium de-intercalation, Electrochimica Acta 52, 4572-4580 (2007)

18. P. Delahay, New Instrumental Methods in Electrochemistry, Interscience Publishers, New York, N.Y., p. 60 (1954)

19. R.P. Frankenthal and I. Shain, Diffusion currents at spherical electrodes, Journal of The American Chemical Society 78 (13), 2969-2973 (1956)

20. A.J. Bard and L.R. Faulkner, Electrochemical Methods, Chap. 5, John Wiley & Sons, New York (1986)

21. W. Jost, Diffusion in Solids, Liquids, Gases, p. 45, Academic Press, New York (1960)

22. J.M. Tarascon, W.R. Mckinnon, F. Coowar, T.N. Bowmer, G. Amatucci, and D. Guyomard, Synthesis conditions and oxygen stoichiometry effects on Li insertion into the spinel $LiMn_2O_4$, Journal of The Electrochemical Society 141 (6), 1421-1431 (1994)

23. I. Uchida, H. Fujiyoshi, and S. Waki, Microvoltammetric studies on single particles of battery active materials, Journal of Power Sources 68, 139-144 (1997)

24. C.J. Wen, B.A. Boukamp, R.A. Huggins, and W. Weppner, Thermodynamic and mass transport properties of "LiAl", Journal of The Electrochemical Society 126 (12), 2258-2266 (1979)

25. T. Nishina, H. Ura, and I. Uchida, Determination of chemical diffusion coefficients in metal hydride particles with a microelectrode technique, Journal of The Electrochemical Society 144 (4), 1273-1277 (1997)

CHAPTER IV

CHARACTERIZATION OF CATHODE MATERIALS FOR LI-ION BATTERIES

INTRODUCTION

Accurate characterization of battery materials is as important as their discovery and fabrication. Only by understanding the characteristics of the materials can we further improve their properties, and reliably estimate their electrochemical, kinetic, and mechanical behaviors to predict long-term cell behavior and lifetime of Li-ion batteries. In this chapter, we discuss material characterization techniques to determine anisotropic and inhomogeneous aspects of cathode materials.

Lithium-ion (Li-ion) battery cells are comprised of Li-ion intercalation compounds as the cathode and anode materials. As a cell is cycled, Li-ions travel back and forth between the positive and negative electrodes, inserted or extracted from interstitial sites between atomic layers within the active materials (Fig. 4.1). In this schematic diagram of the Li-ion intercalation process, $Li_{1-x}MO_2$ represents the metal oxide cathode with M for metal elements, such as Co, Ni, or Mn, and Li_xC is the carbon-based anode, such as graphite, where Li-ion atomic ratio x changes from 0 to 1. The Li-ion cathode materials are typically metal oxides with energetically favorable lattice structures to host Li-ions, such as layered structures (e.g. LiCoO2), or three-dimensional tunneled structures (e.g. $LiMn_2O_4$ and $LiFePO_4$). In Table 4.1, typical intercalation

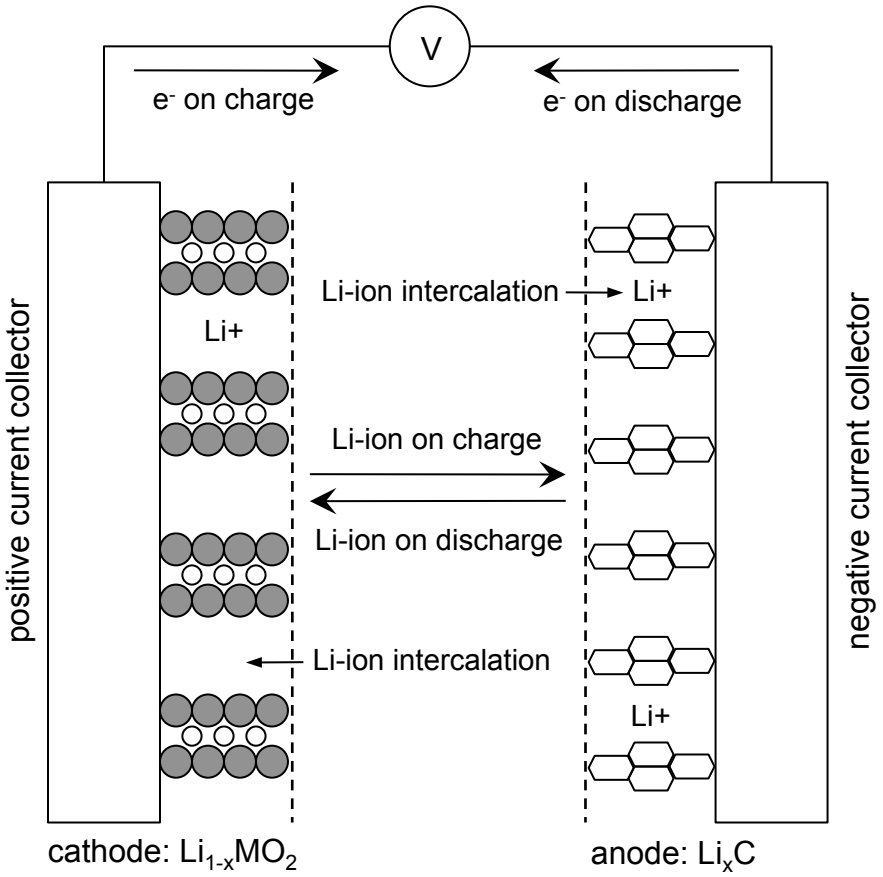

Figure 4.1: Schematic diagram of Li-ion intercalation process [1]

Material	Lattice structure	Synthesis method	Specific capacity (mAh/g)	Nominal voltage vs. Li (V)
$LiCoO_2$	Layered	Electrochemical lithium extraction	155	3.88
$LiNiO_2$	Layered	Pyrolysis from LiOH and $Ni(OH)_2$	200	3.55
$LiMn_2O_4$	Tunneled, spinel	Calcination from Mn_3O_4 and Li_2CO_3	120	4.00
$Li[Ni_{1/3}Co_{1/3}Mn_{1/3}]O_2$	Layered	Carbonate coprecipitation	160	3.75
$LiFePO_4$	Tunneled, olivine	Microwave processing	110	3.50

Table 4.1: Intercalation compound cathode materials: metal oxide insertion compounds [1-5]

compound cathode materials are summarized with their lattice structures, specific capacity, and nominal voltages [1, 2, 3, 4, 5]. These materials not only have different electrochemical properties, but also have distinguishing atomic, molecular structures and characteristics. Understanding the material characteristics of metal oxide compounds is important to accurately measure the original material properties, such as chemical composition, crystallography, and physical parameters of size and shape. Also, using material characterization techniques we can monitor direct or indirect phenomena within a intercalation compound during electrochemical cycling, such as its lattice expansion, degradation, and solid electrolyte interface (SEI) formation.

A number of characterization techniques serve different roles in battery material research. We can divide them into three groups: the first and the most straightforward way of characterizing a material is to directly observe its micro/nano-structure through an electron microscope, such as a scanning electron microscope (SEM) and a transmission electron microscope (TEM). Their highly magnified images provide physical parameters, such as particle size and crystal shape, of a cathode material. The second class of characterization tools is based on either diffractometry or spectroscopy; when X-ray is used, X-ray diffraction (XRD) or X-ray Photoelectron Spectroscopy (XPS) can be done; when photon is used, Raman spectroscopy can work; and when neutron is the source, there is neutron diffraction. These diffraction / spectroscopy techniques can measure elemental compositions, chemical states, and crystallinity. Finally, the atomic force microscope (AFM) represents another type of characterization as it can measure three-dimensional surface profiles from a sample material.

In this study, we analyze how nano/micro-structures of crystalline grains and grain boundaries construct each primary particle from different chemical compositions. Several characterization techniques including SEM, TEM, XRD and AFM were used on particle-based metal oxide cathode materials with the following objectives:

1. To characterize cathode particles as anisotropic and inhomogeneous materials by using various characterization tools including SEM / TEM / AFM (in a particle scale, order of μm).
2. To characterize internal structure of crystalline grains and grain boundaries within cathode materials using TEM (in a crystalline scale, order of nm).
3. To measure lattice expansion or strain associated with Li-ion intercalation within $LiMn_2O_4$ spinel cathode using XRD (in a lattice scale, order of nm).

METHODS

Cathode materials characterized in this study are $LiMn_2O_4$ spinel, $LiFePO_4$ olivine, and $Li[Ni_{1/3}Co_{1/3}Mn_{1/3}]O_2$ (L333). Different samples of isolated particles, aggregates, or bulk particles mixed with binders and conductive agents were prepared from the original powder materials for various characterization techniques introduced in the previous section.

SAMPLE PREPARATION

Electron microscopy samples were prepared by dispersing $LiMn_2O_4$, $LiFePO_4$ and L333 cathode particles on carbon meshes; TEM samples were additionally embedded in epoxy media (Araldite®6005) and then sliced using microtome cutting. XRD samples were prepared from bulk-composite cathode electrodes; $LiMn_2O_4$ powder was mixed with polyvinylidene fluoride (PVdF) binder (5% wt.) and carbon black (5% wt.) in N-Methyl-2-pyrrolidone (NMP) solvent, then the slurry was pasted on a Celgard separator film and dried for two days inside of an Ar-filled dry box. The cathode film was assembled with a lithium metal anode in a Swagelok cell; the electrolyte was 1M $LiPF_6$ in EC:DEC (1:1). The $LiMn_2O_4$/Li cell was then cycled to various voltage levels to obtain $Li_xMn_2O_4$ samples under different states of charge, x = 0, 0.5, and 1. The potential (vs. Li) was maintained in the sample cell until $LiMn_2O_4$ cathode film was extracted and dried for XRD. For AFM setup, $LiMn_2O_4$ particles were placed on a gold current collecting layer (~100μm) on top of the scanner head. After gradual compression the cathode materials maintained physical and electric contact with the gold substrate.

CHARACTERIZATION TECHNIQUES

Cathode powder morphology was observed by a Hitachi S-4800 SEM and a Hitachi H-9500 TEM, both equipped with an energy dispersive spectroscopy (EDS) to determine the elemental distribution. The phase structure and lattice expansion of Li-ion insertion compounds were analyzed by X-ray diffraction on a Rigaku diffractometer with Cu Kα radiation. AFM (MultiMode coupled with a NanoScope controller, Veeco) on dispersed single particles was used to measure polycrystalline particle surface.

RESULTS AND DISCUSSION

SCANNING ELECTRON MICROSCOPY (SEM)

SEM images of $LiMn_2O_4$ in Fig. 4.2 show two primary particles with a similar size but different shapes; one particle is closely packed to form a sphere or an ellipsoid (Fig. 4.2(a)), but the other particle has a branched, irregular structure. Both particles consist of about 10 crystalline grains with the size of 1~4 μm, and each crystalline has an individual orientation. High-resolution SEM images in Fig. 4.3 show a closer view of the crystal surface with a number of crystal cavities, aligned in one direction. Fig. 4.3 (b) shows grain boundaries between three crystalline grains; the crystals are aligned in three directions indicated by crystal surface formation and cavities on each surface. Based on these images, we can conclude that 1) $LiMn_2O_4$ primary particles have a variety of forms depending on the size and number of crystal grains, and 2) the directionality of crystals and grain boundaries may have significant effect on the Li-ion (de)intercalation within the cathode materials, as the crystal direction determines the route for Li-ion insertion and extraction within the tunneled lattice structure (Fig. 4.4), and the grain boundaries provide fast diffusion paths.

Similarly, a $Li[Ni_{1/3}Co_{1/3}Mn_{1/3}]O_2$ (L333) primary particle was examined by SEM as shown in Fig. 4.5. The particle forms a rough spherical shape consisting of a few hundred rod-shaped crystalline grains of sub-micron size. High-resolution SEM images in Fig. 4.6 show more details of the crystalline formation and grain boundaries; individual grains have distinctive crystal surface structures, randomly oriented and facing one another, which create very complicated grain boundaries with a large area. Although

(a)

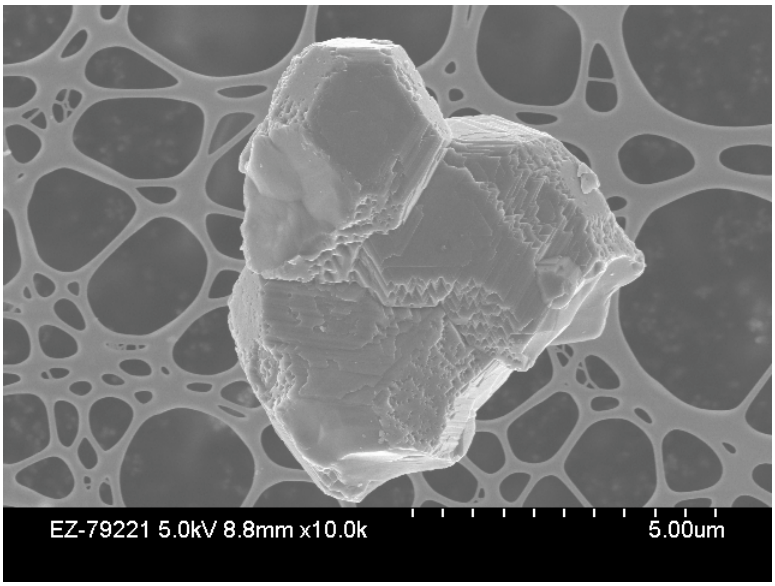

(b)

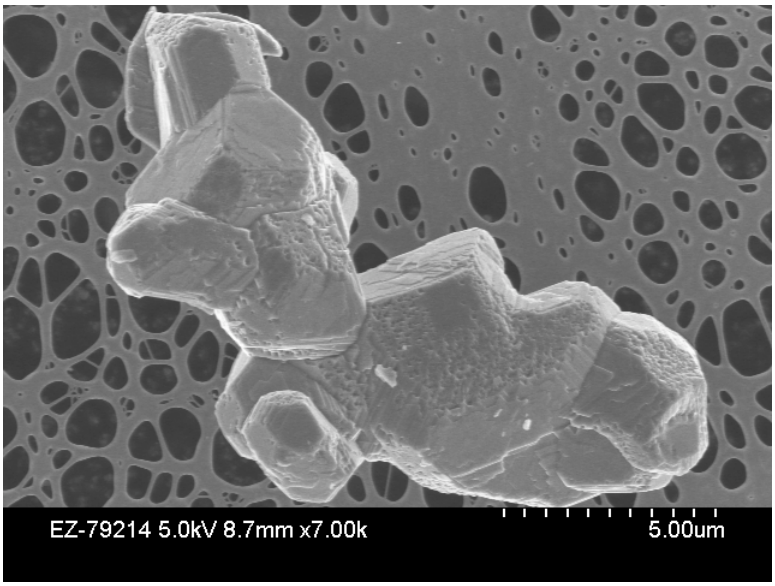

Figure 4.2: SEM images of $LiMn_2O_4$ spinel: (a) particle with spherical/ellipsoidal appearance (b) particle with irregular structure

(a)

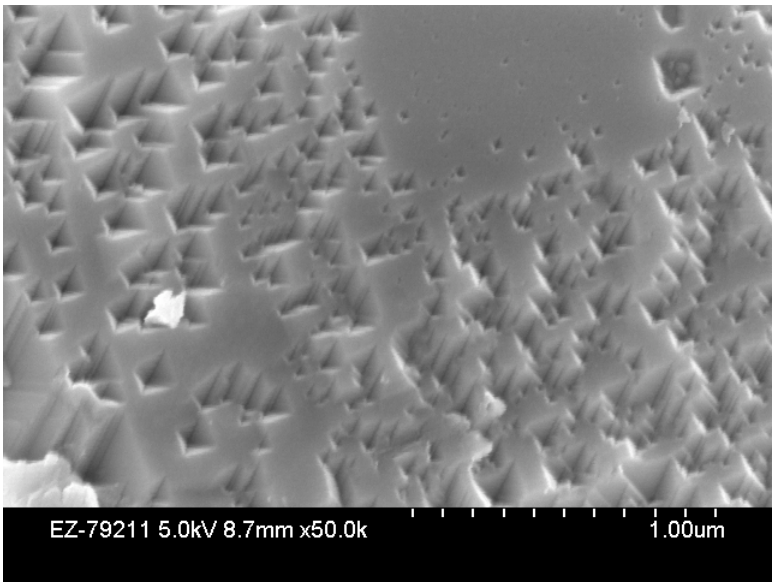

(b)

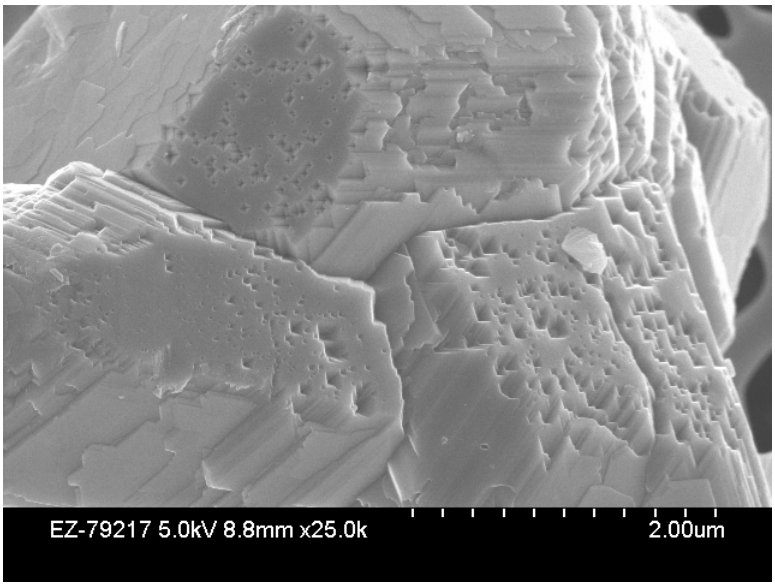

Figure 4.3: High resolution SEM images of $LiMn_2O_4$ crystal grains: (a) crystal grain surface, (b) grain boundaries

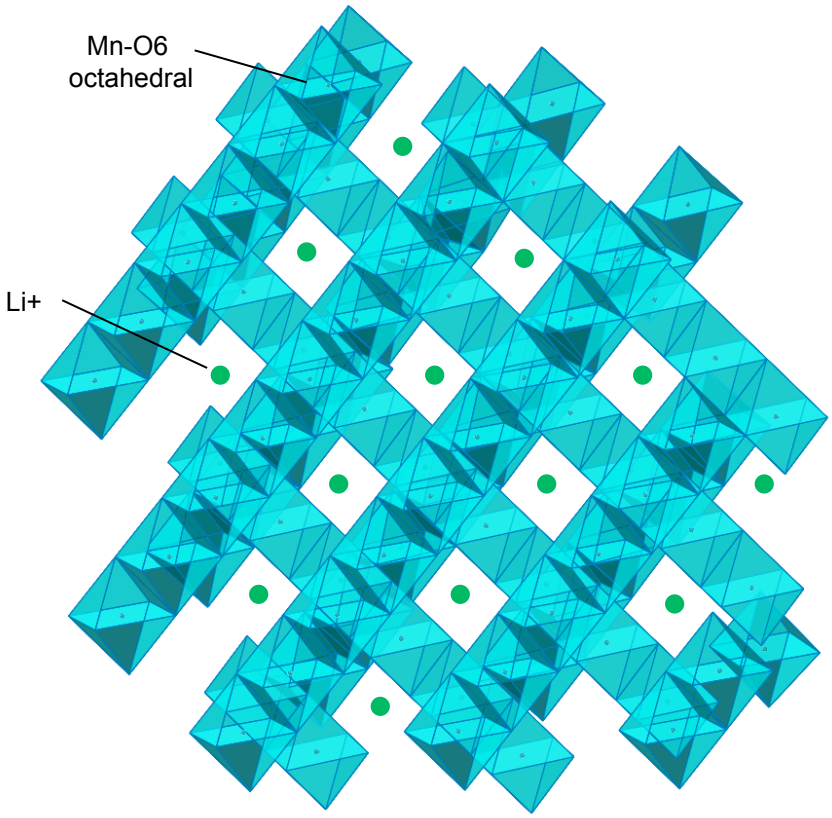

Figure 4.4: Schematic lattice structure of $LiMn_2O_4$ spinel

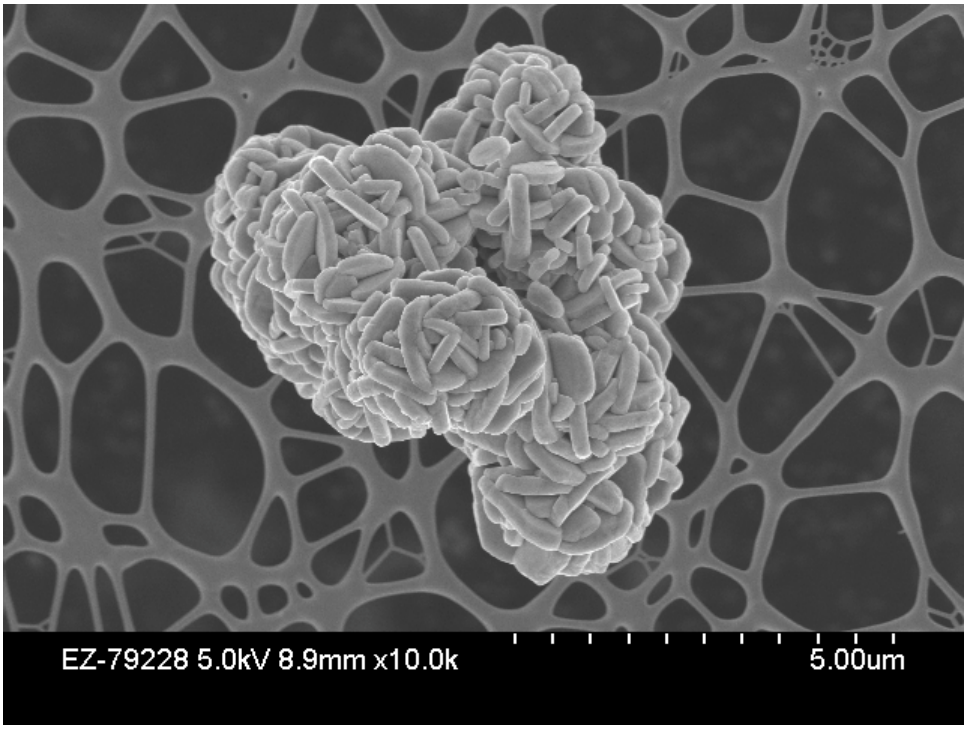

Figure 4.5: SEM images of $Li[Ni_{1/3}Co_{1/3}Mn_{1/3}]O_2$ primary particles

(a)

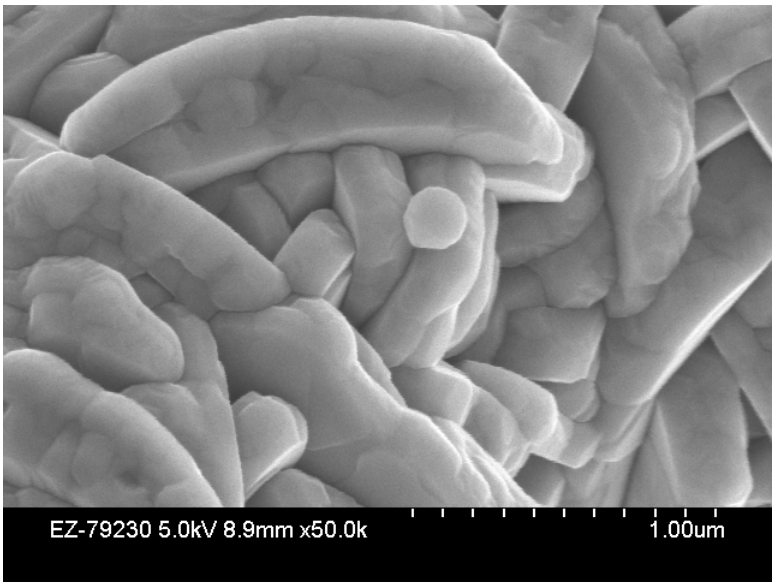

(b)

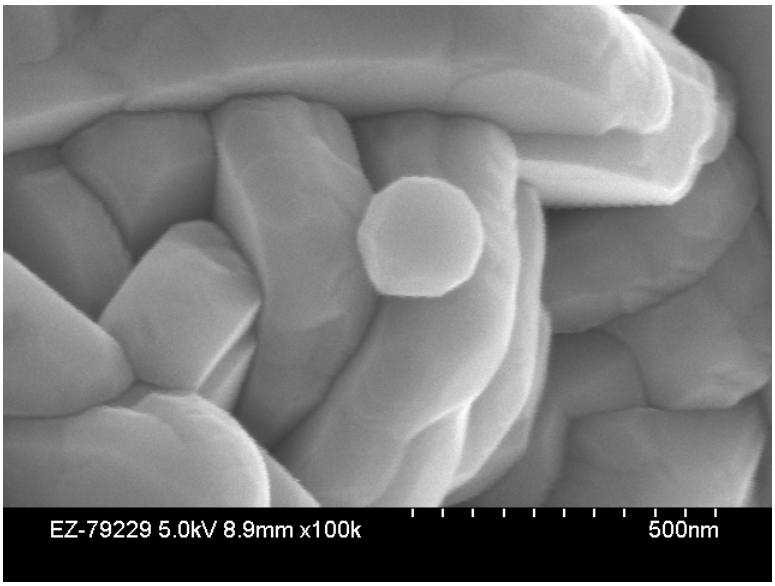

Figure 4.6: High resolution SEM: (a) primary particle, (b) close view of crystalline grains and boundaries

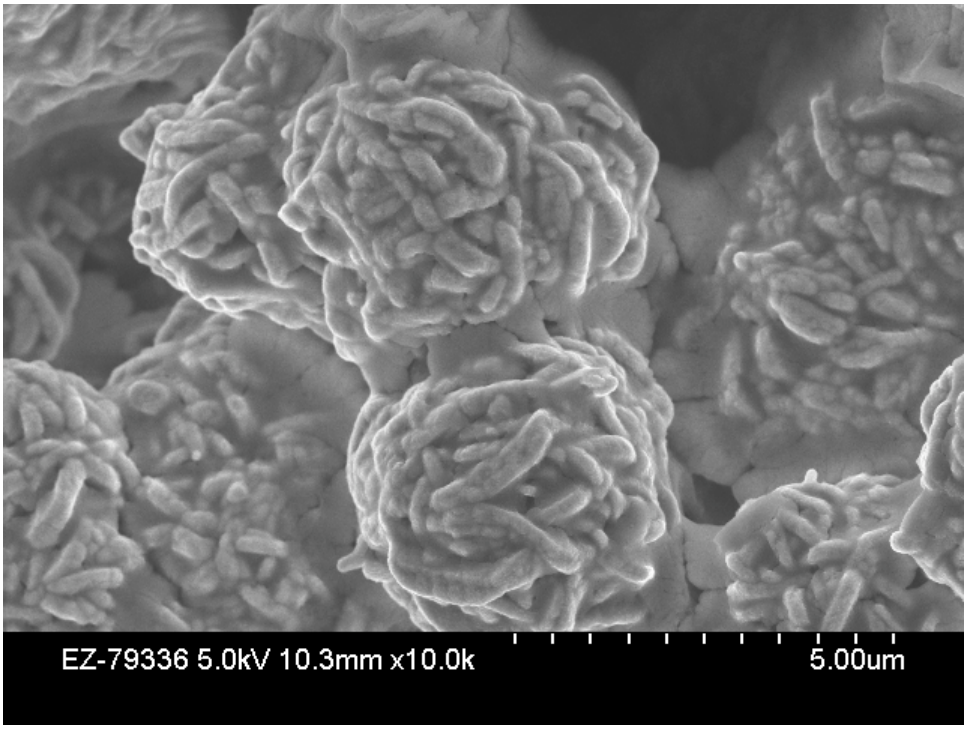

Figure 4.7: SEM images of composite L333 electrode mixed with additives

(a)

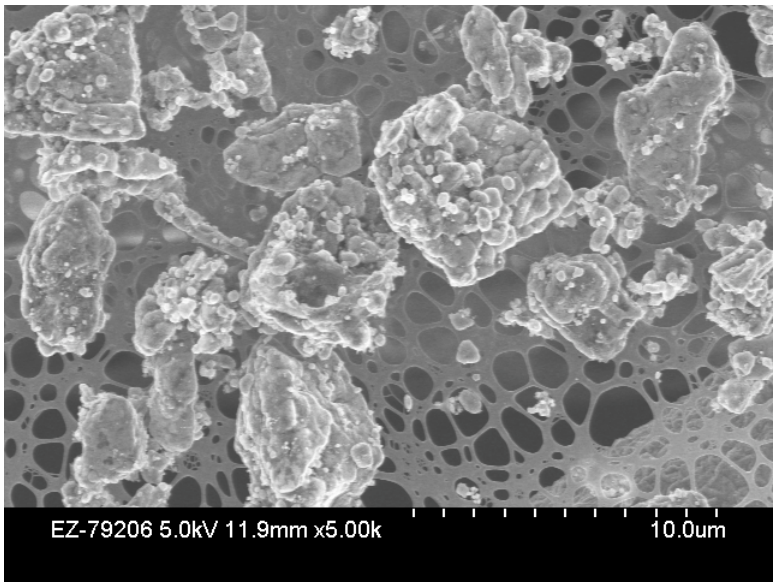

(b)

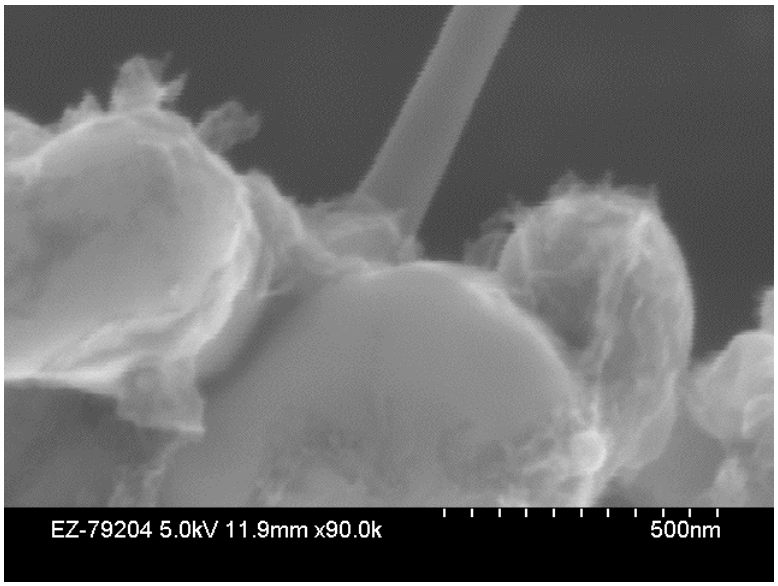

Figure 4.8: SEM images of $LiFePO_4$ particles: (a) primary particles, (b) carbon coating on particles

the local diffusion within a crystal grain and its boundary is affected by the crystalline direction, and thus anisotropic, the global diffusion within a particle does not have a particular direction and thus can be assumed isotropic. Another observation from L333 particle SEM is that the materials have an advantage of hosting more conductive additives due to the complex and large particle surface as shown in Fig. 4.7. SEM images of $LiFePO_4$ in Fig. 4.8 show irregular size and shape of secondary particles consisting of relatively uniform size primary particles (0.3~0.5 μm) of either spherical or ellipsoidal shape. Crystal grains within the primary particles were not recognizable by SEM, instead they were observed by TEM. $LiFePO_4$ powder included carbon coating shown as fluffy thin layer on the primary particles.

TRANSMISSION ELECTRON MICROSCOPY (TEM)

$LiMn_2O_4$ spinel particles were also studied by TEM for the multi-crystalline internal structure; Figure 4.9(a) shows a primary particle consisting of a few crystal grains. The particle has a distinctive spinel crystal layout, and the internal region shows various levels of gradation depending on the number of overlapping crystal grains. High-resolution TEM in Fig. 4.9(b) shows a $LiMn_2O_4$ lattice structure with uniformly spaced striae indicating a single crystal grain. The interplanar distance of this grain is measured as approximately 0.48 nm, which is similar to the interplanar distance of (111) plane, 0.476 nm, calculated from $LiMn_2O_4$ powder XRD patterns. This indicates (111) planes are vertical to the crystalline grain surface. TEM image of $LiMn_2O_4$ polycrystalline in Fig. 4.10 contains multiple regions of lattice layers with different interplanar distances

and directions, indicating there are a number of crystalline grains packed in this particle. The internal grain boundaries are identified from this image following the lattice patterns.

TEM on $LiFePO_4$ particles revealed their internal structures; each primary particle in Fig. 4.11(a) shows spotted regions of crystal grains. The crystalline lattice structure of $LiFePO_4$ can be identified by several layers in high-resolution TEM with the interplanar distance measured as 0.45 nm (Fig. 4.11(b)), similar to the c-axis lattice parameter, 0.463 nm measured from previous XRD studies [5, 6]. The grain boundaries inside particles that were not observed by SEM, are defined by the lattice patterns in this TEM image.

Cathode particle observation from SEM and TEM leads us to a different point of view on the orientation dependence of Li-ion diffusion kinetics that has been studied in several lithium metal oxide thin films [7, 8, 9]. Cathode materials with layered structure, such as $LiCoO_2$ and $LiNi_{0.8}Co_{0.2}O_2$, showed that their diffusion properties and electrochemical behaviors are highly dependent on the lattice orientation; a certain lattice direction provides a speedy path for Li-ion movement, while some other directions block ionic diffusion and thus result in poor high-rate electrochemical performance. Three-dimensional tunneled structures of $LiMn_2O_4$ spinel, or $LiFePO_4$ olivine have shown better performance as the Li-ions can be released from any crystal orientation. In fact, the 3D framework structure in $LiMn_2O_4$, or $LiFePO_4$ is the main reason for their excellent high-rate performance that is required for candidate materials to power electric vehicles. However, when we consider micro- or particle-scale diffusion, intergranular diffusion, or diffusion through the grain boundaries gets deeply involved in the Li-ions intercalation process at the single particle level. To know the exact properties of metal oxide Li-ion insertion materials and predict long-term cell behaviors and failure, we should understand

(a)

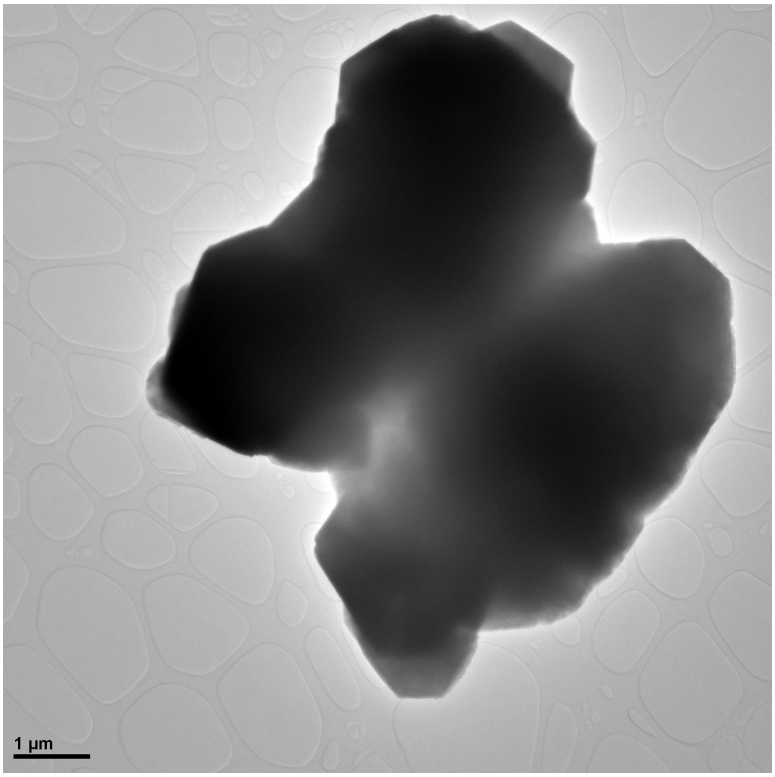

(b)

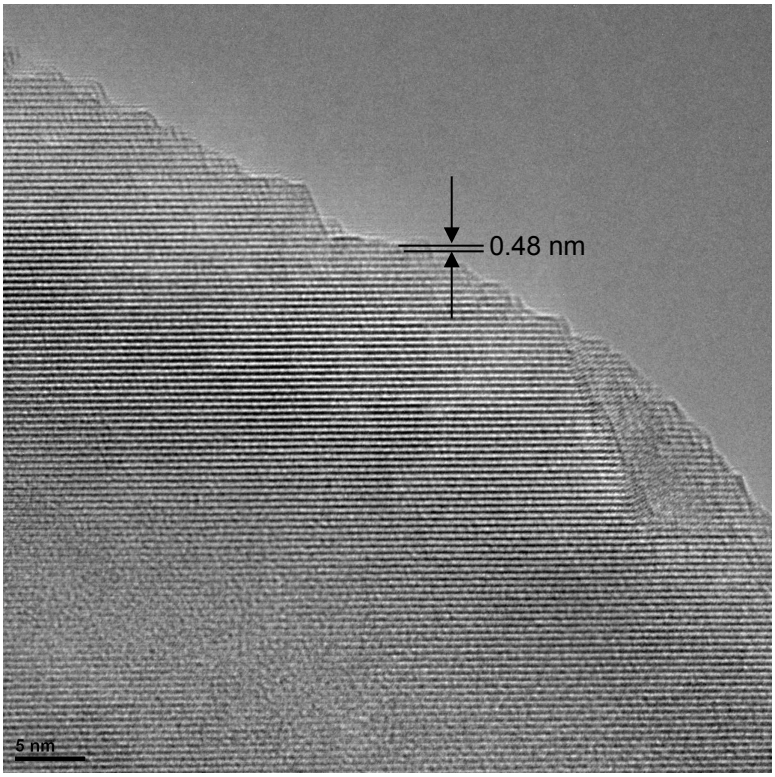

Figure 4.9: TEM images of $LiMn_2O_4$ spinel: (a) single particle, (b) lattice structure depicted by striae

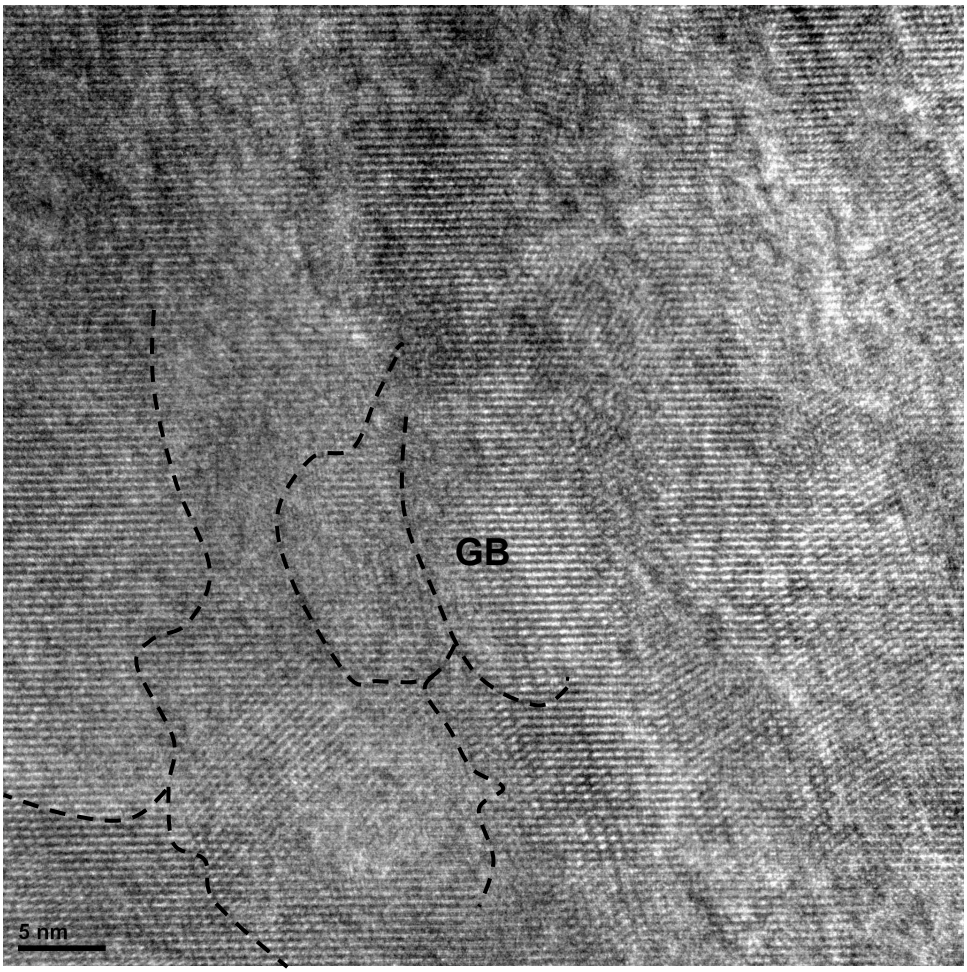

Figure 4.10: Internal grains and boundaries from a $LiMn_2O_4$ particle

(a)

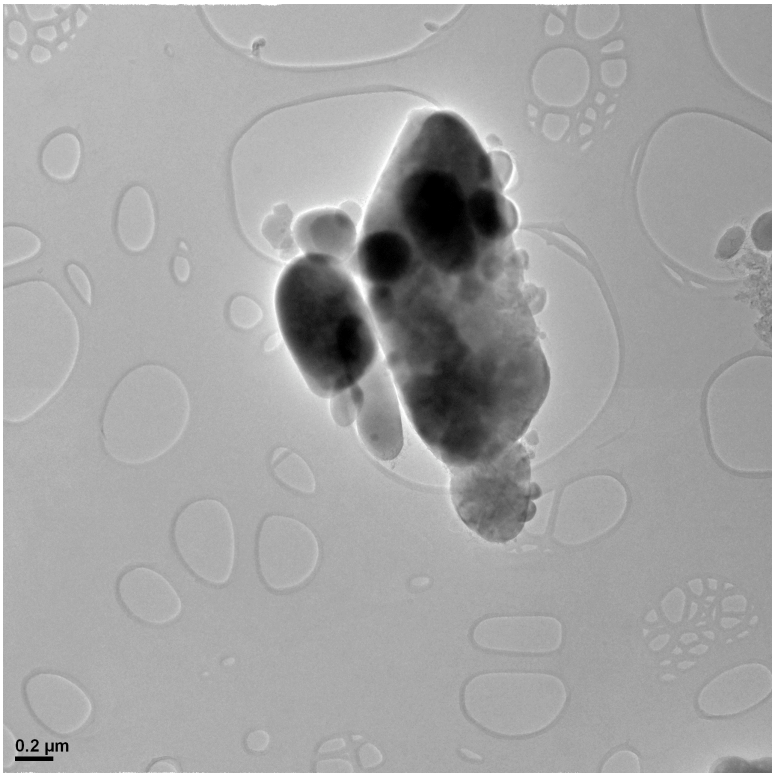

(b)

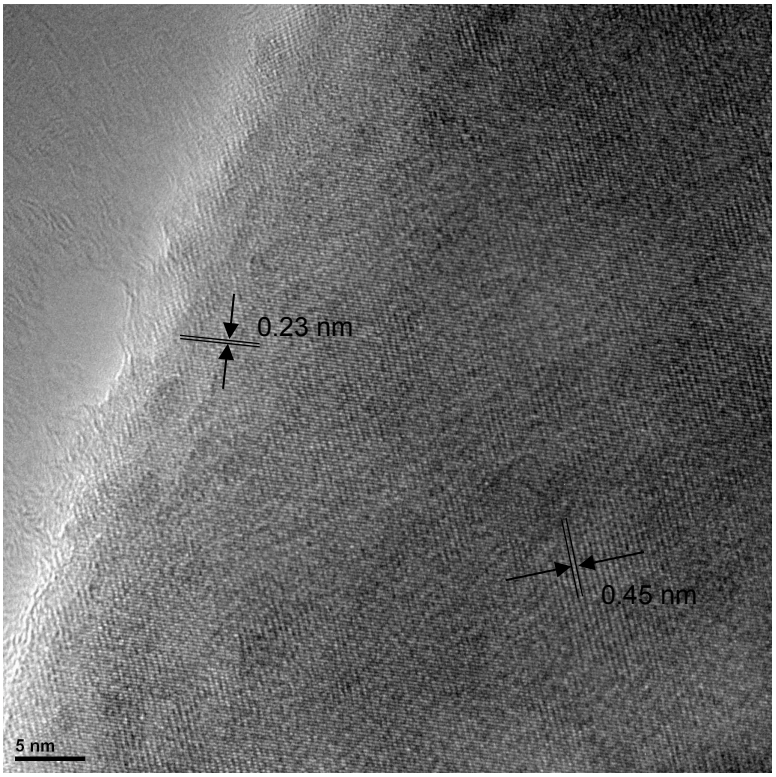

Figure 4.11: TEM images of $LiFePO_4$ olivine particle: (a) primary particles consisting of 200-400 nm size crystal grains, (b) lattice structure

and eventually characterize their anisotropic and inhomogeneous aspects originated from the sub-particle structures of crystal grain and grain boundaries.

X-RAY DIFFRACTOMETRY (XRD)

X-ray samples were extracted from $Li_xMn_2O_4/LiPF_6$ in EC:DEC/Li cells cycled under 20 μA (C/40) constant current charging or discharging to 4.40, 3.99, 3.30 (as-fabricated) as shown in Fig. 4.12. X-ray diffraction revealed different Li-content spinel compositions of $Li_{0.115}Mn_2O_4$, $Li_{0.4}Mn_2O_4$, and $LiMn_2O_4$, and corresponding lattice parameter change from c = 8.064 to 8.2402 for the cubic structure (Fig. 4.13). The intercalation-induced lattice expansion of full range, from λ-Mn_2O_4 (at fully charged state) to $LiMn_2O_4$ (at fully discharge state), has been measured in parametric change between c = 8.026 and 8.240, 7.6% expansion of cubic crystal structure [10]. Our calculation of 6.7% lattice expansion between x = 0.115 and 1 shows good agreement with the literature. XRD calculated a lattice spacing of d_{111} = 0.476 nm from as-fabricated $LiMn_2O_4$. This provides good comparison to the interplanar distance of 0.48 nm measured from TEM image.

ATOMIC FORCE MICROSCOPY (AFM)

Crystal grains and their boundaries were measured from isolated $LiMn_2O_4$ single particles by surface scanning with AFM. Fig. 4.14 shows three-dimensional morphology of a primary $LiMn_2O_4$ particle consisting of several crystalline grains with grain boundaries clearly illustrated on the particle surface. The AFM result proves that the 3D scanning technique can be a useful tool to study cathode powder materials for their

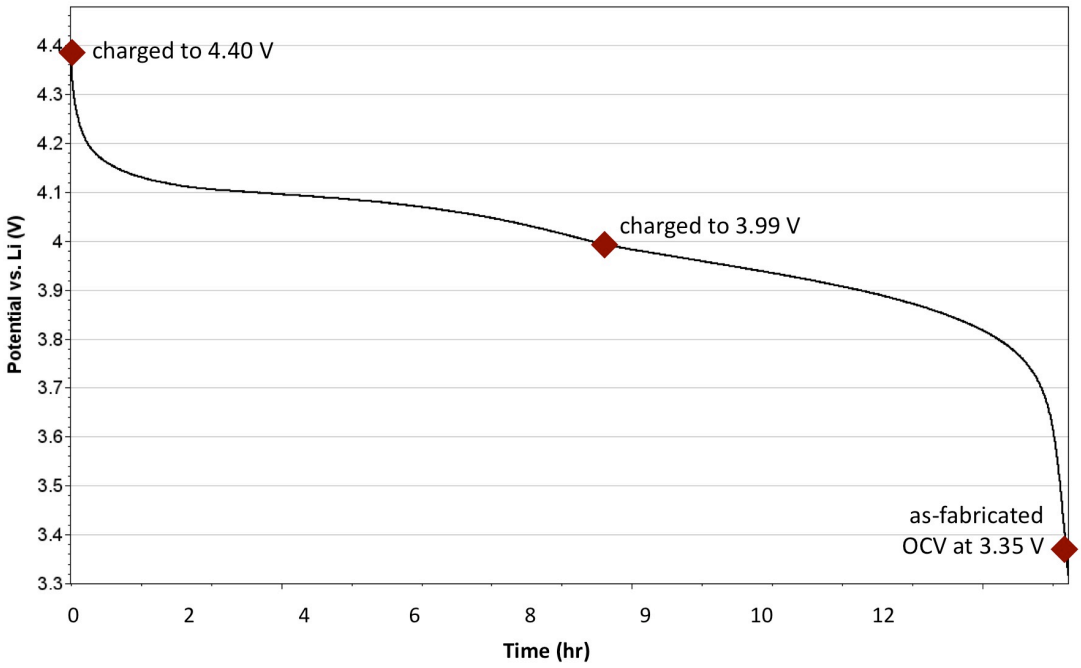

Figure 4.12: Electrochemical behavior of a $LiMn_2O_4$ composite cell under Galvanostatic cycling (SOC states for XRD are marked)

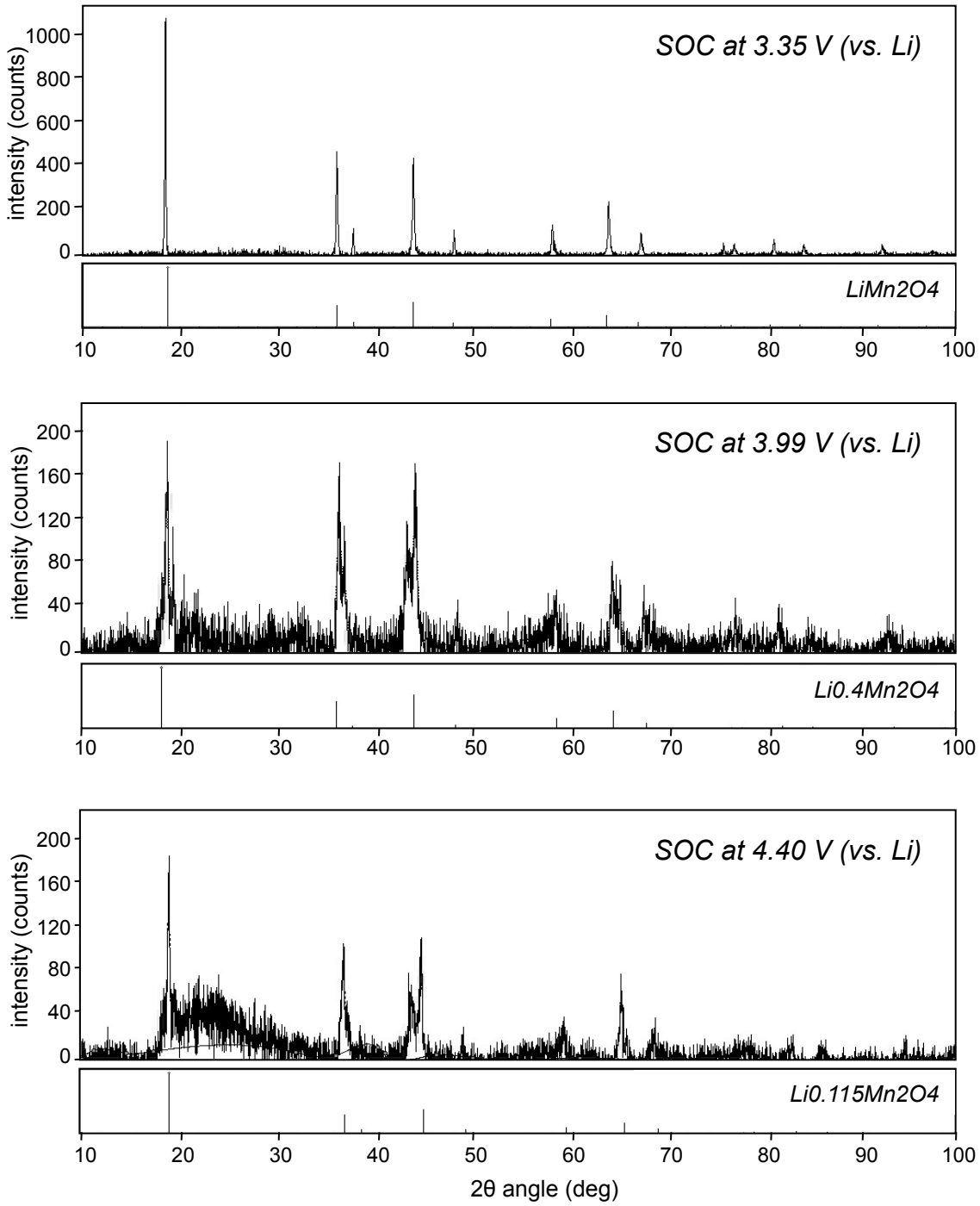

Figure 4.13: XRD intensity plot with different diffraction patterns

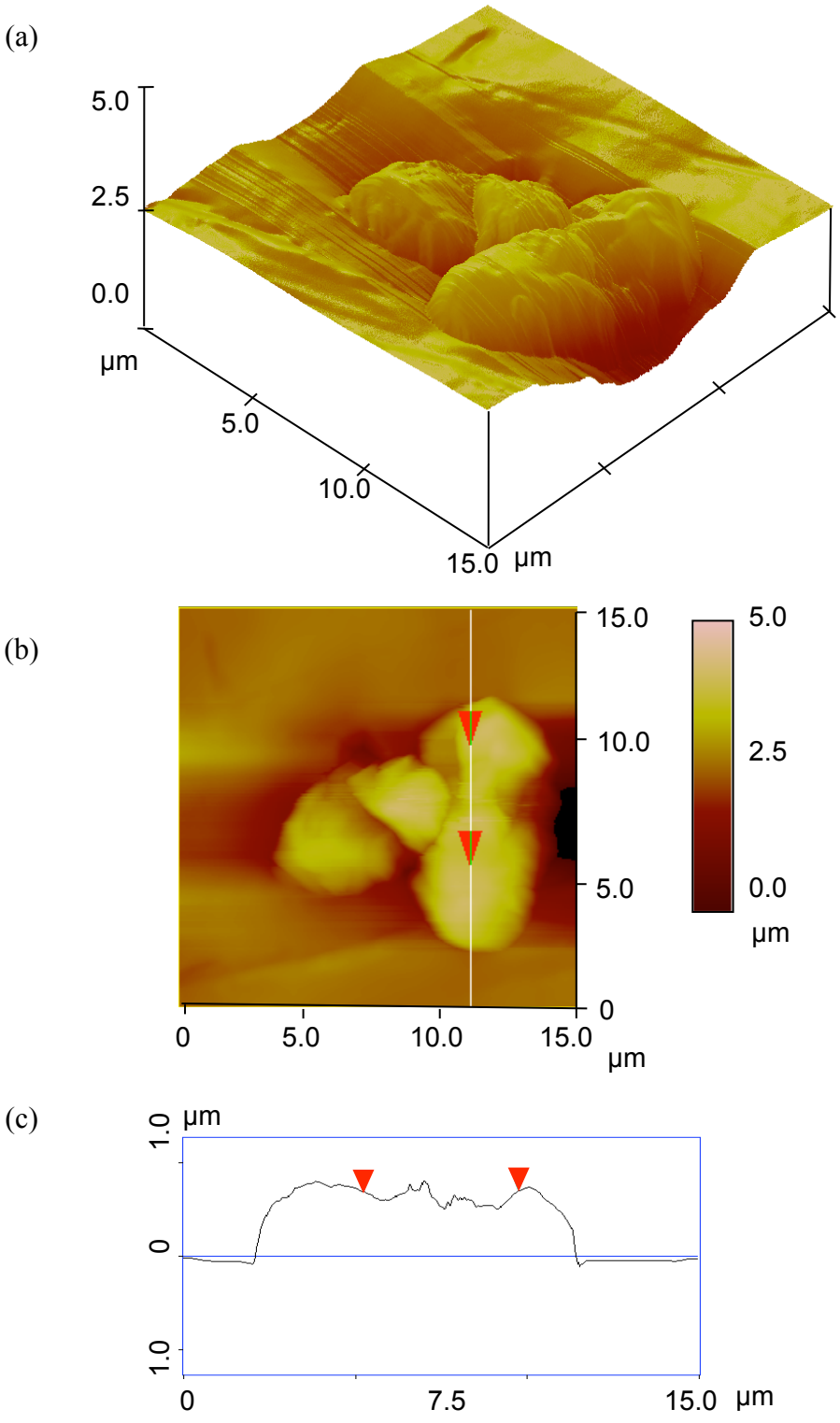

Figure 4.14: AFM images of single particles by tapping mode on a scan size of 15 × 15 μm: (a) 3D image, (b) 2D profile of surface height, and (c) sectional analysis on a cross section line indicated by red arrows

geometry surface microstructure. In a later chapter, AFM will also be used to reconstruct a cathode single particle to provide realistic geometry for electrode modeling.

CONCLUSIONS AND FUTURE WORK

A number of metal oxide Li-ion insertion compounds materials were proposed for future electric vehicle batteries. Among those materials, $LiMn_2O_4$, $Li[Ni_{1/3}Co_{1/3}Mn_{1/3}]O_2$, and $LiFePO_4$ are the most promising and the most studied candidate materials, and thus were chosen for our materials characterization study. Various characterization techniques including SEM, TEM, XRD, and AFM were used to observe external and internal microscopic morphology of primary/secondary particles, to analyze the lattice structure of chemical compositions, and to obtain three-dimensional morphological information from the materials' surface. The resultant images and data showed that the cathode particles are anisotropic and inhomogeneous due to the hierarchic structure consisting of crystal grains and grain boundaries. The highly directed small number of crystalline grains in $LiMn_2O_4$ spinel make the material more anisotropic, while the complex and packed crystals in a $Li[Ni_{1/3}Co_{1/3}Mn_{1/3}]O_2$ particle increase its isotropic nature. XRD was used to measure $Li_xMn_2O_4$ spinel lattice expansion when Li-ions intercalate from $x = 0$ to 1, as a preliminary step in investigating the morphological change during $LiMn_2O_4$/Li cell cycling. Surface profiles from AFM showed the detailed three-dimensional structure of crystalline grains and boundaries of $LiMn_2O_4$ particles. Anisotropic and inhomogeneous aspects of cathode particles should be a subject of future study in modeling and control of Li-ion batteries; they will significantly affect the electrochemical

reactions and mechanical behaviors and they may have dominant effects on particle fracture and eventual failure. In situ measurement with XRD and AFM also should follow to accurately assess the structural changes related to the Li-ion intercalation processes.

BIBLIOGRAPHY

1. D. Linden, and T.B. Reddy, Handbook of batteries, 3rd Ed., McGraw-Hill (2002)

2. K. Mizushima, P.C. Jones, P.J. Wiseman, and J.B. Goodenough, Li_xCoO_2 ($0<x<1$): A new cathode material for batteries of high energy density, Materials Research Bulletin 15, 783-789 (1980)

3. W. Ebner, D. Fouchard, and L. Xie, The $LiNiO_2$/carbon lithium-ion battery, Solid State Ionics 69, 248-256 (1994)

4. M.-H. Lee, Y.-J. Kang, S.-T. Myung, and Y.-K. Sun, Synthetic optimization of $Li[Ni_{1/3}Co_{1/3}Mn_{1/3}]O_2$ via co-precipitation, Electrochimica Acta 50, 939-948 (2004)

5. A.K. Padhi, K.S. Nanjundaswamy, and J.B. Goodenough, Phospho-olivines as positive-electrode materials for rechargeable lithium batteries, Journal of The Electrochemical Society 144 (4), 1188-1194 (1997)

6. C.H. Mi, X.G. Zhang, X.B. Zhao, and H.L. Li, Effect of sintering time on the physical and electrochemical properties of $LiFePO_4$/C composite cathodes, Journal of Alloys and Compounds 424 (1-2), 327-333 (2006)

7. J.B. Bates, N.J. Dudney, B.J. Neudecker, et al., Preferred orientation of polycrystalline $LiCoO_2$ films, Journal of The Electrochemical Society 147 (1), 59-70 (2000)

8. J. Xie, N. Imanishi, T. Matsumura, et al., Orientation dependence of Li-ion diffusion kinetics in $LiCoO_2$ thin films prepared by RF magnetron sputtering, Solid State Ionics 179, 362-370 (2008)

9. T. Matsumura, N. Imanishi, A. Hirano, N. Sonoyama, and Y. Takeda, Electrochemical performances for preferred oriented PLD thin-film electrodes of $LiNi_{0.8}Co_{0.2}O_2$, $LiFePO_4$ and $LiMn_2O_4$, Solid State Ionics 179, 2011-2015 (2008)

10. M.M. Thackeray, Manganese oxides for lithium batteries, Progress in Solid State Chemistry 25, 1-71 (1997)

CHAPTER V

EXPERIMENTAL STUDY WITH THIN FILM CATHODE MATERIALS OF LI-ION BATTERIES[1]

INTRODUCTION

Conventionally Li-ion battery electrodes are made by mixing active materials in particle forms (1-10 μm size) with conductive additives and organic binder, and by compressing the composite material to achieve desired volume fraction. When this type of composite electrode is used for electrochemical measurement, the additive materials interfere with accurate assessment of the energetically active materials' properties. There have been a number of studies to develop experimental models free from the parasitic effects of battery additives, including thin film electrodes (Table 1.8), single particle electrodes (Table 1.9), and a dispersed single particle model that was discussed earlier in chapter 3. In this chapter, we will discuss lithium manganese oxide thin film, from its fabrication to structural and electrochemical characterization.

Thin film type electrodes have been widely used for many experimental studies of Li-ion battery materials research as they can provide a simple, quite dense, and uniform layer model for the study of Li-ion intercalation. Radio-frequency (RF) magnetron

[1] Material in this chapter was presented as: M.D. Chung, X. Zhang, M. Park, and A.M. Sastry, Experimental Study of Diffusion Properties of Spinel $LiMn_2O_4$ Thin Film Electrodes and Their Characterization with In-situ Atomic Force Microscopy, *215th ECS Meeting*, San Francisco, CA, May 24 (2009)

sputtering is one of well-established techniques to deposit cathode films (Table 5.1), and was used in this study [1, 2, 3, 4, 5, 6, 7]. $LiMn_2O_4$ has been targeted for this thin film study due to its promising features as a mass-produced battery material, such as high voltage, low cost, and low toxicity. Earlier studies with different metal oxide cathodes, especially $LiCoO_2$, showed the importance of deposition and post-annealing conditions, such as substrate materials and bias voltages, film thicknesses, annealing temperature and duration [1, 2, 3]; however, there has been no study of $LiMn_2O_4$ thin films linking the fabrication conditions to their structural characteristics.

Our research aims to study lithium manganese oxide films with various thicknesses (0.3-2.3 μm) made by RF-sputtering on two different types of substrates (gold-coated silicon / stainless steel), using a single $LiMn_2O_4$ target. Post-annealing conditions including temperature (550-750°C), heating and cooling rate (5-15°C/min), and atmospheric setup will also be investigated for their structural and electrochemical characteristics. Specific objectives in this study are as follows:

1. To fabricate lithium manganese oxide cathode thin films using RF magnetron sputtering and post-annealing processes.
2. To characterize the film structure and morphology using XRD and SEM to investigate how different fabrication conditions (e.g. substrates and annealing temperature) affect the film structure and morphology.
3. To electrochemically test the cathode thin film to investigate how its structural characteristics affect its electrochemical properties.

Cathode material	Electrolyte / anode	Thickness (µm)	Capacity (µAh/cm^2 µm)	Focus / findings
$LiCoO_2$	Lipon / Li	0.05-1.8	68	preferred lattice orientation of polycrystalline with various thicknesses
	Lipon / Li	1.2	60	effect of substrate bias on electrochemical properties
	PEO polymer / Li	0.3-1.4	66	orientation dependence of Li-ion diffusion coefficients
$LiMn_2O_4$	Lipon / Li	0.3	48	serial connection of solid-state microbatteries (32V)
	Lipon / Li	0.3	32	all solid-state thin film, process conditioning
	1M $LiClO_4$ in PC:DMC / Li	0.2	50	process conditioning including annealing temperatures (700-800°C)
V_2O_5	1M $LiClO_4$ in PC / Li	0.6-3.6	36	thickness-dependent orientation and its effect on Li-ion kinetics and crystal morphology

Table 5.1: Thin film studies using sputtering deposition [1-7]

METHODS

THIN FILM FABRICATION

Lithium manganese oxide thin films were deposited on both gold-coated silicon substrates and stainless steel substrates using RF magnetron sputtering with a system configuration as shown in Fig. 5.1. The sputtering target was prepared by sintering $LiMn_2O_4$ powder (99.5% battery grade, Aldrich) at 650°C for 24 hrs to form 2-inch diameter ¼-inch thick targets. Substrates were obtained from a gold/titanium-coated silicon wafer (Aldrich) by cutting it into 0.5-by-0.5 inches size substrates, or punching ½-inch diameter discs from 100 μm stainless steel sheet. The 500 μm thick substrates contained a Ti-adhesion layer used to bind the gold layer to form a current collecting layer of 1000 Å thickness, which also served as a barrier to prevent Si diffusion. The sputtering of $LiMn_2O_4$ thin films was made for three different thicknesses of 0.3, 0.9, and 2.6 mm, which were measured after deposition by using electron microscopy. Pre-sputtering was applied to eliminate any impurities from the target. After deposition, the amorphous cathode layer was annealed to recrystallize at 550 and 750 °C for 120 min with 5-15 °C/min heating and cooling rates.

THIN FILM CHARACTERIZATION

The film structure was characterized by X-ray diffraction (XRD), and film morphology was examined with scanning electron microscopy (SEM). XRD using a X'Pert Pro diffractometer (PANalytical) with Cu-Kα radiation was used to identify changes made between substrates and deposited films, and between as-deposited and annealed films. SEM (S-4800, Hitachi) was first used to measure the actual film

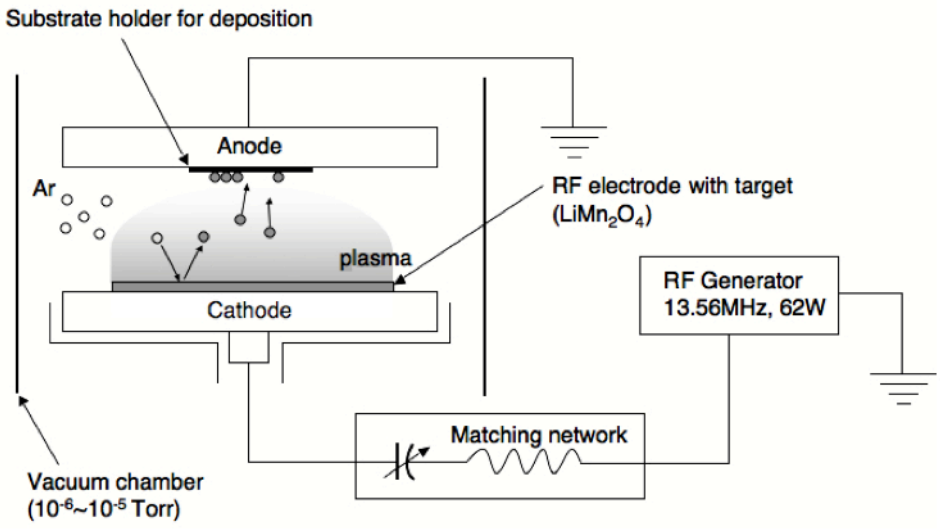

Figure 5.1: Schematic diagram of RF magnetron sputtering system

thickness from a sectional area, and also was used to assess the crystallized film conditions, including crystalline grain size. For electro-chemical studies, the film-coated substrates were assembled inside a glove box to Swagelok-type cells together with lithium metal anode and 1M $LiPF_6$ in a mixture (1:1 in volume) of ethylene carbonate (EC)/diethylene carbonate (DEC) as the liquid electrolyte. Galvanostatic cycling of the cells was carried out at a current density of 20 μA cm^{-2} between 2.5 and 3.3 V using a Bio-Logic VMP3 cell cycler.

RESULTS AND DISCUSSION

THIN FILM CHARACTERIZATION

The as-deposited films are amorphous layers of sputtered elements, such as lithium, manganese, and oxygen, with thicknesses controlled by changing the deposition time under a constant rate (~30 Å/min). SEM images were used to verify the film thickness as shown in Fig. 5.2. A silicon substrate and metal conduction/adhesion layers were also identified in backscattered electron (BSE) model images. After annealing, recrystallized cathode films observed by SEM showed well-defined crystalline grains with different sizes depending on the annealing temperature (Fig. 5.3). Higher annealing temperature at 750°C led to mostly larger grains sized up to 1 μm mixed with much smaller crystals, while lower temperature annealing at 550°C resulted in much smaller and uniform crystalline grains of 100 nm size. The temperature dependence of crystal formation has been studied in $LiCoO_2$ [8, 9] and $LiMn_2O_4$ thin films [6, 10, 11]. The

(a)

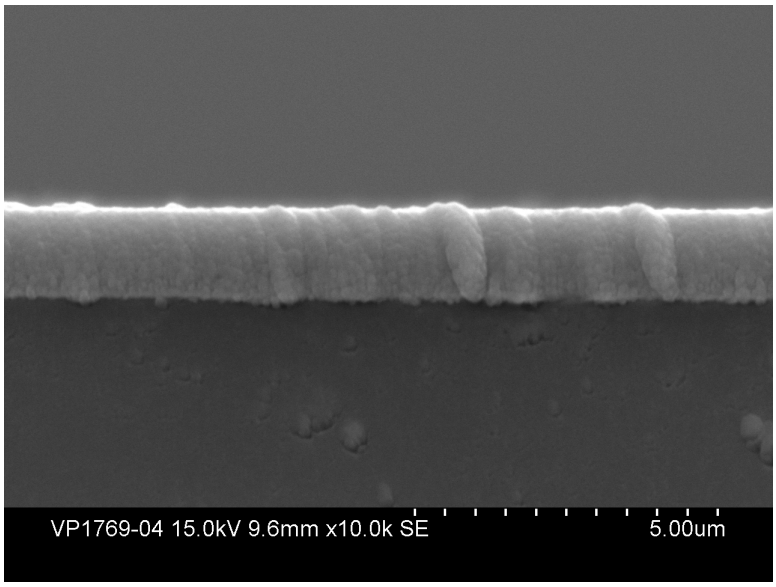

(b)

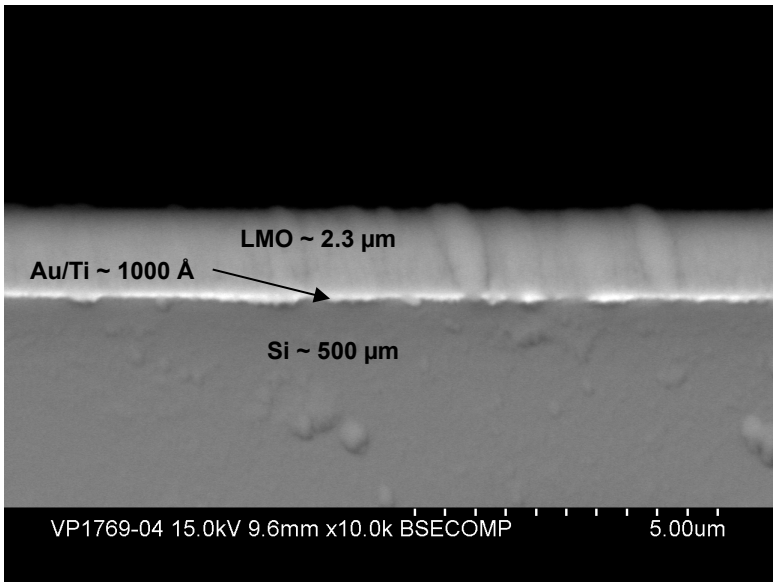

Figure 5.2: SEM of as-deposited thin films with (a) secondary electron (SE) mode (b) backscattered electron (BSE) mode showing cathode, metal-coating, and silicon substrate layers

(a)

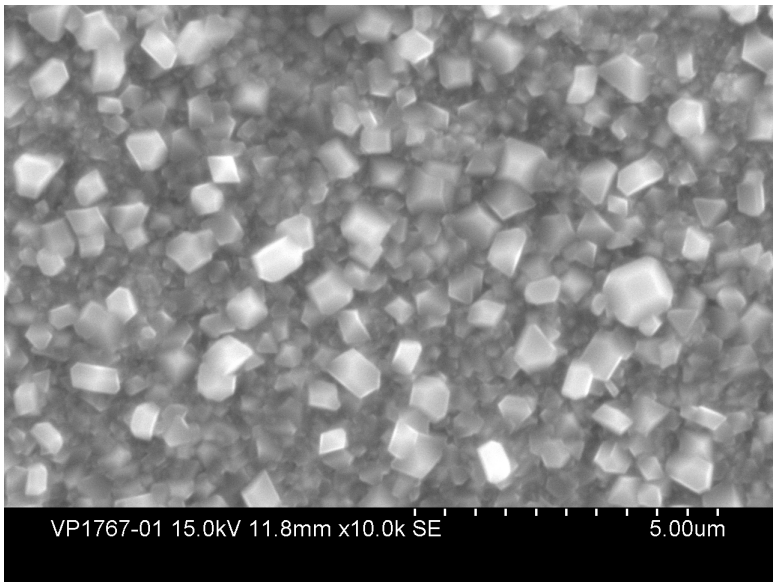

(b)

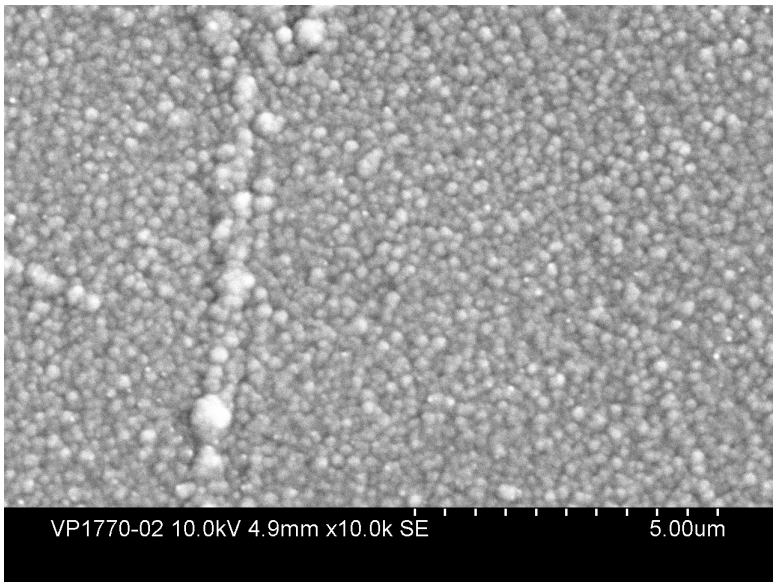

Figure 5.3: SEM of crystalline grains on thin films annealed for 120 min at (a) 750 ºC and (b) 550 ºC

observed pattern in this study was in good agreement with former studies on both silicon and stainless steel substrates.

XRD patterns for as-deposited and annealed films provide strong evidence of recrystallization processes, distinguished by the peaks for crystal lithium manganese oxides, such as Mn_2O_3 and $LiMn_2O_4$ (Fig 5.4 and Fig 5.5). Silicon substrate films show strong peaks for the substrate materials (Si and Au) before annealing, but after the annealed oxide material is detected the relative intensity of those materials decreases. For the stainless steel substrate films the opposite trend is observed: once the films are annealed, the peaks for Fe and Ni, base materials for the substrate, become stronger despite increased peaks from oxide crystals. This means (i) there are a significant amount of diffused Fe and Ni elements even in as-deposited films and (ii) the high temperature condition during annealing accelerates metal diffusion. With an inert coating layer also working as a barrier to prevent Si diffusion, gold-coated silicon substrates can be advantageous in protecting the cathode films' purity, at least when deposition techniques requiring post-annealing are used, including sputtering. Additionally, we should note that different substrates also affect the type of oxide crystals: a single phase of Mn_2O_3 was formed on silicon wafer substrate, while two phases of Mn_2O_3 and $LiMn_2O_4$ were mixed on annealed stainless steel films. No significant difference was found among different thickness samples from XRD patterns.

Some unexpected observations related to film fabrication conditions include film surface texture follows the rough substrate surface, and cracks form upon cooling after annealing. Figure 5.6 shows an amorphous film surface with patterns consisting of stripes and wrinkles. The films' rough surface inherited from the press-rolled stainless steel

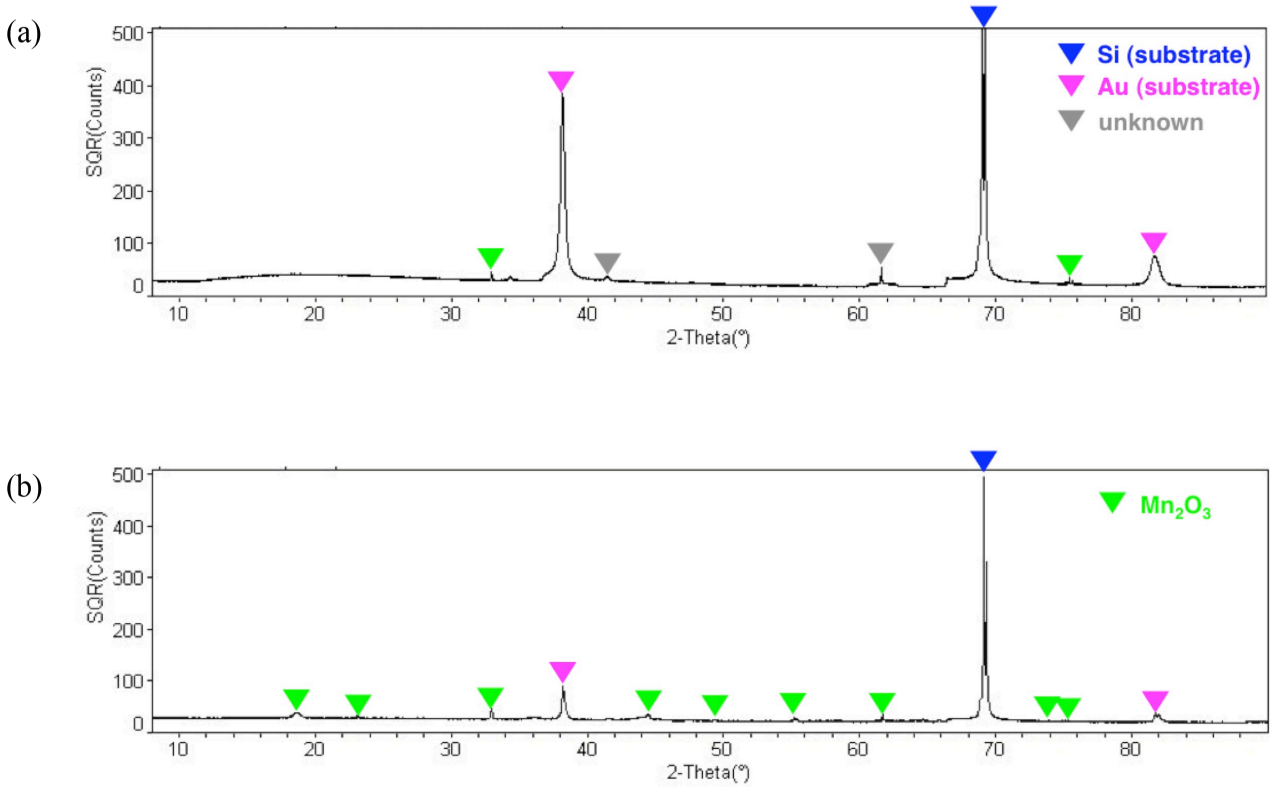

Figure 5.4: XRD patterns of thin films on gold-coated silicon substrates (a) as-deposited film and (b) annealed film with new peaks from recrystallization

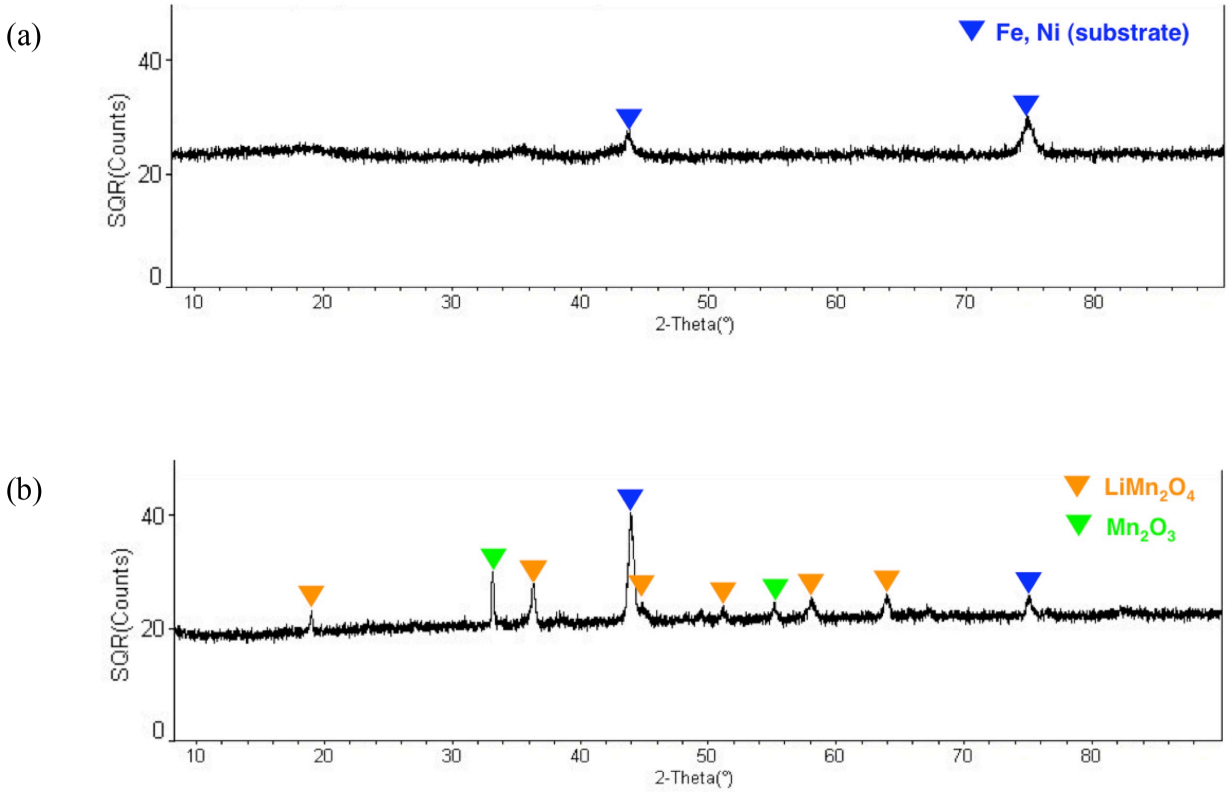

Figure 5.5: XRD patterns of thin films on stainless steel substrates (a) as-deposited film and (b) annealed film with new peaks from recrystallization

(a)

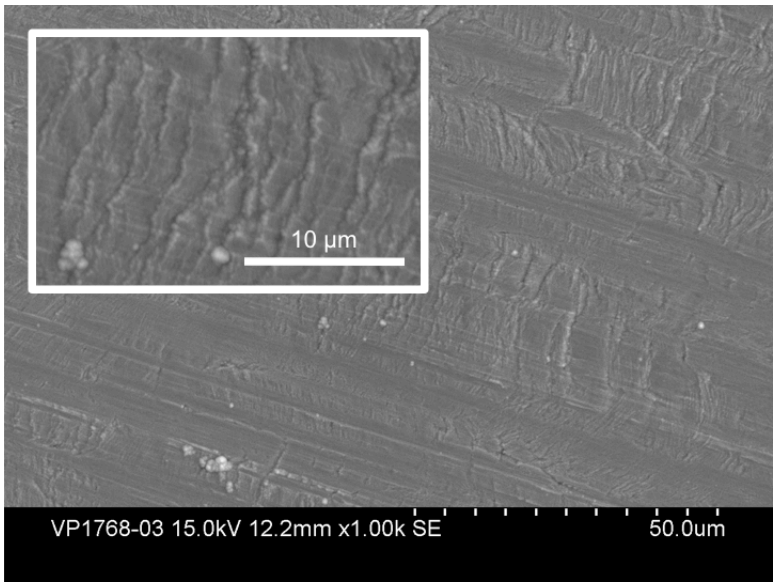

(b)

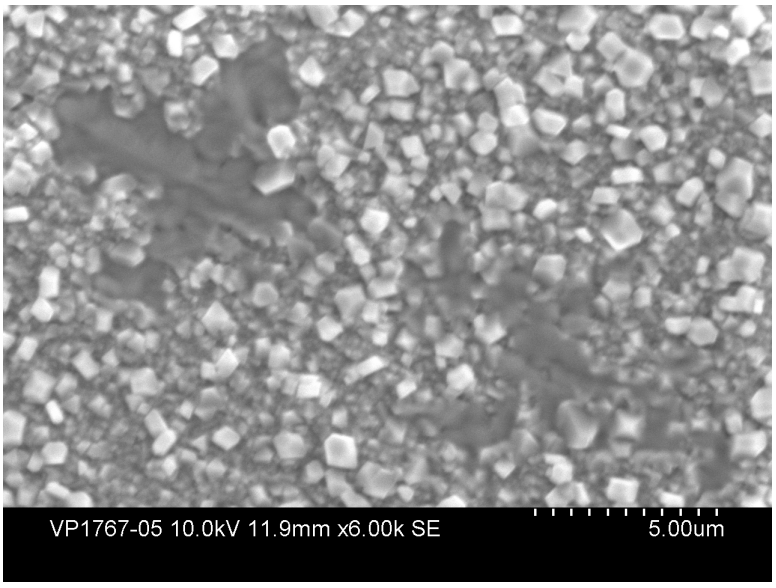

Figure 5.6: SEM images showing (a) a surface texture of amorphous as-deposited film with stripes and wrinkles (inlet), and (b) ruptured surface after annealing

substrates might have significant effects on the crystalline grain formation and its uniformity throughout the film surface. A number of ruptured spots as shown in Fig. 5.6(b) were observed from the oxide surface on stainless steel substrates. On gold-coated flat silicon substrates, extremely smooth amorphous oxide films were formed, which caused relatively weak adhesion between the deposited layer and its substrate. When as-deposited films were annealed and rapidly cooled down at 15°C/min, cracks formed on the oxide surface (Fig. 5.7). Closer view from a SEM image suggests complete separation of the cracked surface from its surrounding film and from the substrate. At lower cooling rates (5 and 10°C/min), however, no crack was observed.

ELECTROCHEMICAL BEHAVIOR

Galvanostatic cycling result of 0.9 μm thick film on a gold-coated silicon substrate is shown in Fig. 5.8 for the first 10 cycles. The first and the second charging cycles showed approximately full theoretical capacities of ~50 μA cm^{-2} μm^{-1}, but the capacity rapidly decreases down to 1/10 of the initial value from the third cycle, indicating the electrolyte decomposition has a dominant effect on the early cycles. Also, the potential plateaus in these cyclic curves differ from those of $LiMn_2O_4$ spinel material vs. Li-metal anode. As its XRD pattern indicates, the cathode film sputtered and annealed from $LiMn_2O_4$ target is mostly Mn_2O_3; the electrochemical measurement also supports this material identification, as discussed in the literature [12].

(a)

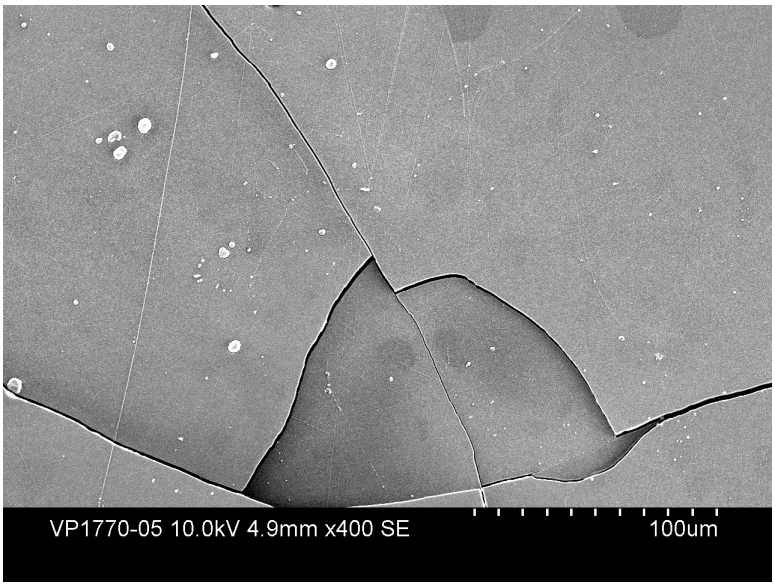

(b)

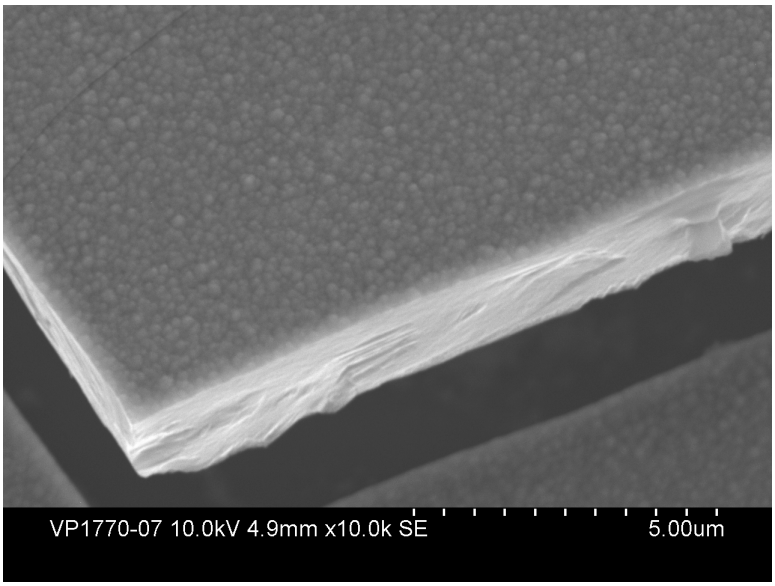

Figure 5.7: SEM images showing (a) a cracked surface after annealing, and (b) closer view to show separated films

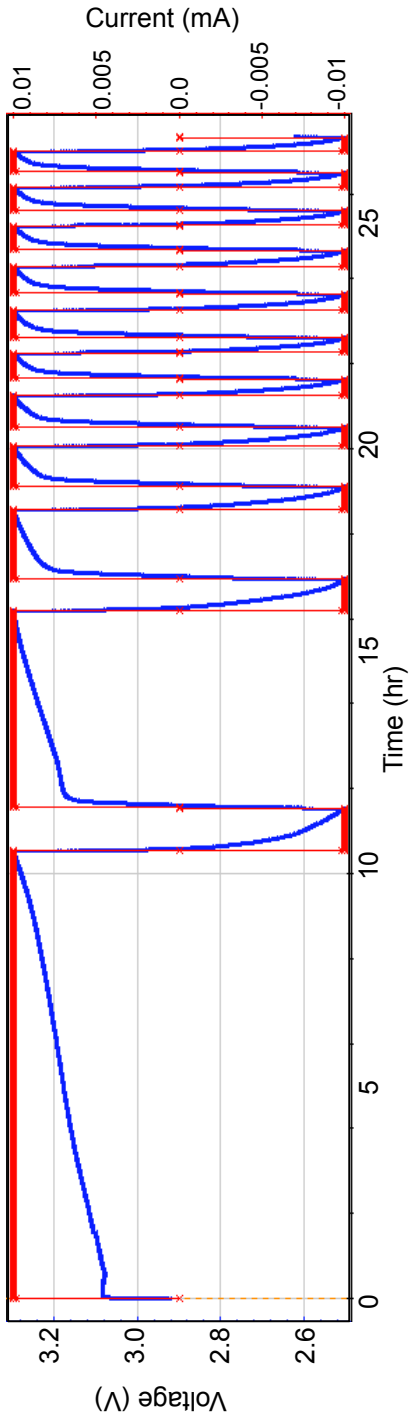

Figure 5.8: Galvanostatic cycling of lithium manganese oxide thin film vs. Li metal anode under 20 μA cm^{-2}

CONCLUSIONS AND FUTURE WORK

Lithium manganese oxide thin films were fabricated using RF magnetron sputtering deposition and post-annealing at temperatures 550° and 750°C. Various fabrication conditions, including substrate materials, film thickness, and annealing temperatures, were applied to investigate their influences on the structural characteristics of the films. Analyses based on SEM images and XRD patterns showed the annealing temperature has the most significant effect on the crystal formation by changing the grain size and its variation: at 550°C annealing, uniformly smaller crystal grains of 100 nm formed, while larger 0.5~1.5 μm size grains formed when annealed at 750°C. The types of substrate used also affected the films' characteristic and quality. Stainless steel substrates provide good adhesion to the oxide film, but the diffusion of their base metal elements might interfere with the film formation and alter its composition; gold-coating on silicon substrates serves as a barrier to protect the film's purity, although weakly attached oxide films on the flat substrate may crack upon fast cooling at 15°C/min. No structural change has been found in this study from lithium manganese oxide films with different thicknesses. Both XRD and electrochemical tests revealed the fabricated film materials were either Mn_2O_3 or a mixture of Mn_2O_3 and $LiMn_2O_4$. Structural characteristics of pure $LiMn_2O_4$ films might be different from what we found. Hence, to investigate how the structural characteristics of $LiMn_2O_4$ thin films are interrelated with their electrochemical and Li-ion kinetic properties, $LiMn_2O_4$ films should be fabricated either by modifying sputtering conditions, such as atmospheric pressure and target materials, or by using different deposition techniques, including pulsed laser deposition.

BIBLIOGRAPHY

1. J.B. Bates, N.J. Dudney, B.J. Neudecker, et al., Preferred orientation of polycrystalline $LiCoO_2$ films, Journal of The Electrochemical Society 147 (1), 59-70 (2000)

2. J. Xie, N. Imanishi, T. Matsumura, et al., Orientation dependence of Li-ion diffusion kinetics in $LiCoO_2$ thin films prepared by RF magnetron sputtering, Solid State Ionics 179, 362-370 (2008)

3. H.Y. Park, S.R. Lee, Y.J. Lee, et al., Bias sputtering and characterization of $LiCoO_2$ thin film cathodes for thin film microbattery, Materials Chemistry and Physics 93, 70-78 (2005)

4. Y.S. Park, S.H. Lee, B.I. Lee, and S.K. Joo, All-solid-state lithium thin-film rechargeable battery with lithium manganese oxide, Electrochemical and Solid-State Letters 2 (2), 58-59 (1999)

5. J.B. Bates, N.J. Dudney, D.C. Lubben, et al., Thin-film rechargeable lithium batteries, Journal of Power Sources 54, 58-62 (1995)

6. K.H. Hwang, S.H. Lee, and S.K. Joo, Characterization of sputter-deposited $LiMn_2O_4$ thin films for rechargeable microbatteries, Journal of The Electrochemical Society 141 (12), 3296-3299 (1994)

7. C. Navone, R. Baddour-Hadjean, J.P. Pereira-Ramos, and R. Salot, A kinetic study of electrochemical lithium insertion into oriented V_2O_5 thin films prepared by rf sputtering, Electrochimica Acta 53, 3329-3336 (2008)

8. N.J. Dudney and Y.I. Jang, Analysis of thin-film lithium batteries with cathodes of 50 nm to 4 μm thick $LiCoO_2$, Journal of Power Sources 119-121, 300-304 (2003)

9. H.Y. Park, S.C. Nam, Y.C. Lim, et al., $LiCoO_2$ thin film cathode fabrication by rapid thermal annealing for micro power sources, Electrochimica Acta 52, 2062-2067 (2007)

10. F.K. Shokoohi, J.M. Tarascon, B.J. Wilkens, et al., Low temperature $LiMn_2O_4$ spinel films for secondary lithium batteries, Journal of The Electrochemical Society 139 (7), 1845-1849 (1992)

11. H. Otsuji, K. Kawahara, T. Ikegami, and K. Ebihara, $LiMn_2O_4$ thin films prepared by pulsed laser deposition for rechargeable batteries, Thin Solid Films 506-507, 120-122 (2006)

12. M.M. Thackeray, Manganese oxides for lithium batteries, Progress in Solid State Chemistry 25, 1-71 (1997)

CHAPTER VI

CONCLUSIONS AND FUTURE WORK

Multiscale experimental approaches to Li-ion battery research are discussed in this study: in macro scale, a small Li-ion battery in terms of size (~2.5 cm^3) and capacity (~120 mAh) was designed for an implantable medical device; in particle- to micro-scale, baseline cathode materials for Li-ion batteries, including $LiMn_2O_4$, were investigated for their structural and electrochemical characteristics. In the introduction, we discussed the significance of Li-ion battery research to solve the present energy-and-environmental problems, and defined the specific challenges to Li-ion batteries in small-scale (e.g. microchip) and large scale (e.g. EV) applications. High power performance and safety are required for small scale Li-ion batteries in micro-systems and medical devices, while high energy density and long term reliability are key attributes of large format cells for EV/HEV applications to provide a longer driving range per charging. Also, power / energy requirements in small devices are extremely diverse as illustrated by previous MEMS battery studies in the literature, so optimizing the battery design is only feasible by accurately identifying the usage profile. For automotive applications with well-known power / energy requirements and usage profiles, the real challenge is in monitoring and controlling the batteries for a longer period of time based on thorough understanding of the material and the cell behavior. We reviewed the literature of previous experimental

and computational studies on Li-ion battery materials in particle- to micro-scale, and discussed their limitations.

In chapter 2, we demonstrated how a small-scale polymer Li-ion battery was designed (or selected) for an implantable surgical device for distraction osteogenesis. Identifying the power / energy requirements for its clinical protocol was the key step toward an optimized battery design. The design of an optimized battery was done in parallel to the development of a novel distraction device using an electric motor and a control circuit as an actuation mechanism. Based on its power and energy profiles, we ran an algorithm to select a battery with 1) an appropriate electrochemistry, 2) a sufficient capacity, 3) a desirable form factor, and 4) minimal volume. A polymer Li-ion battery was selected due to high power and energy densities as well as its favorable geometry. A bench-top prototype device, integrating an actuator, a control circuit, and a battery, was fabricated to test its functionality and reliability. The selected polymer Li-ion battery showed a good pulsed discharge behavior for a normal distraction process of 15 mm for 15 days. Animal implantation studies of the prototype device, preferably in miniature pigs that are often used for the mandibular distraction studies, should follow the bench-top tests to prove its in-situ operation and safety.

The following three consecutive chapters discuss particle- to micro- scale experimental studies of Li-ion insertion metal oxide cathode materials using simple forms, such as particles and thin films, aiming to understand their structural characteristics and electrochemical properties. We first developed an experimental model using dispersed single $LiMn_2O_4$ particles for generating accurate material properties, including diffusion coefficients and realistic particle geometries, then incorporated them

into battery models. Cyclic voltammetry and potentiostatic intermittent titration technique were used to measure diffusion coefficients, which ranged between 3.22×10^{-12} and 1.22×10^{-11} cm^2/s depending upon the Li-ion concentration. These values are similar to those measured from thin film studies and are 1-2 orders of magnitude lower than those measured in composite electrodes reported in the literature. Simulation of Li-ion intercalation with the implemented experimental measurements showed that a $LiMn_2O_4$ particle could be under higher intercalation-induced stress due to slower diffusion and local stress concentration at the grain boundaries. Future work includes validating the simulation results by measuring Li-ion intercalation-induced mechanical responses, such as strains, within cathode particles using in-situ AFM. Furthermore, different material formats, especially thin films, may provide simpler models.

Microscopic observation from various characterization techniques including SEM, TEM, XRD, and AFM were discussed in chapter 4 for candidate cathode materials of EV applications, such as $LiFePO_4$, $Li[Ni_{1/3}Co_{1/3}Mn_{1/3}]O_2$, and $LiMn_2O_4$. We presented strong evidence of their anisotropic and inhomogeneous nature due to the hierarchic structure consisting of crystal grains and grain boundaries. Atomic or molecular scale analysis of our morphological and structural observation should follow as future work to explain how the non-uniformity within the polycrystalline materials affects their electrochemical and kinetic characteristics.

Lithium manganese oxide thin films, studied in chapter 5, also showed similarly complex microstructures observed in primary particles. We found their micro structural characteristics were highly sensitive to the fabrication conditions, including substrate material and annealing temperature. Comparison between two types of substrate showed

that the types of substrate affect the film's quality as well as its crystalline characteristics. The annealing temperature, however, was found to be the most important factor in determining crystal formation by changing the grain size and its variation. Nano-crystal grains formed when the annealing temperature decreased from 750 to 550°C were less than 1/10 the size of those annealed at 750°C. Both XRD and electrochemical tests suggested the fabricated film materials were either Mn_2O_3 or a mixture of Mn_2O_3 and $LiMn_2O_4$. Unlike other lithium metal oxides, such as $LiCoO_2$, stoichiometry seems to deviate in sputtered lithium manganese oxide films from $LiMn_2O_4$ of target materials. Thus, $LiMn_2O_4$ films should be fabricated either by modifying sputtering conditions, such as atmospheric pressure and target materials, or by using different deposition techniques, including pulsed laser deposition. Then, electrochemical techniques that are described earlier in chapter 3 can be applied to measure the films' diffusion properties to eventually reveal their relationship with their structural characteristics.